Methodology for Probabilistic Tsunami Hazard Analysis: Trial Application for the Diablo Canyon Power Plant Site

Pacific Gas & Electric Company
April 9, 2010

Submitted to the PEER Workshop on Tsunami Hazard Analyses for Engineering Design Parameters, Berkeley CA

Pacific Gas and Electric Company®

10/22/2010

Executive Summary

Executive Summary

Traditionally, tsunami hazard analysis for nuclear power plants has been based on deterministic methods. This approach involved selecting a tsunami wave height, a storm wave height, and a tide level and then adding these three components to estimate a design wave height. Based on a recommendation from PG&E's Advisory Board, we moved away from the deterministic approach and developed a probabilistic method for combining the effects of waves from tsunamis, storms, and tides.

Probabilistic methods have been used for tsunami hazard (e.g. Rikitake and Aida, 1988) but they have not been complete probabilistic treatments. In this report, we develop a probabilistic methodology that incorporates three key modifications to the approach used by Rikitake and Aida (1988). First, we include aleatory variability of the tsunami amplitude for a given source in to the hazard calculation. Second, we include offshore landslide sources in addition to earthquake sources. Third, we include the effects of storms and tides in the probabilistic analysis. Storms and tsunamis are assumed to be independent, but submarine landslides triggered by offshore earthquakes are considered.

A deterministic approach that combines the tsunami generated by a rare local submarine landslide with a large storm wave would lead to an unreasonably rare combination of events. The probabilistic approach developed here allows for the selection of reasonable tsunami waves from distant earthquakes, local earthquakes, or local landslides with an appropriate storm wave.

The issue of proper treatment of aleatory variability in the tsunami wave heights is important. From ground motion studies, it is well known that ignoring the aleatory variability of the ground motion model leads to a significant underestimation of the hazard at low probability levels. The aleatory variability of tsunami wave heights for a given earthquake or landslide scenario will also have a large effect on the hazard at low probability levels.

A trial application of this methodology for PTHA is conducted for the Diablo Canyon Power Plant site. An example of the results is shown in Figure 1 in terms of the wave height above mean sea level at the intake structure. The hazard cure shows that if tsunamis are considered separate from storms and tides, then the hazard for tsunami waves of up to 3m is dominated by distant earthquakes along the circum-Pacific. This is consistent with the historical observations that the majority of historical tsunamis observed in along central Coastal California have been from distant earthquakes around the circum-Pacific.

Figure 1 also shows that for wave heights up to 5 m, the hazard from tsunamis is much smaller than the hazard from storms and tides. For wave heights up to 5 m, the hazard (annual rate) from tsunamis is less than 1% of the hazard from storm waves and tides. The local offshore landslides, while rare, can lead to large tsunami waves that are larger than the storm waves. For wave heights between 7 and 10m, the hazard is dominated by

the submarine landslides with little contribution from storms. At a hazard level of 1E-6, the wave height is 11.5m.

The PTHA shows that the hazard at DCPP can be captured by selecting the appropriate wave heights from storms and tides for hazard levels greater than 1E-5 and from submarine landslides for hazard levels less than 1E-6. A key conclusion is that for this site, adding the wave heights from large storms and large tsunamis, as is typical in developing engineering design tsunami values, corresponds to extremely rare cases that are not justified.

The PTHA results can be used to estimate the probability of exceedance for design values developed using traditional approaches and evaluate the level of conservatism in the current design values. They can also be used to compare with previous estimates of the probabilities of exceeding critical flood levels based on the current practice of adding the storms, tides, and tsunamis in a conservative manner. For DCPP, the probabilities for exceeding two critical flood levels (20 ft above MLLW and 48 ft above MLLW) were estimated as part of the IPEEE conducted in 1994. The IPEEE evaluation did not consider tsunamis from submarine landslides, but it used a conservative approach for combining storms, tides, and tsunami wave heights. The estimated probabilities of exceeding the two critical flood levels from current PTHA are very similar to the probabilities estimated in the IPEEE, indicating that, for the DCPP site, the conservatism in the previous approach accommodated the additional hazard from the submarine landslides.

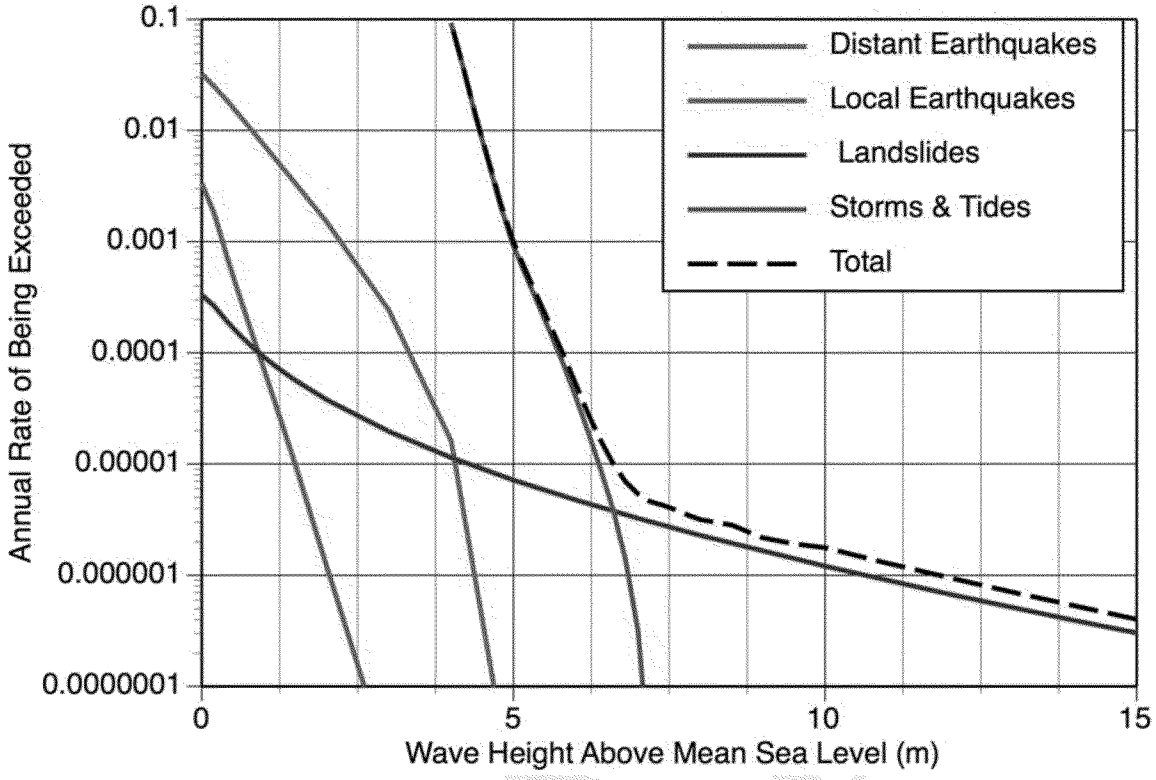

Figure 1. Mean hazard from storms, tides, and tsunamis for the DCPP intake structure.

CONTENTS

SECTION 1
Introduction

1.0 INTRODUCTION

The December 26, 2004 M_W 9.1 Sumatra earthquake and tsunami mobilized efforts to address tsunami safety issues worldwide. The presence of fault zones capable of similar-sized earthquake events offshore northern California, Oregon, and Washington, as well as offshore Alaska and the Aleutian Islands, raised concern about the exposure and safety of critical facilities along the coastline of the western United States (National Science and Technology Policy Council, 2005), including nuclear facilities.

In addition to tsunamis generated by fault displacement, submarine landslides also are recognized as potential sources of damaging tsunamis locally (for example, Plafker and others, 1969; Hampton and others, 1993, 1996; Lee and others, 1993, 2003; Nishenko and others, 2004). In recent years, submarine landslides have been identified as the source of many of the larger "surprise" tsunamis associated with small earthquakes (Ward, 2001).

The method for assessing natural hazards at nuclear facilities has evolved during the past 40 years, shifting from the deterministic identification of probable maximum events to the use of probabilistic seismic hazard analyses (PSHA) for earthquake ground motions. Tsunamis can also be treated in a probabilistic approach, but there is no established methodology for conducting a probabilistic tsunami hazard analysis (PTHA) for nuclear facilities that need to address low probability levels and the combined effects of tsunami, storm waves, and tides

1.1 OBJECTIVES AND SCOPE

This report develops a methodology for conducting a PTHA for nuclear facilities. A trial application of the method to the Diablo Canyon Power Plant (DCPP) site is conducted to demonstrate the proposed approach. Currently, there is no regulatory guidance from the NRC describing the hazard level (annual probability) that should be used for evaluating tsunami hazards at nuclear power plants.

When comparing different natural hazards such as earthquake ground shaking and flooding from tsunamis, they should be evaluated in terms of their contribution to the risk, not simply in terms of their hazard. This requires understanding the risk impacts of the natural hazard. For ground motion, this approach has been applied in Regulatory Guide 1.208 (US NRC, 2007). A similar risk set of risk evaluations should be conducted

for tsunami hazard to provide the technical basis for selecting the appropriate probability level to use.

This report is limited to estimating the tsunami hazard and does not address the selection of the appropriate probability level for use at nuclear power plants. The scope of this study addresses the tsunami hazard at DCPP from all sources using a probabilistic approach. The flooding hazard from tsunamis depends not only on the tsunami wave height, but also on the height of storm waves and tides that occur during the tsunami. Therefore, our probabilistic tsunami hazard analysis (PTHA) includes the combined hazard from tsunamis, storms, and tides.

1.2 PROJECT TEAM

The overall project was conducted under the direction of Lloyd Cluff, Director, Geosciences Department. Dr. Stuart Nishenko, Geosciences Senior Seismologist, served as the project manager. PG&E selected several consultants based on their technological leadership, their experience and expertise, and their familiarity with the DCPP site to perform the work associated with the major technical areas of the project. These consultants formed the Tsunami Hazard Analysis Team.

Kathryn Hanson, Geomatrix Consultants, Inc.; Michael Angell, William Lettis & Associates, Inc.; Dr. Jan Rietman, Fugro West, Inc.; and Dr. Paul Somerville, URS Corporation, compiled and analyzed marine bathymetric, geologic, and geophysical data. These individuals were part of PG&E's Long Term Seismic Program team, which completed extensive onshore and offshore geologic, geophysical, and seismological investigations from 1985 through 1991 to evaluate the seismic design and the seismic margins of the Diablo Canyon Power Plant. Building upon this knowledge and database, they have incorporated recent information and bathymetric data into a comprehensive GIS-based framework to support this analysis of potential local tsunami hazards.

Drs. Hong Kie Thio and Gene Ichinose, URS Corporation, performed the tsunami modeling. These individuals have conducted many analyses of plate boundary earthquakes and tsunamis, including the 1944 Tonankai, Japan; 2002 Arequipa, Peru; 2004 Sumatra-Andaman; and 2005 Nias Island, Indonesia, events, as well as seiche simulations for Lake Tahoe, California; Puget Sound, Washington; and the Dead Sea, Israel.

Dr. Norman Abrahamson, Geosciences Seismologist, and Jennie Watson-Lamprey, consultant, conducted the probabilistic tsunami hazard analysis using the simulated tsunami wave heights, recurrence rates, and storm and tide models.

PG&E's Tsunami Hazards Analysis Technical Advisory Board was a key component in the conduct of this project. The Advisory Board, which consisted of individuals eminently qualified in the subject areas of the project, provided guidance to PG&E and its consultants to ensure the objectives of the project were achieved and that relevant theories, analytical techniques, and other pertinent, newly developed information were considered. The members of the Advisory Board, their affiliations, and their areas of expertise are:

Dr. Clarence R. Allen, California Institute of Technology emeritus (earthquake geology and tectonics, former member of the LTSP Advisory Board; investigations of many earthquakes, including the 1960 Chile and 1964 Alaska tsunamis);

Dr. Gary Greene, Monterey Bay Aquarium Research Institute and Moss Landing Marine Laboratories (California submarine geology);

Dr. Robert P. Kennedy, RPK Structural Mechanics Consulting (civil and structural engineering analysis of nuclear facilities under seismic and other extreme loading conditions);

Dr. George Plafker, US Geological Survey emeritus (geohazards, earthquakes and tsunamis, investigations of the 1946 Aleutian, 1960 Chile, 1964 Alaska, 1992 Flores Island, and 2004 Sumatra tsunamis);

Dr. Robert Wiegel, University of California, Berkeley emeritus (oceanographic and coastal engineering, investigations of the 1960 Chile, 1964 Alaska, and other significant tsunamis).

The Advisory Board met formally on December 20-21, 2005, and August 8-9, 2006 to review the initial study results. Their comments and recommendations were considered in the preparation of this report.

1.3 ACKNOWLEDGMENTS

In addition to the Technical Advisory Board members, we would like to acknowledge and thank Drs. Homa Lee, Eric Geist, and Bill Normark of the US Geological Survey; Lewis Rosenberg, San Luis Obispo County Geologist; Dr. Kurt Schwehr, Center for Coastal and Ocean Mapping Visualization Center at the University of New Hampshire;

Richard Eisner, California Governor's Office of Emergency Services; Dr. Michael Reichle, California Geological Survey; Dr. Vasily Titov and Mick Spillane, NOAA Center for Tsunami Research; and Paula Dunbar, National Geophysical Data Center, for advice and discussion during the project. Marcia McLaren and Dr. William Page, PG&E Geosciences, reviewed and assisted with geologic and seismologic data for the region, and William Horstman, DCPP, served as technical liaison.

SECTION 2

Probabilistic Tsunami Hazard Analysis Methodology

2.0 INTRODUCTION

Probabilistic tsunami hazard analysis (PTHA) is similar to widely used probabilistic seismic hazard analysis for ground motion. The basic approach is to combine the rate at which tsunamis are generated with the distribution of amplitudes that are expected to occur at the site for a given tsunami. The probabilistic tsunami hazard from earthquakes is given by:

$$\nu_{EQK}(W_{tsu} > z) = \sum_{i=1}^{N_{FLT}} N_i(M_{\min}) \int_m \int_{Loc} f_{m_i}(M) f_{Loc_i}(Loc) P(W_{tsu} > z \mid M, Loc)\, dM\, dLoc \qquad (2\text{-}1)$$

where $\nu_{EQK}(W_{tsu} > z)$ is the annual rate of tsunami wave heights exceeding z, N_{FLT} is the number of tsunamigenic fault sources, $N_i(M_{min})$ is the rate of earthquakes with magnitude greater than M_{min} for the i^{th} source, f_m and f_{Loc} are probability density functions for the magnitude and rupture location, and $P(W_{tsu}>z|M,Loc)$ is the conditional probability of the tsunami wave height, W_{tsu}, exceeding the test value z.

Assuming the tsunami wave heights are log-normally distributed, the conditional probability of exceeding wave height z is given by

$$P(W_{tsu} > z \mid M, Loc) = 1 - \Phi\left[\frac{\ln(z) - \ln(\hat{W}_{tsu}(M, Loc))}{\sigma_{EQK}}\right] \qquad (2\text{-}2)$$

where $\hat{W}_{tsu}(m, Loc)$ is the median wave height, σ_{EQK} is the aleatory variability of the tsunami wave height from earthquakes (e.g. standard deviation) in natural log units, and Φ is the cumulative normal distribution.

If only a small number of representative scenarios (magnitude and location) are considered, then the tsunami hazard from earthquakes simplifies to

$$\nu_{EQK}(W_{tsu} > z) = \sum_{i=1}^{N_{FLT}} \sum_{j=1}^{NS_i} rate_{ij}\, P(W_{tsu} > z \mid M_{ij}, loc_{ij}) \qquad (2\text{-}3)$$

where $rate_{ij}$ is the rate of occurrence of the j^{th} scenario from the i^{th} source.

Overall, we propose an approach similar to that of Rikitake and Aida (1988) using synthetic tsunami waveforms from numerical modeling to estimate the median

amplitudes ($\hat{W}_{tsu}(m, Loc)$) and using standard earthquake recurrence models to estimate the rates of occurrence, $rate_{ij}$, for the tsunamigenic earthquakes. An important limitation of the Rikitake and Aida (1988) approach is that they did not include the aleatory variability of the tsunami wave height; they assumed that there was no variability about the wave heights computed from the numerical modeling (e.g. $\sigma_{EQK}=0$). The issue of proper treatment of aleatory variability in the tsunami wave heights is important. From ground motion studies, it is well known that ignoring the aleatory variability of the ground motion model leads to a significant underestimation of the hazard (Bommer and Abrahamson, 2006), particularly at long return periods. The aleatory variability of tsunami wave heights for a given earthquake scenario will also have a large effect on the hazard at long return periods.

We have made three modifications to the approach used by Rikitake and Aida (1988):

(1) Inclusion of the aleatory variability of the tsunami amplitudes

(2) Inclusion of landslide sources

(3) Inclusion of storms and tides

These three modifications are described in the following sections.

2.1 ALEATORY VARIABILITY OF TSUNAMI WAVE HEIGHTS

The tsunami wave heights are computed using numerical simulations. A comprehensive approach for estimation of aleatory variability for numerical simulation based models is given by Abrahamson et al (1990). In this approach, the aleatory variability is subdivided into modeling and parametric components. This division is shown in Table 2-1. This separation is useful for tracking that all of the components of the variability are considered.

Table 2-1. Subdivision of Aleatory and Epistemic Uncertainty into Modeling and Parametric Components.

Modeling Aleatory Unexplained randomness. Estimated from misfit between model and observations	**Modeling Epistemic** Uncertainty that we have the correct model. Captured by logic trees with alternative credible models
Parametric Aleatory Understood randomness Estimated from propagating parameter variability through the ground motion model	**Parametric Epistemic** Uncertainty that we have the correct aleatory distributions for the parameters in the model. Captured by logic trees with alternative parameter pdfs.

Modeling aleatory variability results from the unexplained difference between a model prediction of the tsunami wave height for past tsunamis and the observed data. It represents the limitation of the numerical simulation method and the accuracy of the bathymetric data. It can only be estimated from validation exercises in which the predicted and observed tsunami wave heights are compared.

Parametric aleatory variability is the explained variability that results from using a suite of source parameters, such as slip distribution, dip, and rake for a given earthquake scenario. Any parameter that is optimized for a specific earthquake as part of the validation of the model (in the computation of the modeling aleatory component) must be considered as part of the parametric aleatory variability.

The total aleatory variability is computed from the combined modeling and parametric terms. These two terms are independent so the total aleatory variability is given by

$$\sigma = \sqrt{\sigma_{\text{mod}}^2 + \sigma_{par}^2} \qquad (2\text{-}4)$$

In addition to the aleatory variability, a probabilistic analysis should also address the epistemic uncertainty. The epistemic uncertainty can also be separated into modeling and parametric terms. The modeling epistemic uncertainty arises from a lack of knowledge or data, and it represents the scientific uncertainty that the simulation method is correct.

Parametric epistemic uncertainty is the scientific uncertainty that the correct probability density functions have been used to represent the distribution of source parameters for a given scenario.

2.2 LANDSLIDE SOURCES

The inclusion of landslide sources is straight-forward: the landslides are treated as additional sources with median estimates of the tsunami wave heights computed using numerical simulations and the rates of the landslides estimated from evidence of past landslides in the source region. The rate of the landslides is a total rate that does not distinguish between earthquake triggered landslides and those that occur independent of earthquakes. The annual hazard from landslides is given by

$$\nu_{LS}(W_{tsu} > z) = \sum_{i=1}^{N_{LS}} \sum_{j=1}^{NLoc_i} rate_{ij}\, P(W_{tsu} > z \mid \hat{H}_{ij}, \hat{A}_{ij}, \hat{V}_{ij}, loc_{ij}) \qquad (2\text{-}5)$$

where N_{LS} is the number of landslide source zones, $NLoc_i$ is the number of landslide locations in the i^{th} source zone, and $\hat{H}_{ij}$, $\hat{A}_{ij}$, and $\hat{V}_{ij}$ are the median slide thickness, slide area, and slide velocity, respectively.

Volcanic collapses are treated as a type of landslide. That is, the number of landslide sources should include the relevant volcanic collapses as well as the relevant local landslides.

The combined annual hazard from landslides and earthquakes (without storms and tides) is given by the sum of the two hazards:

$$\nu_{EQK+LS}(W_{tsu} > z) = \nu_{EQK}(W_{tsu} > z) + \nu_{LS}(W_{tsu} > z) \qquad (2\text{-}6)$$

2.3 COMBINED HAZARD FROM TSUNAMIS, STORMS, AND TIDES

The total wave heights depend on the height of the waves caused by the storms and tides as well as from earthquake generated and slide-generated tsunamis. First, we combine the storms and tides by considering all possible combinations of storm waves and tides and summing the rates of the combinations that exceed z. If the storm and tide distributions are discretized, the annual rate at which the combined storm and tide level exceed mean

sea level by z or more during a fixed period of time (here, 3 hours time intervals are used as discussed in Section 7) is given by

$$\nu_{S\&T}(W_{S\&T} > z) = \sum_{j=1}^{N_S} \nu(W_S > x_j) \sum_{i=1}^{N_T} H(W_{Ti} + x_j - z) P(W_{Ti}) \quad (2\text{-}7)$$

where $\nu_{S\&T}(W_{S\&T} > z)$ is the annual rate of storms and tide exceeding z above mean sea level, N_S is the number of discrete storm wave heights above the tide level, x_j are the discrete values for the storm waves, N_T is the number of discrete tide levels above mean sea level, and W_{Ti} are the discrete values for the tide (relative to mean sea level), $P(W_{Ti})$ is the probability of the tide being at W_{Ti}, and H(x) is the Heaviside function which is 1 for x>0 and 0 otherwise. In eq (2-7), the Heaviside function selects the combinations of tides and storms that exceed z.

Similarly, the storms and tides can be combined with the hazard from tsunamis generated from earthquakes and landslides by considering all possible combinations and adding the rates of the combinations that exceed z. The total hazard from storms, tides, earthquake generated tsunamis, and landslide generated tsunamis has two parts: the annual hazard from storms and tides when there is no tsunami and the storms and tides during tsunamis.

$$\begin{aligned} \nu_{Total}(W > z) = &\left(1 - \nu_{EQK+LS}(W > Z_{\min})\right) \nu_{S\&T}(W > x_j) \\ &+ \sum_{j=1}^{N_{S\&T}} P(W_{S\&T} > x_j) \sum_{i=1}^{N_{Tsu}} \nu_{EQK+LS}(W > z - x_j) \end{aligned} \quad (2\text{-}8)$$

Because the annual rate of tsunamis is small, the term $\left(1 - \nu_{EQK+LS}(W > Z_{\min})\right)$ is approximately 1 so the hazard can be approximated by

$$\nu_{Total}(W > z) = \nu_{S\&T}(W > x_j) + \sum_{j=1}^{N_{S\&T}} P(W_{S\&T} > x_j) \sum_{i=1}^{N_{Tsu}} \nu_{EQK+LS}(W > z - x_j) \quad (2\text{-}9)$$

In the following sections, the components of equation (2-9) are computed for the DCPP site as a trial application of the proposed tsunami hazard methodology.

For the application of the PTHA to DCPP, we employed a seven-step process:

1. Construct a digital elevation model for the study region to aid in the identification of local sources and to provide a reference sea-floor surface to be used in

numerical modeling of the tsunami effects at the DCPP site. Appendix A contains background material on the digital elevation model.

2. Identify potential tsunami sources that could impact DCPP. This includes distant earthquakes, local earthquakes, local landslides, and distant volcanic collapses.
3. Develop a small number of representative scenario events and source parameter inputs for each tsunami source.
4. Calculate median tsunami wave height and drawdown and wave flow velocity at the DCPP site using a non-linear tsunami modeling code. Simulations are conducted for each representative scenario event.
5. Estimate the rates of occurrence of each scenario event with significant median tsunami wave heights at DCPP.
6. Develop a probabilistic model of the wave heights at DCPP from storms and tides.
7. Conduct the PTHA for the DCPP site, combining the hazard from tsunamis with the hazard from storms and tides.

The various tsunami sources are then characterized in terms of their rate of occurrence and the median and aleatory variability of the wave height in Sections 4-7. Section 8 characterizes the hazard from storms and tides. Section 9 describes the results of the hazard calculation.

SECTION 3

Historic Tsunamis Along the Central California Coast

3.0 HISTORIC TSUNAMIS ALONG THE CENTRAL CALIFORNIA COAST

The majority of historic tsunamis observed in along central Coastal California have been from distant earthquakes around the circum-Pacific: there have been 16 tsunamis observed from distant earthquakes compared to just 2 observations from locally generated tsunamis. In addition to tsunamis, storms can generate large waves along the coast.

3.1 TIDE GAUGES IN THE CENTRAL CALIFORNIA COASTAL REGION

The principal tide gauges near the DCPP site that would record tsunamis along the central coast of California are at Avila Beach and Port San Luis (Figure 3-1). The Avila Beach tide gauge was established in 1933, ran until 1935, and was reestablished in 1945 (Paula Dunbar, personal comm., 2006). It was located at the Avila Beach recreational pier. In January 1972, the Avila Beach tide gauge was moved to the Port San Luis site on the old fishing pier in the northwest corner of the harbor.

Tide gauges are designed to record diurnal tidal variations and typically dampen shorter period waves, such as tsunamis. This damping creates a discrepancy between the real and recorded amplitudes. As a result, recorded maximum amplitudes may be less than the actual maximum wave heights (see Appendix 2, Section A2.6).

A review of historical tsunami records and studies of the underwater topography by Marine Advisors (1966) determined that the wave heights recorded at Avila Beach are the result of local conditions that produce abnormally high response. Avila Beach has recorded extreme high and low water levels, as much as twice the tidal range and commonly two or three times as great as the rest of coastal California. A comparison of water wave spectra at the DCPP site and Avila Beach by Marine Advisors (1966) indicated the two areas do not resemble one another in spectral response (Figure 3-2) and would behave differently during a tsunami. Avila Beach is influenced by the natural periods of the bay itself, whereas the DCPP site is not. Although these two sites are different, the data from Avila Beach are an important benchmark for comparison with data from the DCPP site and elsewhere along the California coast.

3.2 DISTANT TSUNAMIS

Table 3-1 lists the recorded maximum wave heights at Port San Luis and Avila Beach from 1946 to 2004 for tsunamis generated by plate-boundary earthquakes and volcanic events around the circum-Pacific. Observations at San Luis Obispo and Morro Bay for the 1946 Aleutian tsunami and at Pismo Beach for the 1960 Chile event also are listed. Figure 3-3 shows the locations of the events with respect to the DCPP site.

The largest observed tsunamis are from the 1964 Alaska earthquake (1.6 m), 1952 Kamchatka earthquake (1.4m), and the 1946 Aleutians earthquake (1.3m). The other 13 distant tsunamis had amplitudes less than 1 m at Avila Beach or Port San Luis.

3.3 LOCAL TSUNAMIS

Local tsunamis are defined as those generated by nearby sources, generally less than 200 kilometers from the Diablo Canyon Power Plant (DCPP) site. Table 3-2 lists the wave heights recorded from local tsunami. Local tsunamis that were generated in and affected the study region occurred on November 22, 1878 near San Luis Obispo and on November 4, 1927 near Lompoc, California. The 1927 Lompoc tsunami is consistent with a tectonic or fault-rupture origin, whereas the 1878 San Luis Obispo tsunami is considered to have been caused by a submarine landslide that was neither earthquake- nor storm-triggered.

3.3.1 November 22, 1878 San Luis Obispo Tsunami

The November 22, 1878 San Luis Obispo tsunami (listed as November 2, 1878 in Marine Advisors (1966) or May 10, 1877 or August 13, 1868 in Joy (1968)) caused one fatality, destroyed wharfs at Cayucos, Avila, and Point Sal, and was observed at Surf and Port Harford (Figure 2-1). No earthquake or wind was reported. An article in the *San Luis Obispo Tribune* (Saturday, November 23, 1878) contains eyewitness accounts of the damage near San Luis Obispo:

> "Marine Phenomena. On Friday last (November 22nd) a tidal wave swept along this coast doing considerable damage to many of the landings. The full extent of the wave and the exact amount of injury inflicted is not known at this time. It was observed as far south as Wilmington where the water fell three feet below the breakwater and in half an hour rose as many feet above it. As near as we can ascertain the culmination of the wave was within a few miles of San Luis Obispo Harbor. The principal damage was done at Point Sal. About half the wharf at this point is reported to have been carried away, involving the loss of several hundred sacks of grain and

the drowning of one man. The Point Sal wharf was a strong structure and in thorough repair. Captain Hanna of the Gypsy was at Point Sal taking on grain when the disturbance commenced and was obligated to put over to Port Harford, near Avila. The captain states that he has not seen such heavy seas for years. The greater part of the old Peoples Wharf at Avila was carried away. This was not a very substantial affair, having been badly damaged last winter, since which time it has not been used and but partially repaired. Superintendent Haskins states that the reef that protects Port Harford presented a grand appearance during the raging of the waters. The wave would break against the rocks throwing the spray in clouds many feet above the highest rock. Port Harford was not affected. A gentleman who was driving along the beach in the vicinity of Price's Surf Landing (Pismo) reports an unusual commotion in the ocean early in the day. It was low tide at the time and the water would recede and then rush in with great force to above the high water mark. At Morro the sea ran so high as to break over the sand ridge which divides the bay from the ocean. The Cayucos Wharf was slightly damaged, losing about 30 piles. The new wharf at San Simeon was uninjured. The most remarkable thing was the absence of wind. The disturbance was doubtless occasioned by a submarine earthquake."

The *Los Angeles Express* (November 22, 1878, p. 3) mentions a dispatch from San Luis Obispo reporting damage to the wharves at Point Sal, the Peoples Wharf at San Luis Landing, and the Cayucos Wharf. The *Express* further reports, "While this destruction was going on it is a fact worthy of notice that there was no injury done to the wharf here in Santa Monica." Lander and others (1993) state this event was probably a local submarine landslide near Surf and compares the effects to those of the November 4, 1927 Lompoc event.

3.3.2 November 4, 1927 Lompoc Earthquake Tsunami

The tsunami generated by the 1927 Lompoc earthquake is one of the few California tsunamis that had a tectonic rather than a landslide origin (McCulloch, 1985; Lander and others, 1993). In contrast to the 1878 San Luis Obispo tsunami, this event was associated with a M_W 7.0 earthquake, approximately 25 miles southwest of Point Arguello, and was observed at tide gauge stations at Fort Point (San Francisco) and Hilo, Hawaii. In addition to tide gauge observations, Byerly (1930) reported waves as high as 4 feet (1.2 m) at Port San Luis, south of the Diablo Canyon, and 6-foot (1.8-m) waves were observed at Surf. At Pismo, the first wave was reported as positive (there was no initial recession of the water). At Surf, the run up destroyed the Southern Pacific Railroad tracks for many yards and inundated the railroad station (Lander and others, 1993). Satake and Somerville (1992) show that a reverse fault having 2.5 meters of displacement

is sufficient to model the tsunami arrivals at Fort Point and Hilo. The 1927 Lompoc event is discussed further in Section 5.

Table 3-1 Tsunamis from Distant Earthquakes Recorded at Central California Tide Gauges

Earthquake-generated Tsunami			Wave Height (m)					
Date	Location	Magnitude		Port San Luis	Avila Beach	Morro Bay	San Luis Obispo	Pismo Beach
4/1/1946	Aleutians	8.1			1.3	1.5	1.3	
12/20/1946	Japan	8.1			0.1			
11/4/1952	Kamchatka	9.0			1.4			
3/30/1956	Kamchatka	†			0.1			
3/9/1957	Aleutians	8.6			0.5			
11/6/1958	Kuriles	8.3			0.1			
5/22/1960	S. Chile	9.5			0.9			1.4
10/13/1963	Kuriles	8.5			0.3			
3/28/1964	Alaska	9.2			1.6			
10/17/1966	Peru	8.1			0.1			
5/16/1968	Japan	8.2			0.1			
11/29/1975	Hawaii	7.2		0.4				
6/22/1977	Tonga	7.2		0.1				
12/3/1995	Kuriles	7.9		0.1				
6/23/2001	Peru	8.4		0.27				
12/26/2004	Sumatra	9.1		0.23				

† Explosion of Bezymianny volcano, Kamchatka

Sources: htpp://earthquake.usgs.gov/; htpp://www.noaa.gov/; Lander and others, 1993.

Table 3-2 Tsunamis from Local Earthquakes Recorded at Central California Tide Gauges

Earthquake-generated Tsunami			Wave Height (m)					
Date	Location	Magnitude		Port San Luis	Avila Beach	Morro Bay	San Luis Obispo	Pismo Beach
11/22/1878	San Luis Obispo	‡						
11/4/1927	Lompoc	7.0		1.2*				

‡ Landslide
* Reported (Byerly, 1930); tide gauge not installed until 1972

Sources: PG&E (1988) LTSP Final report; Lander and others, 1993

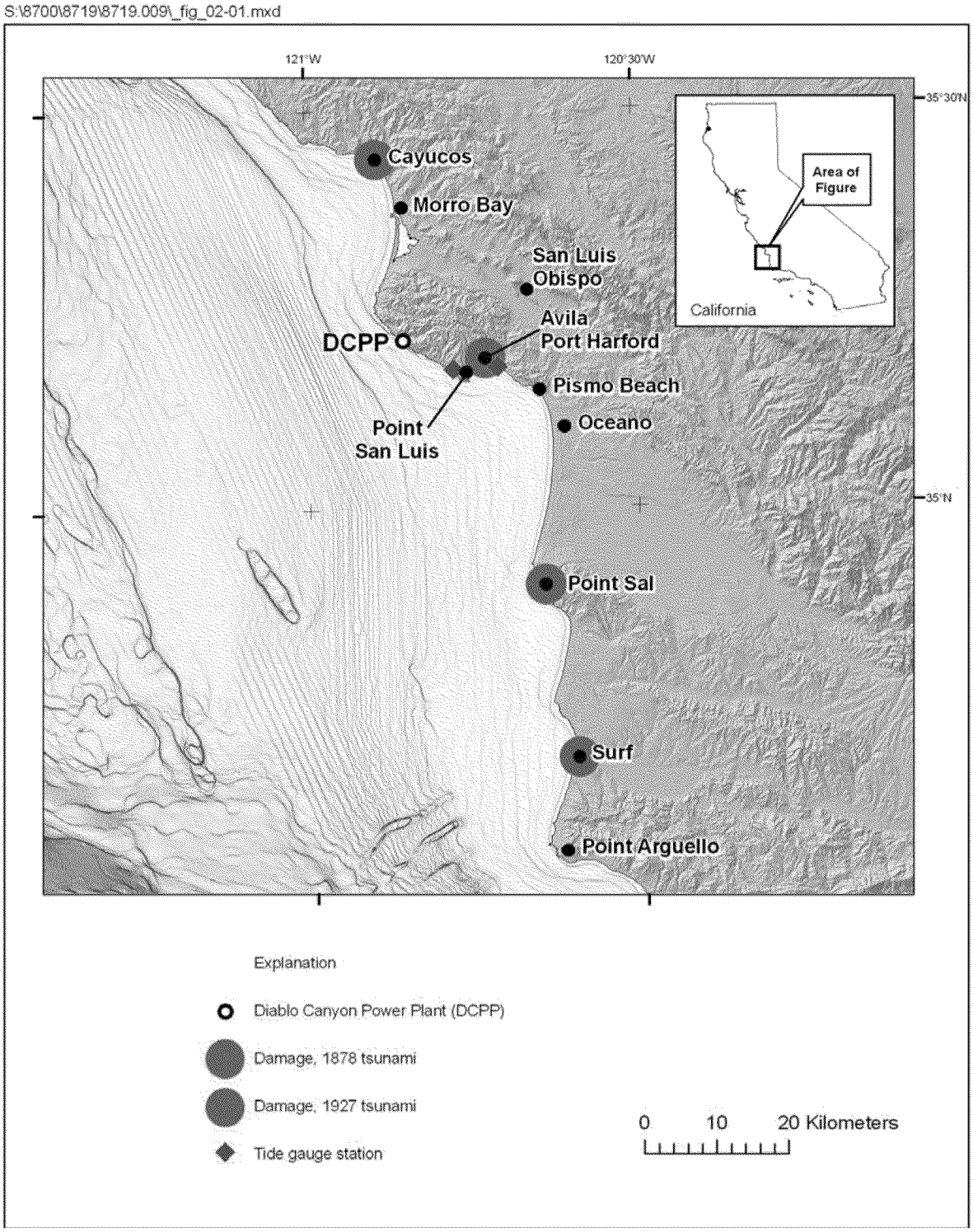

Figure 3-1 **Map showing the locations of damage due to the 1878 and 1927 tsunamis, and the Avila Beach and Port San Luis tide gauge stations.**

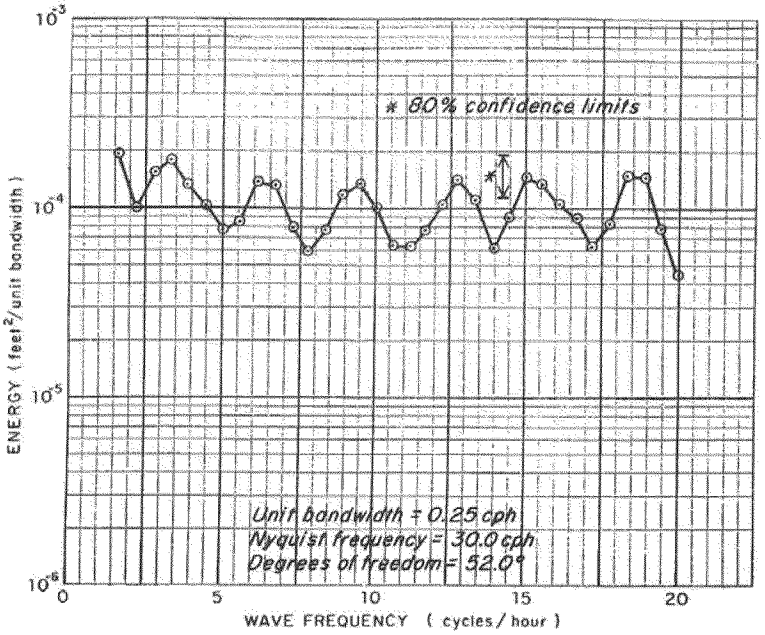

Long-wave energy spectrum at Diablo Canyon.
November 1966

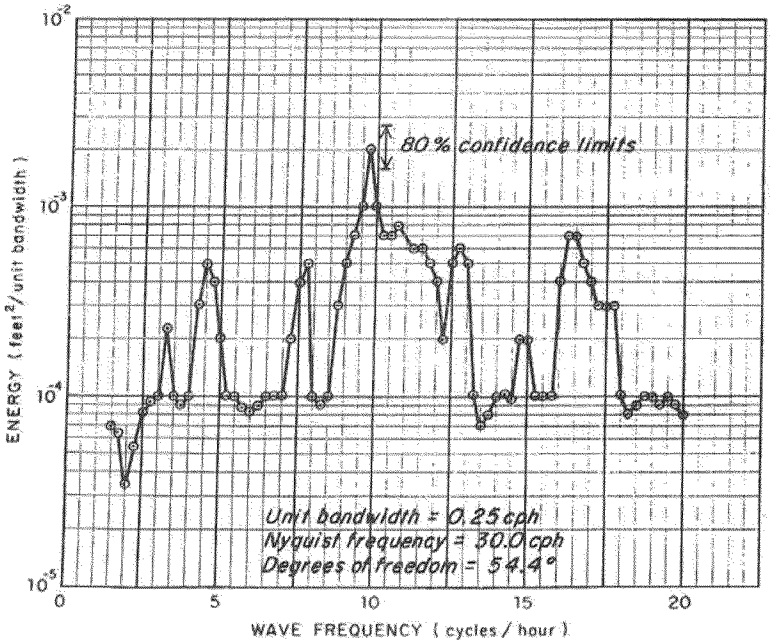

Long-wave energy spectrum at Avila.
November 1966

Figure 3-2 **Comparison of DCPP site and Avila Bay water wave spectra (from Marine Advisors, 1966).**

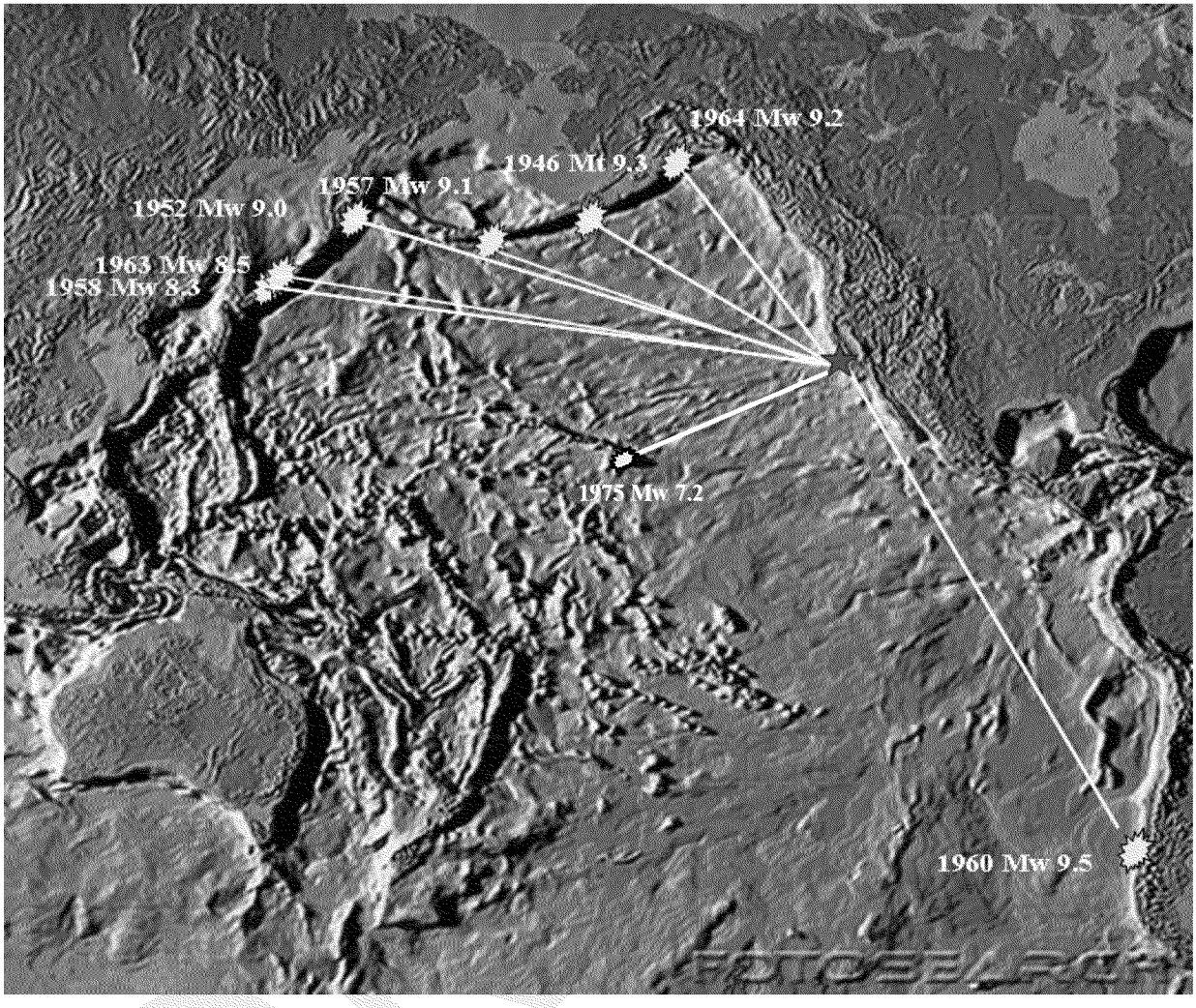

Figure 3-3 **Locations of earthquakes listed in Table 3-1 with respect to the DCPP site. Note: The M_t 9.3 magnitude for the 1946 event has been computed from tsunami amplitude; the earthquake was M_W 8.1.**

SECTION 4

Distant Tsunamis

4.0 CIRCUM PACIFIC EARTHQUAKE SOURCE CHARACTERIZATION

Distant tsunamis that may impact DCPP are from large subduction zone earthquakes in the circum Pacific. Earthquakes in four subduction zones were considered: Aleutians, Kamchatka, South America, and Cascadia. To keep the volume of numerical simulations manageable in the tsunami modeling, the tsunamigenic earthquakes in these zones were simplified to a small number of representative scenario events. The scenario event rupture parameters are summarized in Table 4-1.

4.1 LARGE SUBDUCTION ZONE EARTHQUAKES IN THE CIRCUM PACIFIC

4.1.1 ALASKA-ALEUTIAN SUBDUCTION ZONE

The Queen Charlotte/Alaska/Aleutian seismic zone marks the boundary between the Pacific and North American plates and comprises five distinct tectonic regimes along its 5,000-kilometer length. These include predominately strike-slip faulting along the Queen Charlotte/Fairweather fault system, a zone of transition between strike-slip and underthrust motion in southeastern Alaska, a continental-type subduction regime in southern Alaska, which grades into dip-slip to oblique-slip island-arc-type subduction in the Aleutian Islands, and a regime of dominantly left-slip oblique subduction/transform motion in the Kommandorski Islands.

Subduction along the Aleutian island arc has produced great earthquakes having significant tsunami wave heights along the western United States, including the 1946 Unimak Island (M_W 8.1, M_t 9.3), 1938 Alaska Peninsula (M_W 8.2), 1957 Central Aleutians (M_W 8.6), and the great 1964 Alaska (M_W 9.2) events. The 1964 Alaska earthquake is the third largest earthquake in recorded history. It produced large local tsunamis (Plafker and others, 1969; Lee and others, 2003), in addition to the tsunami that reached the coasts of California, Oregon, and Washington (Plafker, 1969), causing significant loss of life and property. In California, the highest amplitudes were measured at Crescent City—the fourth wave reached a height of 6.33 meters above mean lower low water (Lander and others, 1993).

Two representative scenario earthquakes are selected, both located along the Eastern Aleutian subduction zone: M9.2 and M8.75. The larger magnitude, M9.2, represents earthquakes with M>9. The recurrence interval for earthquakes in the Eastern Aleutian, including Prince William Sound and Kodiak source zones, of a 1964 size (M>9) earthquake is 650 years (Wesson et al., 2007). For the Western Aleutians, the recurrence

interval for M>9 earthquakes is 600 years (Wesson et al, 2007). The M9.2 scenario is intended to represent earthquakes in both the eastern and western Aleutians. Therefore, the recurrence interval is computed from the combined rates of these two sources. The recurrence interval for M>9 earthquakes in either zone is estimated to be 310 years. The smaller magnitude scenario, M8.75, represents earthquakes in the magnitude range M8.5-M9.0. The large magnitude scenario is considered to be the characteristic earthquake for this zone, but the smaller magnitude scenario could also occur. Based on the Youngs and Coppersmith (1985) characteristic earthquake model, the rate of earthquakes 0.5 magnitude units below the characteristic part is about 1/4 of the rate of the characteristic part. Alternatively, the characteristic part of the model could be broader than the 0.5 magnitude width assumed in the Youngs and Coppersmith model. Therefore, we have assumed that the rate for M8.5-M9.0 is the same as the rate for M>9 (e.g. 310 years).

4.1.2 KAMCHATKA SUBDUCTION ZONE

The Kamchatka seismic zone is one of the most active in the circum-Pacific region, producing numerous large and great earthquakes. The earthquake history for Kamchatka records several earthquakes that produced significant tsunamis during the past 250+ years. The 1952 (M_W 9.0) rupture produced wave heights of 1 to 1.4 meters at Crescent City and Avila Beach. Prior events occurred in 1737 (M 9?), 1792 (M 8.4), 1841 (M_W 9.0), and 1923 (M_W 8.5). Wave heights in Hilo, Hawaii, for the 1841 and 1952 events were 4.6 meters and 3.7 meters, respectively (Abe, 1979). Although the 1841 event was not recorded along the central California coast, the ratio of wave heights at Hilo (4.6/3.7, or 1.24), suggests wave heights of approximately 1.8 meters at Avila Beach. Johnson and Satake (1999) indicate the 1737 event, in addition to being a M_W 9 earthquake, also may have ruptured the same segment of the arc.

Two representative scenario earthquakes are selected along the Kamchatka subduction zone: M9.0 and M8.5. The larger magnitude scenario represents earthquakes of magnitude 8.75 and larger. Based on the observation of three earthquakes with M>8.75 in the last 272 years, we assign an average recurrence interval of 90 years for this scenario. The smaller magnitude scenario represents earthquakes in the magnitude range of M8.25 - M8.75. Based on two earthquakes in the magnitude range in the last 218 years, we use a recurrence interval of 200 years for this scenario.

4.1.3 SOUTH AMERICAN SUBDUCTION ZONE

Large and great earthquakes occurring on the subduction plate boundary between the Nazca and South American plates have produced significant damaging tsunamis throughout the circum-Pacific region during the past 450 years. Approximately ten earthquakes having magnitudes greater than 8 have occurred along the coasts of Chile and Peru since 1562, including the largest recorded earthquake in history, the M_W 9.5 1960 Chile earthquake. The north/south orientation of the coastline of Chile, coupled with the direction of the tsunami wave propagation, focuses most of the energy toward the western Pacific, resulting in significantly smaller wave heights along the western United States. Along the California coast, wave heights for the 1960 tsunami were less than 2 meters, with the highest observed at Crescent City (1.7 m). Wave heights at Avila Beach reached 0.9 meters. Written accounts of earlier great South American earthquakes before the installation of the tide gauge at Avila Beach indicate similar wave heights along the California coast (Lander and others, 1993). Hawaii and Japan, which were in the direction of maximum amplitude or directivity, experienced considerable destruction by waves that reached 6 meters in height.

Based on historical and geologic records, 4 earthquakes with magnitudes greater than 9 have occurred between 1575 and 1960, this gives a recurrence interval of 128 years (Nishenko, 1985). Larger earthquakes, on the order of magnitude 9.5, occurred in 1575 and 1960, resulting in a recurrence interval for magnitude 9.5 and greater earthquakes of 385 years (Cisternas and others, 2005).

One earthquake with a magnitude of 9.5 located along the coast of Chile is selected as a representative scenario. A magnitude range of M>9 is assigned to this scenario. Based on the observed rate of M>9 earthquakes, a recurrence interval of 130 years is used for this scenario.

4.1.4 CASCADIA SUBDUCTION ZONE

The Cascadia subduction zone represents the boundary between the Juan de Fuca, Gorda, and North American plates, extending from Cape Mendocino in northern California along the Oregon, Washington, and British Columbia coast to Vancouver Island—a length of 1,000 kilometers. An earthquake that would rupture the entire length of the Cascadia megathrust would be comparable in size to the 2004 M_W 9.1 Sumatra-Andaman earthquake.

One earthquake with a magnitude of 9.0 rupturing the full Cascadia subduction zone is selected as a representative scenario. The recurrence interval for an earthquake rupturing the entire Cascadia is about 500 years (Petersen and others, 2008). This scenario earthquake represents earthquakes in the magnitude range of M>8.75.

4.2 TSUNAMI MODELING

Tsunami waveforms at DCPP were modeled using a fully non-linear nested-grid approach with a base resolution of 3 arc min (5.5 km) for the Pacific Ocean propagation that is subsequently refined in stages to a final resolution of 2.4 arc sec (75 m) around the DCPP site (see Appendix 2). The wave heights were computed at the DCPP intake and discharge for each of the selected scenario events and are listed in Table 4-1. These are considered to be the median values of the wave heights. In addition to the median values, the aleatory variability is also needed. The evaluation of the aleatory variability for the simulation procedure is described below.

4.2.1 TSUNAMI WAVE HEIGHT ALEATORY VARIABILITY AND BIAS

As described in Section 2, the aleatory variability is separated into modeling variability and parametric variability. There are two factors that contribute to the aleatory parametric variability: variability in the earthquake source properties (magnitude, slip distribution, dip), and variability in the earthquake location within the source zone.

URS (2010) estimated the modeling variability of the maximum wave height for high resolution (5 to 10 m grid size) bathymetry. Based on the comparison of recordings from three earthquakes (1952 Kamchatka, 1960 Chile, and 1964 Alaska), the mean bias is -0.15 natural log units and the standard deviation is 0.15.

The parametric variability due to the dip variability is 0.29 natural log units and the parametric variability due to the slip variability is 0.26 natural log units (Thio, personal communication, 2010). The parametric variability due to location within a region is 0.40-0.45 natural log units for the Alaska and Kamchatka source regions (Thio, personal communication, 2010). For a scenario with location variability, the total aleatory standard deviation is about 0.60. For scenarios for full rupture of a zone, there is no location uncertainty and the total aleatory standard deviation of 0.42.

Given the small number of samples on which the modeling variability is estimated, the epistemic uncertainty in the total aleatory variability is assumed to be 0.1 natural log

units. For scenarios with location variability, the following values of the aleatory variability with their weights in parentheses are used: 0.5 (0.2), 0.6 (0.6), and 0.7 (0.2). For scenarios without location variability (M9.5 South America and M9 Kamchatka), the following values of the aleatory variability and weights are used: 0.35 (0.2), 0.42 (0.6), and 0.50 (0.2).

The mean bias is -0.15 natural log units. Based on the small number of observations, the standard error of the mean bias is 0.1. Three values of the bias, centered on the mean value, are assumed: 0.0 (0.2), -0.15 (0.6), and -0.30 (0.2). Again, the numbers in parentheses are the weights assigned to each alternative value. These three bias values correspond to scale factors of 1.0, 0.86, and 0.74. This implies that the modeling method tends to over predict the tsunami wave heights by 14% on average. The upper tail of the tsunami wave height distribution is not well constrained. Therefore, the lognormal distribution is truncated at 2 standard deviations.

An evaluation of the aleatory variability for drawdown was not addressed in the URS (2010) study. The aleatory variability for the drawdown may be smaller than for the maximum wave height but without estimates, we use two values to bound the range as part of a sensitivity study: for the first case, the aleatory variability for the drawdown is assumed to be the same as the aleatory variability for the maximum wave height; for the second case, the aleatory variability is assumed to be zero. The zero variability case is intended to show the lower bound for the drawdown hazard and does not represent a best estimate.

4.2.2 TSUNAMI WAVE HEIGHTS AT DCPP

The source models and tsunami wave height results for the four distant subduction zones are described below. The resulting tsunami wave heights, drawdown, and peak velocities are summarized in Table 4-2.

4.2.2.1 Aleutian subduction zone

For the larger magnitude Aleutian subduction zone scenario, the source model is based on the 1964 earthquake. Slip models with and without slip on the Patton Bay fault were considered, but there was not a significant difference in the wave heights at DCPP for

these two source models. Therefore, the case without the Patton Bay fault was selected. The source model without the slip on the Patton Bay faults is shown in Figure 4-2. The computed tsunami wave height is 1.17m at both the DCPP intake and discharge sites. For the smaller magnitude scenario, the computed wave heights are 0.34 m at both the DCPP intake and discharge sites.

4.2.2.2 Kamchatka subduction zone

For the Kamchatka large magnitude scenario, the source model is based on uniform slip. The computed tsunami wave heights at the DCPP intake and discharge sites are 1.13 m and 0.87 m, respectively. For the smaller magnitude scenario, the computed tsunami wave heights are 0.08 m and 0.09 m at the DCPP intake and discharge sites, respectively.

4.2.2.3 South American subduction zone

For the South American subduction zone, two different slip models based on the 1960 Chile earthquake were considered: a uniform slip model (Plafker, 1972) and a variable slip model estimated from the inversion of coastal geodetic deformation measurements (Barrientos and Ward, 1990), both shown in Figure 4-3. The uniform slip model has a displacement of 20 m everywhere on the fault plane, whereas the variable slip model has a spatially varying displacement on the fault plane and a peak displacement of 40 m. In the latter model, the maximum slip occurs at depth, with the shallow slip tapering off to only a few meters at most. Since the Barrientos and Ward (1990) model is based on geodetic observations, the resolution of offshore slip is presumably poor. The uniform slip model produces results that are more consistent with observed tsunami wave heights. Therefore, the uniform slip model was selected.

For the M9.5 scenario, modeled tsunami wave heights at the DCPP intake and discharge sites are 0.47m and 0.44 m, respectively.

4.2.2.4 Cascadia

The fault slip model named the "Cascadia 1700 Long Wide" model was developed by Satake and others (2003) based on historical wave height values in Japan from a Mw ~9 earthquake along the Cascadia subduction zone that occurred on January 28, 1700. This model adjusts for the slip profile along the trench in order to fit the wave height and inundation at several sites in Japan.

The tsunami wave heights at DCPP are small for this scenario ranging from 0.3 to 0.5 m.

Table 4-1. Source Parameters for the Distant Earthquake Scenarios

Subduction Zone	Mag. Range	Scenario Mag.	Recurrence Interval (years)	Source Geometry		
				Length (km)	Width (km)	Slip (m)
Alaska /Aleutian	M>9	9.2	310	800	150-250	Variable
Alaska /Aleutian	M8.5-M9.0	8.75	310	400	150	10
Kamchatka	M>8.75	9	90	700	100	15
Kamchatka	M8.25-M8.75	8.5	200	150	200	8
South America	M>9	9.5	130	950	200	20
Cascadia	M>8.75	9	500	1400	200	Variable

Table 4-2. Tsunami Modeling Results for Distant Earthquakes.

		Maximum Amplitude (m)		Minimum Amplitude (m)		Peak Velocity (m/s)		Peak Velocity at Maximum Amplitude (M/s)	
Source	Mag	Intake	Discharge	Intake	Discharge	Intake	Discharge	Intake	Discharge
Alaska /Aleutian	9.2	1.17	1.17	-1.35	-1.33	1.13	1.00	0.67	0.66
Alaska /Aleutian	8.75	0.34	0.34	-0.32	-0.32	0.38	0.39	0.24	0.21
Kamchatka	9	0.87	1.13	-0.99	-0.78	0.75	0.69	0.35	0.32
Kamchatka	8.5	0.09	0.08	-0.03	-0.02	0.10	0.10	0.02	0.02
South America	9.5	0.44	0.47	-0.63	-0.60	0.73	067	0.23	0.14
Cascadia	9	0.33	0.50	-0.46	-0.51	0.91	1.19	0.13	0.06

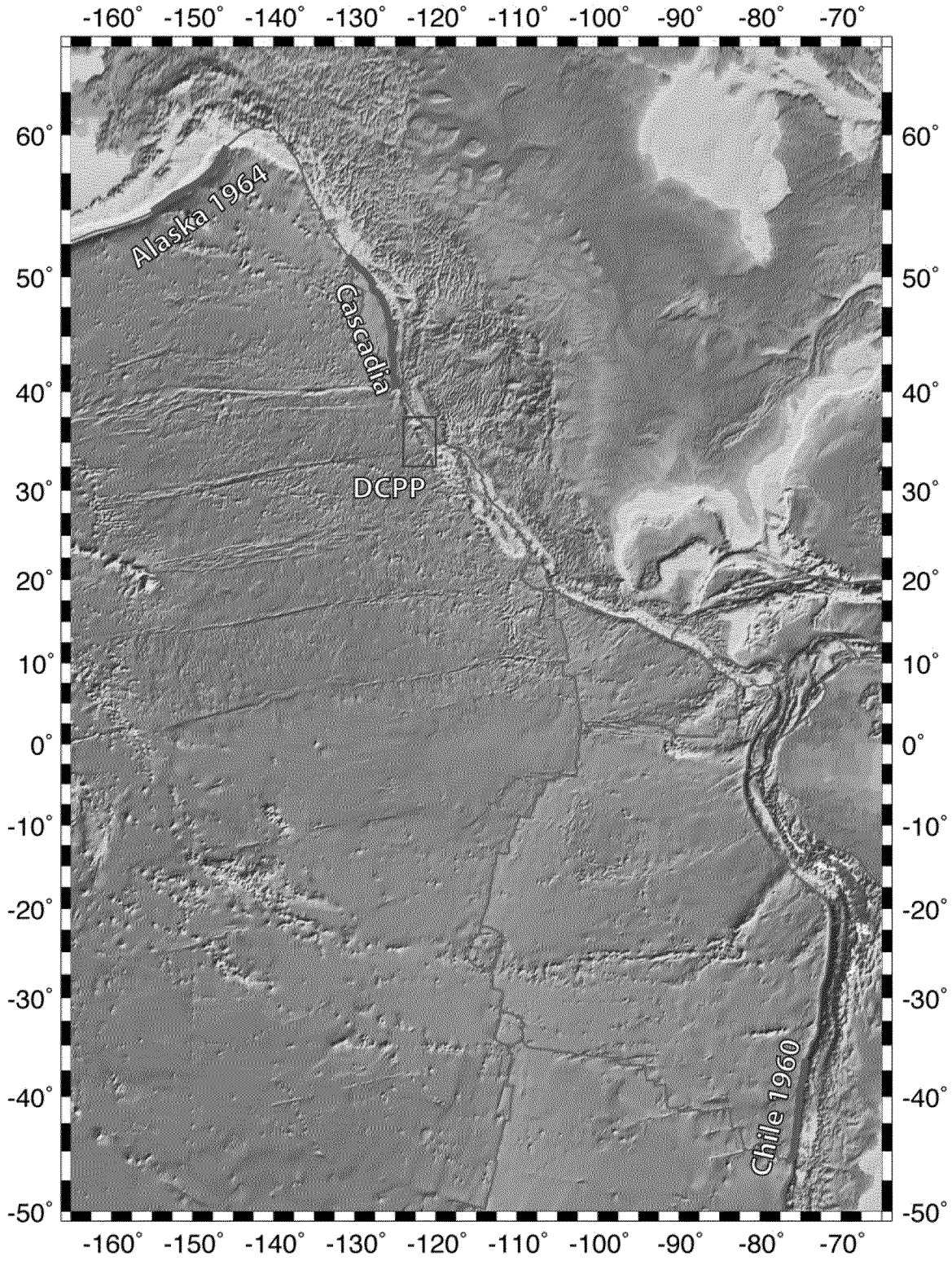

Figure 4-1 Map of the Pacific Ocean showing the teleseismic sources considered in this study.

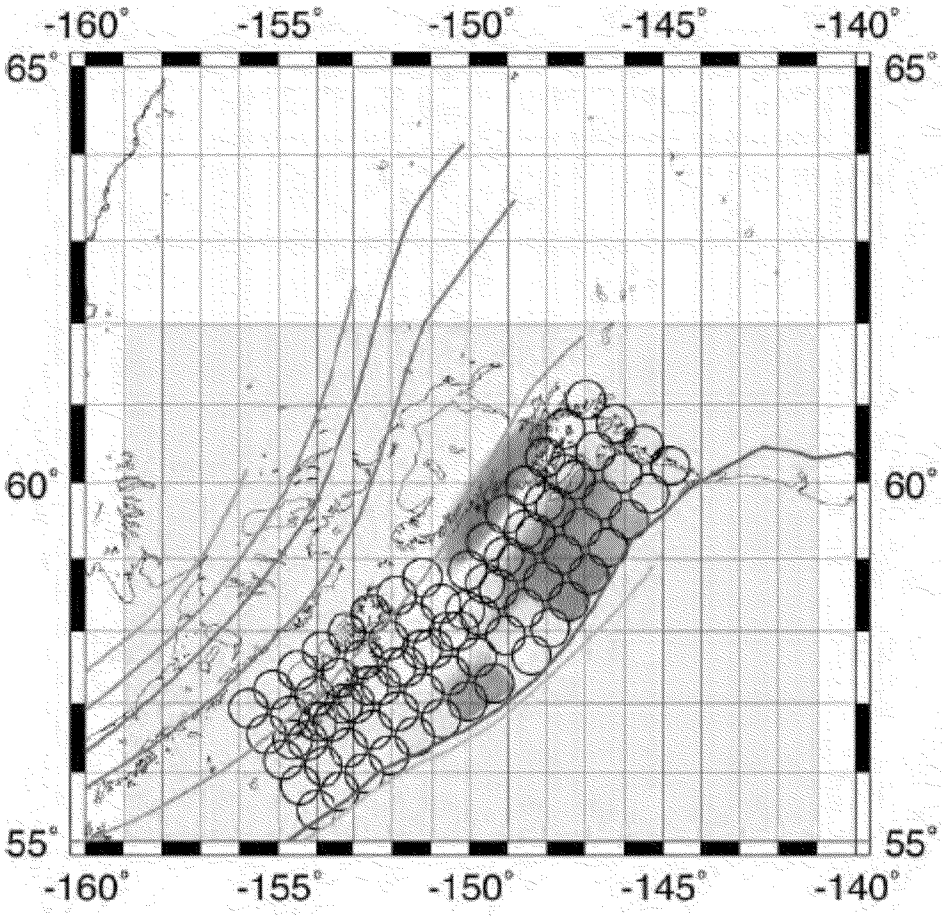

Figure 4-2 1964 Alaska earthquake model. Source model and vertical deformation for the 1964 Alaska earthquake scenario, based on the source model of Johnson and others (1996).

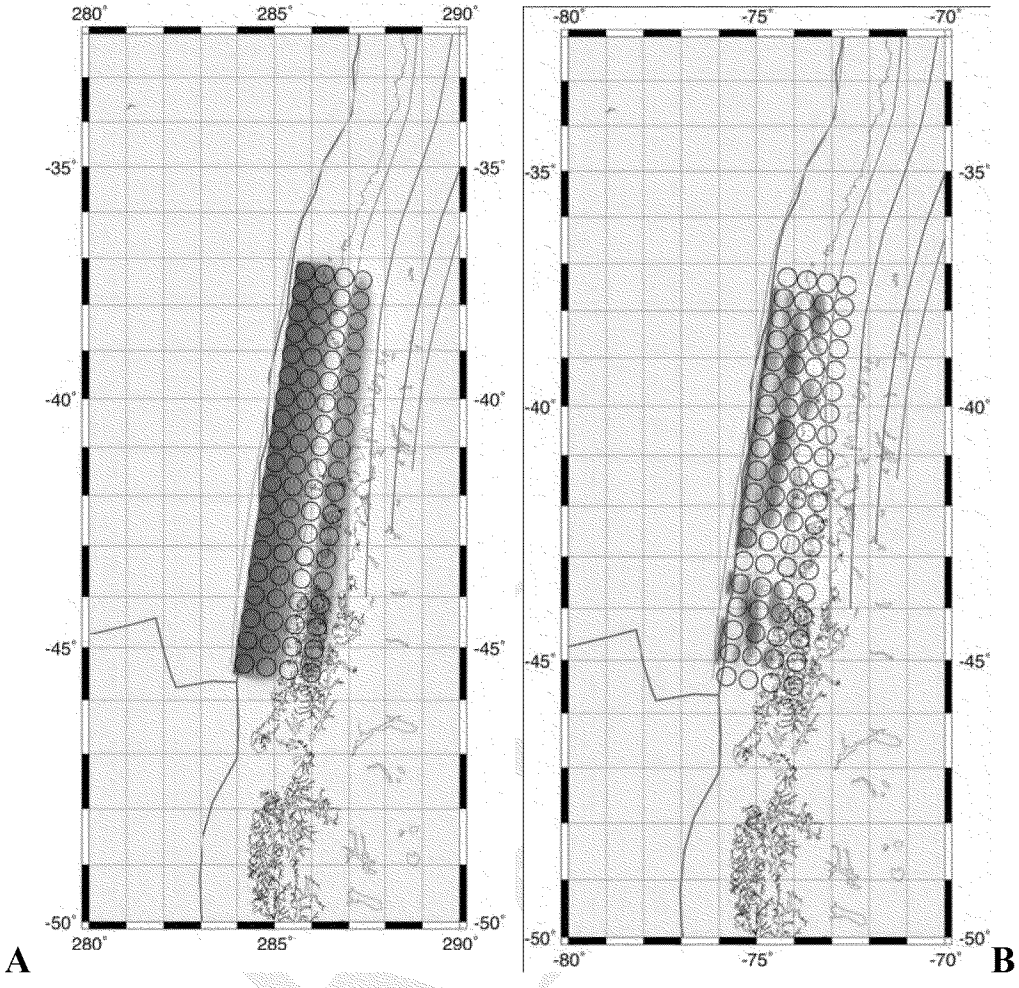

Figure 4-3 1960 Chile earthquake models. a) Vertical deformation for the uniform slip model of the 1960 Chile earthquake (after Plafker, 1972). b) Static deformation for the variable slip model of Barrientos and Ward (1990).

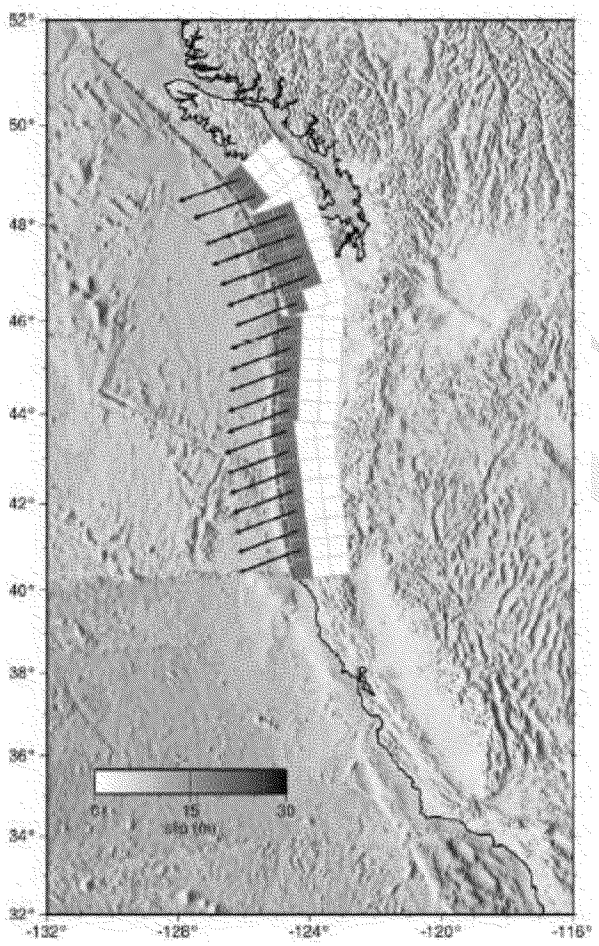

Figure 4-4 Cascadia slip model modified from Satake and others (2003) for the 1700 Cascadia earthquake and tsunami. The fault rake (shown by arrows) is fixed in the direction of relative plate motion.

SECTION 5

Local Tsunamis - Faulting

5.0 FAULT SOURCE CHARACTERIZATIONS

For the local fault source characterization six fault zones were considered. Recurrence rates for the scenario earthquakes were calculated based on the LTSP (PG&E 1988) and the source characterization from the 2008 National Seismic Hazard Maps (NSHM) (Petersen and others, 2008). Scenario earthquakes ruptures were developed for the Hosgri and Casmalia fault zones, the northern Santa Lucia Bank fault zone, and the Purisima and Queenie structures, as well as a repeat of the Lompoc 1927 event. Scenario rupture parameters are summarized in Table 5-1. The rupture zones used for tsunami simulations are mapped on Figure 5-1.

5.1 Scenario Earthquake Ruptures

5.1.1 Hosgri Fault Zone

The Hosgri fault zone is the southernmost component of a complex system of right-slip faults subparallel to the central California coast that includes, from north to south, the San Gregorio, Sur, and San Simeon fault zones. PG&E (1988) and Hanson and others (2005) characterized the contemporary style of faulting along the Hosgri fault zone based on an integrated analysis of a broad spectrum of data. The analysis included shallow high-resolution and deep penetration seismic reflection data, geologic and geomorphic data along the Hosgri and San Simeon fault zones and the intervening San Simeon/Hosgri pull-apart basin, the distribution and nature of near-coast seismicity, regional tectonic kinematics, and comparison of the Hosgri fault zone with strike-slip, oblique-slip, and reverse-slip fault zones worldwide. These data show that the modern Hosgri fault zone is a convergent right-slip (transpressional) fault having a late Quaternary slip rate of 1 to 3 mm/yr. Evidence supporting predominantly strike-slip deformation includes a long, narrow, linear zone of faulting and associated deformation; the presence of asymmetric flower structures; kinematically consistent localized extensional and compressional deformation at releasing and restraining bends or steps, respectively, in the fault zone; changes in the sense and magnitude of vertical separation both along trend of the fault zone and vertically within the fault zone; strike-slip focal mechanisms along the fault trace; a distribution of seismicity that delineates a high-angle fault extending through the seismogenic crust; high ratios of lateral to vertical slip along the fault zone; and the separation by the fault of two tectonic domains (offshore Santa Maria basin, onshore Los Osos domain) that are undergoing contrasting styles of deformation and orientations of crustal shortening. The convergent component of slip is evidenced by the deformation of the early late Pliocene unconformity. In characterizing the style of faulting along the

Hosgri fault zone, alternative tectonic models were assessed by evaluating the cumulative effects of multiple deformational episodes, which can produce complex, difficult-to-interpret fault geometries, patterns, and senses of displacement; the imaging of high-angle fault planes and horizontal fault separations on seismic reflection data; and the effects of strain partitioning that yield coeval strike-slip faults and associated fold and thrust belts.

Two magnitudes are used for the rupture scenarios on the Hosgri fault zone. The first is a magnitude 6.9 and the second a magnitude 7.2. We assign magnitude bins to these scenarios of 6.8 – 7.0, and 7.0 and greater, respectively. Two styles of faulting are considered for each magnitude: strike-slip (rake=7°) and reverse/oblique (rake=25°). The strike-slip style of faulting is slightly preferred (weight of 0.6) compared to the reverse/oblique case (weight of 0.4). Based on the LTSP model (PGE, 1988, Fig 3-14), the recurrence intervals of the M6.9 and M7.2 scenarios are 600 years and 2,000 years respectively.

The Santa Maria Slope Break Zone (SMSB) slide (Section 6.1), may be triggered by an earthquake on the Hosgri fault zone. Based on the longer recurrence interval for slides in the SMSB than the recurrence intervals for earthquakes on the Hosgri faults, we assume that 10 percent of the Hosgri characteristic earthquakes trigger a slide on the SMSB. The rate of earthquakes on the Hosgri fault is divided into the rate for rupture of the Hosgri fault that do not trigger slides on the SMSB and the rate for ruptures that do trigger slides on the SMSB. To preserve the total rate of earthquakes on the Hosgri fault, the recurrence intervals for an independent Hosgri earthquake are 10 percent larger than the long term rate: recurrence intervals for independent M6.9 and M7.2 scenarios are 660 years and 2,200 years respectively. The recurrence intervals for synchronous ruptures are 10 times the recurrence intervals for all ruptures on the Hosgri. For the M6.9 and 7.2 scenarios, the recurrence intervals for ruptures that trigger landslides are 6000 years and 20,000 years, respectively.

5.1.2 Santa Lucia Bank Fault

The Santa Lucia Bank fault zone is part of a 30-kilometer-wide anastamosing to en echelon zone of faults along the west margin of the offshore Santa Maria basin (Figure 5-1). The fault separates the offshore Santa Maria basin from the Santa Lucia high, a structurally uplifted block of Cretaceous rock (McCulloch and others, 1980; Richmond and others, 1981). The northern trace of the Santa Lucia Bank fault zone appears as an

85-kilometer-long linear sea floor escarpment that extends northwest from offshore Purisima Point to offshore Estero Bay. To the southeast, off Point Arguello, the fault zone consists of a number of splays having more westerly orientations. McCulloch and others (1980) and McCulloch (1987) provide several lines of evidence to suggest that lateral displacement has occurred along the Santa Lucia Bank fault zone. The evidence includes the long linear trace typical of lateral-slip faults; differences in the residual magnetic field across the fault, suggesting the juxtaposition of different basement rock types; the presence of a linear magnetic anomaly that probably represents an ophiolitic body at depth that does not cross the fault; and different thicknesses of Pliocene and Miocene units across the fault. They note this suggests that considerable strike-slip displacement accompanied vertical separation on the Santa Lucia Bank fault zone. McCulloch and others (1980) conclude the oblique trend of the basement structures between the Santa Lucia Bank fault zone and the Hosgri fault zone, and infilling during development of the structural lows accompanied by growth of normal faults and minor compression, suggest extension and sagging of the basement during transtensional wrenching throughout the Miocene.

Based on a fault length of 70 km and a down-dip fault width of 12 km, the characteristic magnitude is 7.0. Similar to the Hosgri fault zone, two M7 scenarios are considered: strike-slip (rake = 7) and reverse/oblique (rake=25). Using the Youngs and Coppersmith (1985) characteristic earthquake recurrence model, for a slip-rate of 0.2 mm/yr, the recurrence interval for M>6.75 earthquakes is 8600 years.

5.1.3 Purisima Structure

The Purisima and Lompoc structures form prominent antiformal uplifts in the southern part of the offshore Santa Maria basin (Figure 5-1). The antiformal uplifts in the southern part of the basin are bounded on one or both sides by Miocene normal faults that were reactivated in the Pliocene and Quaternary as moderately to steeply dipping thrust or reverse faults (PG&E, 1990; McIntosh and others, 1991; Meltzer and Levander, 1991). Seismic reflection profiles across the Purisima and Lompoc structures show strong evidence of imbricated thrust faults, post-early Pliocene folding, and locally, evidence of warping or folding of the sea floor (Lettis and Hanson, 1991; Willingham and others, 2006). The deformation of the sea floor indicates the Lompoc and Purisima structures are active Quaternary features.

The rate of vertical deformation measured on the early late Pliocene unconformity across both the Purisima structure and the Hosgri fault zone indicates a combined vertical slip rate of approximately 0.2 mm/yr (Hanson and others, 2005). The actual rate localized across only the Purisima fold is less, approximately 0.07 mm/yr, for example, as interpreted from the vertical separation of the early late Pliocene unconformity near Point Sal (Hanson and others, 2005). For this fault, we estimate of a dip of 30 degrees and we assume the motion to be purely thrust. The length of the fault is estimated to be 20 km, and the width 2 km. Using a 30 degree dip with pure thrust motion, the vertical slip rate of 0.07 mm/yr corresponds to a total slip-rate of 0.14 mm/yr.

The scenario earthquake assigned to this fault is a magnitude 6. A fully characteristic magnitude distribution is used with a characteristic earthquake of magnitude 6. Using the Youngs and Coppersmith (1985) characteristic earthquake recurrence model, for a slip-rate of 0.14 mm/yr, the recurrence interval for M>5.75 earthquakes is 4000 years.

5.1.4 Casmalia Fault zone

The Casmalia Hills are bordered by the Casmalia fault zone (also called the Orcutt Frontal fault) on the northeast, the Hosgri fault zone on the west, and the Lions Head fault on the southwest (Figure 4-1). Seismicity data, offshore seismic reflection data, and onshore geologic mapping show that the Casmalia and Lions Head fault zones are reverse fault zones that dip steeply beneath the Casmalia Hills (Lettis and others, 2004). Clark (1990) reports an uplift rate for the block between these faults of about 0.15 mm/yr based on uplifted marine terraces. Clark and others (1994) present two models to explain the uniform, block-style uplift and observed localized folding along the Casmalia fault zone and the minor reverse and normal displacements on the Lions Head fault zone: (1) continued anticlinal folding of the Casmalia Range above a listric blind thrust or reverse faults (similar to the model presented by Namson and Davis, 1990), or (2) uplift of a rigid structural block along high-angle reverse faults and localized drag folding at the surface along the Casmalia fault zone. Lettis and others (2004) favor the block uplift model, because the anticlinal folding model predicts rates of shortening (2-5 mm/yr) that far exceed observed rates of geologic deformation (0.15 mm/yr). They also point out that uniform block uplift rather than folding is documented by the marine and fluvial terrace record, and the nature and pattern of seismicity indicate high-angle reverse faulting. The NSHM assigns this fault a slip rate of 0.25 mm/yr.

The NSHM assign two characteristic earthquakes to the Casmalia fault zone, a magnitude 6.7 based on Ellsworth (2003) and a magnitude 6.5 based on Hanks and Bakun (2002), with equal weighting. Both the characteristic and Gutenberg-Richter magnitude frequency distributions are used, with weights of 0.67 and 0.33 respectively (NSHM). Magnitude recurrence rates are calculated by balancing the seismic moment using a slip-rate of 0.25mm/year and a fault area of 300.7km^2 (Petersen and others, 2008). One rupture scenario is used for the Casmalia fault zone with a magnitude of 6.7. We assign a magnitude to this scenario of 6.5 and greater. Using the magnitude recurrence rates described above, the recurrence interval of this scenario is 5330 years.

5.1.5 Queenie Structure

The Queenie structure is the largest-amplitude fold in the western offshore Santa Maria basin (Figure 5-1). It appears as a sea floor topographic feature approximately 34 km west of Point Sal. On the basis of stratigraphic and structural relationships interpreted from seismic reflection profiles and oil industry well data, Clark and others (1991) conclude the principal growth of the Queenie structure occurred between 5.3 and 3.4 million years ago (Ma), because the early late Pliocene unconformity is not significantly deformed across the fold. Minor late Quaternary folds in the sea floor adjacent to the Queenie structure, visible on seismic reflection profiles, are evidence of shortening post-3.4 Ma at a rate of 0.005 mm/yr. Clark and others (1991) conclude a reverse fault beneath the Queenie structure extends from the tip of the structure at a depth of approximately 1 km to the base of the seismogenic crust at a depth of 10 to 12 km. For this fault we estimate of a dip of 50 degrees and we assume the motion to be purely thrust. The length of the fault is estimated to be 20 km, and the width 12 km. Using this information, and the shortening rate of 0.005 mm/yr, we calculate the total slip on the fault to be 0.078 mm/year.

The scenario earthquake assigned to this fault is a magnitude 6.5. A fully characteristic magnitude distribution is used with a characteristic earthquake of magnitude 6.5. The earthquake recurrence interval for the scenario is 112,000 years.

5.1.6 1927 Lompoc Earthquake

Relocation of the earthquake by Helmberger and others (1992) based on analysis of teleseismic data moved the epicenter of the 1927 event from the southern end of the Hosgri fault (Gawthrop, 1978) to Arguello Canyon and the Southwest Channel fault (Figure 5-1). Satake and Somerville (1992) confirmed that the 1927 Lompoc earthquake

occurred beneath water depths of 1,000 m based on tsunami travel time calculations consistent with the location determined by Helmberger and others (1992). The 1927 Lompoc earthquake is estimated to have a median recurrence interval of 8,600 years based on a slip-rate of approximately 0.2 mm per year.

5.2 TSUNAMI MODELING

The results of the tsunami modeling for the local faulting are described for each fault source. The aleatory variability for tsunami waves from local faulting is assumed to be the same as for the distant earthquakes.

5.2.1 Hosgri Fault Zone

The ratio of horizontal to vertical slip is an important criterion used to evaluate the style of faulting along the Hosgri fault zone (Hanson and others, 2005). The ratio of horizontal to vertical slip is not constant along the fault zone, nor does it vary monotonically from north to south. The lateral slip rate of 1 to 3 mm/yr, which is transferred between the San Simeon fault zone and the northern part of the Hosgri fault zone, probably decreases progressively southward as slip is consumed by crustal shortening along the more westerly trending reverse faults and folds within the Los Osos domain (Lettis and others, 2004). Quantification of components of horizontal and vertical slip along the entire length of the Hosgri fault zone indicates ratios of horizontal to vertical slip of 1:1 to 30:1. The quantified rates of vertical slip incorporate the total amount of vertical deformation along the entire fault, including the upper crustal fold deformation related to the low-angle fault strands within the fault zone, as well as brittle fault deformation and folding associated with the high-angle fault strands. Based on the rake angles implied by these horizontal to vertical ratios, together with an estimate of fault dip, the Hosgri fault zone is classified as a strike-slip fault along most, if not all, its length. The uncertainties allow for the possibility the fault may have oblique slip in the southernmost reaches.

The source parameters for the Hosgri fault rupture scenario are based on the seismic source characterizations used in the LTSP probabilistic seismic hazard analysis (PG&E, 1988) and evaluations of the horizontal to vertical component of slip along the Hosgri fault zone (Hanson and others, 2005). The rupture scenarios for the Hosgri fault zone have the largest vertical displacements, 2 to 5 meters, of any of these faults. The Hosgri scenarios assume the fault is a convergent right-slip (transpressional) fault (Hanson and others, 2005).). Our current results comprise two different scenarios regarding the rake vector, 23° and 7°. The latter represent our current interpretation of these faults as

predominantly strike-slip faults, whereas the former is included because of the occurrence of higher rake angles in small earthquakes along this fault.

The high rake angle results for the Hosgri fault show only minor tsunami development at DCPP, with amplitudes of 0.75 m. The results for the 7° rake angle shows even smaller amplitudes.

5.2.2 Santa Lucia Bank Fault Zone

The characterization of the Santa Lucia Bank fault zone is based on the characterization in the LTSP (PG&E, 1988). The scenarios comprise two different rake vectors, 23° and 7°. The latter represent our current interpretation of the fault as predominantly strike-slip faults, whereas the former is included because of the occurrence of higher rake angles in small earthquakes along this fault. The fault parameters of the 1927 Lompoc earthquake, as defined by Helmberger and others (1992) and Satake and Somerville (1992), are used for the scenarios. Empirical relations of Wells and Coppersmith (1994) are used to estimate rupture parameters.

The high rake angle tsunami height results from the Santa Lucia Bank fault are on the order of 1.0 m (3.3 ft) at the discharge site. The results for the 7° rake angle shows even smaller amplitudes.

5.2.3 1927 Lompoc Earthquake

The 1927 Lompoc earthquake generated a small tsunami that was observed on tide gauge records at Fort Point (San Francisco) and La Jolla, California, and Hilo, Hawaii. The wave height was only about 5 cm at the California locations. In Hawaii, focusing and local bathymetric effects contributed to a wave height of 10 cm at Hilo.

The Lompoc earthquake tsunami provides the only observations of a known local earthquake-generated tsunami originating in the central-southern California offshore region and provides an opportunity to evaluate the bathymetry model used in our study. A comparison with recorded waves is within the expected uncertainty range, given that eyewitness accounts may be generally overestimated by a factor of 1.5 to 2 because of the difficulty in making an observation of the wave face relative to peak-to-trough or just peak breaking amplitude from sea level. A 1.8-m wave was observed at Surf, California near the town of Lompoc closest to the epicenter. The maximum wave height at the DCPP discharge site was calculated to be 0.34 m.

Table 5-1. Source parameters and tsunami wave heights for local tsunami from faults

Source	Mag. Bin	Scenario. Mag.	Recur. Interval (yrs)	Source Geometry					
				Length (km)	Width (km)	Strike	Dip (°)	Rake (°)	Weight
Hosgri Fault Zone	>7	7.2	2,200	100	12	-20	82	25	0.4
				100	12	-20	82	7	0.6
	6.8 - 7	6.9	660	70	12	-20	82	25	0.4
				70	12	-20	82	7	0.6
Santa Lucia Bank Fault Zone	>6.75	7	8,600	70	12	-22.2	82	25	0.4
				70	12	-22.2	82	7	0.6
Purisima Structure	>5.75	6	4,000	20	2	-36.5	30	90	1
Casmalia Fault Zone	>6.5	6.7	5,300	24	15	-64.9	51	90	1
Queenie Structure	>6.25	6.5	20,000	20	12	-34.7	50	90	1
Lompoc Earthquake	>6.75	7	1,300	30	15	340	66	95	1

Table 5-2. Source parameters and tsunami wave heights for local tsunami from faults

			Maximum Amplitude (m)		Minimum Amplitude (m)		Peak Velocity (m/s)		Peak Velocity at Maximum Amplitude (M/s)	
	Mag	Rake	Intake	Discharge	Intake	Discharge	Intake	Discharge	Intake	Discharge
Hosgri Fault Zone	7.2	25	0.62	0.86	-1.2	-0.16	1.1	1.0	0.10	0.25
		7	0.20	0.43	-0.37	-0.42	0.67	0.91	0.09	0.17
	6.9	25	0.45	0.33	-0.96	-0.44	0.9	1.3	0.10	0.33
		7	0.14	0.77	-0.27	-0.25	0.2	0.8	0.05	0.1
Santa Lucia Bank Fault Zone	7	25	0.74	0.35	-0.91	-0.51	1.4	1.2	0.36	0.32
		7	0.24	1.04	-0.29	-0.47	0.3	0.8	0.10	0.07
Purisima Structure	6	90	0.17	0.28	-0.05	-0.09	0.1	0.3	0.03	0.12
Casmalia Fault Zone	6.7	90	0.20	0.25	-0.01	-0.04	0.05	0.4	0.02	0.10
Queenie Structure	6.5	90	0.60	0.79	-0.73	-0.74	0.6	1.1	0.15	0.11
Lompoc Earthquake Repeat	7	95	0.34	0.34	-0.31	-0.38	0.82	0.35	0.66	0.01

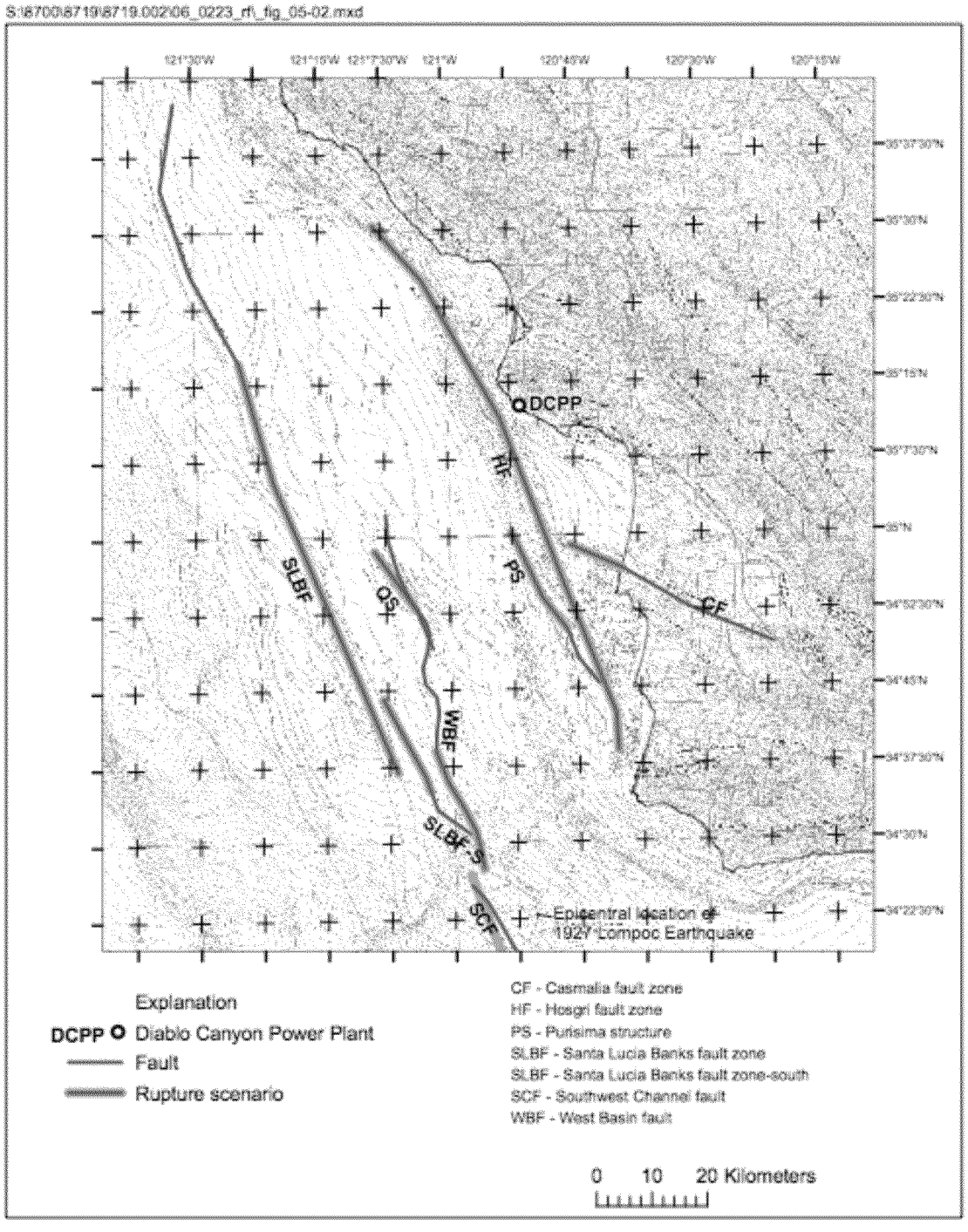

Figure 5-1 Map showing fault rupture scenarios used for the tsunami simulations.

SECTION 6

Local Tsunamis - Submarine Landslides

6.0 LOCAL TSUNAMIS - SUBMARINE LANDSLIDES

An extensive evaluation of potential sources of submarine landslides was conducted. Existing submarine landslides near the site were identified and evaluated for their potential for future landslide activity. The study region included the part of the central California continental margin between latitudes 34ºN and 36.5ºN, from Point Conception to Monterey Bay, and between longitudes 120ºW and 122ºW, extending from the shoreline to the base of the continental slope (Figure 5-1). The most detailed characterization efforts focused on the offshore area between the coastline and the Santa Lucia Escarpment in the central part of the study region adjacent to the DCPP site. A detailed description of the available data sets and evaluation of submarine landslides is given in PG&E (2010). In this section, a summary of the characterization of submarine landslides is given, focusing on the information that is needed for the PTHA

6.1 SUBMARINE LANDSLIDE CHARACTERIZATION

The tsunamigenic local slope failure source characterization is based on geomorphic sea-floor classification. The objective of the sea-floor classification is to identify regions having similar key characteristics that will provide guidance and constraint for developing a suitable range of reasonable input criteria for tsunami modeling. The characteristics include mechanisms of sediment transport and erosion (for example, translational/rotational slide, debris avalanche, debris flow), displacement mode (constant creep versus episodic stick-slip), and size of event (best assessment of average and maximum).

We divided the region into eight geomorphic domains based primarily on bathymetric information and known and inferred relationships between landforms, underlying geologic structure, and modes of sediment transport and erosion. The eight domains are (1) basin; (2) submarine canyon; (3) Santa Lucia Escarpment; (4) upper scarp facets; (5) nearshore platforms; (6) elevated rock platforms; (7) bathymetric scarps along the continental slope; and (8) non-faceted uplands along the continental slope. Further division of these eight domains according to geographic location increases the number of identified domains to 15. Of these 15 domains, 10 tsunamigenic local source failure source characterization regions were developed as shown in Figure 6-1. The source zones are summarized in Table 6-1 and the slide velocities are summarized in Table 6-2.

6.1.1 SANTA MARIA SLOPE BREAK ZONE (SMSB)

The SMSB zone is coincident with a tectonic scarp domain and it is associated with a thrust-related fold adjacent to the Hosgri fault zone. Bedding, which dips gently seaward, is steeper along the limb of this fold. Although anomalous features are identified along this slope break that may be related to some type of mass wasting, the characteristics of these are more consistent with erosional processes or downslope sediment movement in the shelf break region that likely occurs as intermittent creep, not as large-scale landslides.

The SMSB feature is mapped as a single, 30-kilometer-long slump (PG&E, 1989), but examination of the scalloped character of the slope break observed in the reprocessed near-shore bathymetry (Figure A7-5a) and D-series sheet bathymetry contours (Fugro West and others, 2005) suggests that individual slope failures would be more limited, and similar in scale to the Gaviota slide. It is assumed that failures could occur at locations along the entire length of the SMSB feature. Given the uncertainties in the size of potential individual failures, two different scale failures are modeled: a 2-kilometer-wide and 5-kilometer-wide failure. The smaller width is preferred (weight of 0.6) over the larger width (weight of 0.4) based on the scale of scallops observed along the slope break and comparison to the Gaviota slide. A single value of 2.6 kilometers, which is representative of the general downslope width of the zone, is used to estimate the length of the estimated failure. The thickness of the estimated landslides is constrained to be less than 20 meters based on the continuity of bedding observed in seismic data. A shallower slip plane at a depth of 8 meters is considered equally likely.

The triggering mechanism of the features in this region has two interpretations. The highest weight (0.7) is given to the interpretation that the features are due to non-landslide processes based on the lack of evidence in the seismic profiles to support rapid slumping. The lowest weight (0.3) is given to the interpretation that the features are tsunamigenic landslides, triggered by both strong ground motion from multiple seismic sources in the region as well as sedimentation and erosion processes that may have been linked temporally to periods of low sea level and the transition to higher sea level acting in the shelf-break region are likely triggers for slumping events. In the case where the features are tsunamigenic, the possibility that a landslide along the SMSB is triggered simultaneously with a surface fault rupture along the Hosgri fault zone, giving rise in some cases to larger tsunami waves, is given a weight of 0.1. The occurrence of a

tsunamigenic landslide independent of a rupture along the Hosgri fault zone is given a weight of 0.9.

Assuming tsunamigenic landslides occur along the SMSB, estimates of recurrence are based on indirect arguments regarding possible triggering events and the number and size of events that may be recorded along the zone. For independent slope failures, recurrence intervals of approximately 2,000 years (0.33), 5,000 years (0.34), and 100,000 years (0.33) are considered. These intervals are based on the assumption that there have been approximately four to ten events within the SMSB in post-Wisconsin time (~21,000 years ago). The longer recurrence interval of 100,000 years (0.33) assumes that slope failures within the SMSB are tied to periods of low sea level. For slope failures that occur simultaneously with events on the Hosgri fault zone, recurrence is linked to the recurrence of large magnitude (M>7) earthquakes on the Hosgri fault as described in Section 5.1.1. For the M6.9 and 7.2 scenarios, the recurrence intervals for ruptures that trigger landslides are 6000 years and 20,000 years, respectively.

6.1.2 SUR SHELF-BREAK ZONE (SSB)

The shelf break in the SSB is structurally controlled by the active Sur-Nacimiento fault, which is part of the regional San Gregorio-San Simeon-Hosgri fault system (Dickinson and others, 2005) and possible splays (McCulloch and Greene, 1990). Physiographically, this source zone includes the upper reaches of the Sur Canyon. Due to a lack of data, this area was not mapped in detail by McCulloch and Greene (1990). High-quality multibeam data (MBARI Mapping Team, 2000), however, does extend into this region, and no landslides comparable to the Gaviota or Goleta landslides have been observed in these data (Dr. H. Gary Greene, personal communication, April 10, 2006). The numerous headless channels that form the upper reaches of the Sur Canyon system, as imaged in the bathymetry data, appear to be migrating headward by canyon wall failures. These channels act as funnels for the rapid transport of detritus eroded from the Santa Lucia Mountains to the deep abyssal plain. Larger slide masses are exposed in the vicinity of the shelf break near the head of Partington Canyon. The general sea-floor roughness and level of dissection suggest that this zone is an active region of erosion. This zone also lies seaward of the high-relief Sur coastline and likely experiences high rates of sedimentation. Landslides are common along the steep coastal regions of Big Sur in Monterey and San Luis Obispo counties, particularly in the weak Franciscan and biotite-rich granitic rock along the coastline adjacent to the SSB zone (Wills and others, 2001; Hapke and Green, 2005 a, b). However, as noted by Dr. H. Gary Greene (personal

communication, April 10, 2006), the accumulated sediments on the shelf and upper slope in this region are generally coarser and less susceptible to failing as a large coherent mass than the types of sediments that are present along the shelf-break region in the Santa Barbara channel.

Two alternatives for the area of the largest expected slides are considered. The morphology of the sea floor in this zone suggests that landslide failures having headscarp widths of about 2 kilometers or 3 kilometers are possible. The downslope length of the postulated failure is unknown, but is assumed to be approximately twice the estimated width. This is consistent with the general aspect ratios (W:L of 1:1.4 to 1:2.6) of the slides observed within the Santa Barbara channel. The smaller width of 2 kilometers is preferred (weight of 0.6) over the larger width of 3 kilometers (weight of 0.4) because the smaller size is more consistent with observations of the scale of recognized slide masses in the upper part of the Partington submarine canyon. Three alternative slide thicknesses of 50, 70, and 100 m are considered with weights of 0.4, 0.4, and 0.2, respectively. The smaller thicknesses are preferred because it is likely that erosion and sediment transport via the submarine canyons reduces the amount of sediment available for failure and, large blocks of material are less likely to fail as coherent landslide blocks due to the coarse texture of the sediments.

There is considerable uncertainty in estimates of the timing and recurrence of slope failures in this zone. The recurrence intervals estimated below are for a landslide in the SSB region (e.g. a slide occurring at any of the five locations). Given the absence of significant slope failures comparable to the Gaviota and Goleta slides in the Holocene, a minimum recurrence interval of 10,000 years is given a weight of 0.4. Conditions more favorable to slope failures may occur during periods of lower sea level during glacial maximums when sediment is transported farther out onto the shelf or when climatic conditions are more conducive to higher rates of sedimentation or erosion by sea-floor currents. In this case, the recurrence interval for larger slope failures may be longer, on the order of 100,000 years (weight 0.2). An intermediate length interval of 50,000 years is also considered with a weight of 0.4.

6.1.3 ARGUELLO-CONCEPTION ZONE (ACZ)

The ACZ exhibits many of the same characteristics as the shelf-break upper slope region of the Santa Barbara channel along which several landslides have occurred, including the Gaviota slide and Goleta slide complex. This zone lies within a region of compression

marked by numerous folds and thrust faults. The linear steep shelf break between Point Arguello and Point Conception is coincident with a fault and appears to be in the hanging wall of a thrust fault, suggesting that underlying strata may be favorably inclined for failure. The overall relief across the zone ranges from approximately 500 to 600 meters with an average slope of 4° to 5°. Observations of post-late Wisconsin sediment thickness indicate that the sediment at the shelf-break region near Point Arguello is approximately 40 meters and decreases toward the southeast between the canyon heads and Point Conception to a thickness of less than 10 meters (PG&E, 1988). The mapped slides in the zone generally are small slides within the canyons and a retrogressive slide complex in the upper slope region west of Point Conception that appears to be comprised of three distinct mudflows (unpublished mapping, Dr. H. Gary Greene, written communication, August 17, 2006).

The estimated parameters for minimum size events (2 km wide x 3 km long x 10 m thick) and median size events (3 km wide x 4 km long x 10 to 35 m thick) are based on the sizes of observed landslides within the zone and thickness of accumulated sediments in the vicinity of the shelf break. A failure of the headscarp region of one of the Arguello Canyon failures is considered, although mass-wasting features seen in these canyons are more likely slowly moving, probably from subterranean flow of fluids escaping from the underlying hydrocarbon basin (Dr. H. Gary Greene, written communication, August 19, 2006). The maximum size event (6 km x 6 km x 10 to 35 m) assumes that a slope failure comparable to the simultaneous failure of an area the size of two of the lobes of the Goleta slide could occur in the future. It is possible that continued upslope failures of the Point Conception slide complex could trigger a larger slope failure in the vicinity of a smaller landslide that is present at the slope break.

The timing and recurrence of landslides in this region is not known. Maximum-size events comparable to the Goleta slide events are not recognized at the surface, suggesting recurrence of these events is longer than 10,000 to 20,000 years. Linking recurrence to glacial cycles could suggest a recurrence interval on the order of 100,000 to 200,000 years. The recurrence for maximum size events, therefore, is modeled as 15,000 years (weight 0.2), 50,000 years (weight 0.4), 100,000 years (weight 0.2) and 200,000 years (weight 0.2). The evidence for approximately 20 or more smaller mudslides and slides within the canyons (some of which may be smaller than the scenario events) suggests that smaller canyon failures and mudslides may occur more frequently (on average about one per 1,000 years assuming the 20 events occurred since the post-Wisconsin lowstand

(21,000 years ago). The recurrence for minimum-size scenario events is modeled as 1,000 years (weight 0.5) and 2,000 years (weight 0.5). For median-size events, longer recurrence intervals of 2,000 years (0.3), 5,000 years (0.4), and 10,000 years (0.3) are modeled to account for the fewer events of the size that are expressed in the sea bottom morphology (PGE, 2010).

6.1.4 SANTA LUCIA BANK SCARP ZONE (SLBS)

The SLBS east-facing scarp is tectonically controlled by the Santa Lucia Bank fault, a Miocene transtensional fault that appears to have been reactivated as a transpressional fault in the present tectonic stress field. Relief along the scarp is low, decreasing from a maximum of about 150 meters at the southern end of the zone where the maximum slope angle is <9° to less than 50 to 75 meters at the northern end of the zone where the slope angle is <5°. Much of the scarp is underlain by sedimentary rock of Pliocene age (McCulloch, 1989). No slope failures were previously mapped along the scarp by McCulloch (1989). A possible buried debris flow deposit observed in the seismic data at the southern end of the scarp likely formed in the Miocene transtensional period when the scarp likely was higher and more active. There is no obvious headscarp for this debris flow as the Santa Lucia Bank area above the scarp consists of a beveled Pliocene surface.

Given the low potential for generating a landslide, this source is not considered further in this study.

6.1.5 LOWER SLOPE CANYON ZONE (LSC)

The LSC includes a bowl-shaped erosional embayment localized along a submarine canyon that dissects the lower continental slope region north of the Morro promontory. The channel morphology is best expressed in the very limited areas where multibeam bathymetry data are available. It is expected that rates of deposition and erosion will be greater in the channel area than in the surrounding regions of the upper continental slope. Landsliding and slumping due to undermining of the channel margins is the expected mechanism of failure.

The size of possible slope failures (2.5 to 5 km wide and 5 km long) is roughly estimated from the sea-floor morphology, which is not well resolved in this region. The two slide dimensions are given equal weight. There are no seismic lines perpendicular to the slopes in this source zone from which to evaluate the thicknesses of future slope failures or the actual steepness of the channel margins. Values of 25 meters and 50 meters are

reasonable thickness values given the general relief of the channel margins (150 to 200 m) and low slopes (1.2° to 3°) in this zone. These two slide thicknesses are given equal weight.

In the absence of direct evidence that such failures have occurred, the recurrence estimate for the LSC is based in part on the recurrence data developed for the adjacent reach of the Santa Lucia Escarpment (ENZ). It is assumed that the two zones may be characterized by similar sedimentation rates and geologic conditions that may influence slope failures. However, to account for the limited data available to document the existence or timing of slide failures in this zone, shorter intervals that consider the possibility of greater channel incision and erosion that may trigger slope failures in this zone also are included. The recurrence is modeled as 20,000 years, 50,000 years, 100,000 years, 200,000 years and 400,000 years using equal weights.

6.1.6 SOUTHERN SANTA LUCIA BASIN ZONE (SSL)

The SSL zone coincides with a tectonic scarp that is underlain by probable active reverse faults of the Santa Lucia basin fault system. Previous slope failures are inferred to have occurred within this zone based on the morphology of the sea-floor bottom and evidence for landslide deposits interpreted from USGS Bartlett seismic data. The relief (~500 m) and slope (~5°) of this zone are greater than for the LSC zone, and thus it is judged more likely that slope failures will occur in this zone.

The slide dimensions used for this zone are the same as those assigned to the LSC zone: slide widths of 2.5 and 5 kilometers with equal weight and a slide length of 5 kilometers. Thicknesses of 25 and 50 m are given equal weight for these slides.

In the absence of direct evidence for recurrence of large slides on the SSL zone, the recurrence is estimated to be similar to that assigned to the LSC zone, with the exception that the longer recurrence value is not included. The recurrence is modeled as 20,000 years, 50,000 years, 100,000 years, and 200,000 years using equal weights.

6.1.7 NORTHERN SUR ESCARPMENT ZONE (ENSZ)

The ENSZ includes that portion of the escarpment between the Monterey Canyon to the north and Sur Canyon to the south. The Sur Slide (SS), a recognized large landslide on the lower continental slope in the northern part of the zone, is modeled as a single failure based on the inferred size of the landslide mass as described by Gutmacher and Normark

(1993). This slide is considered a possible analog for the maximum size failure that may occur elsewhere along the lower continental slope of the Santa Lucia Escarpment. Within the southern part of this zone, multiple slide deposits near the mouths of the Sur and Lucia canyons attest to additional large-scale landslides.

For the ENSZ zone, larger Sur Slide-scale events (10 km wide and 10.5 km long) with a weight of 0.5 are considered in addition to a smaller 5-kilometer-wide x 7-kilometer-long slide with a weight of 0.5. For the 10-kilometer x 10.5-kilometer slides, thickness of 75, 100, and 125 meters are used (weights 0.2, 0.6, 0.2). For the 5-kilometer x 7-kilometer slides thicknesses of 25, 50, and 100 meters are considered, with weights of 0.2, 0.6, and 0.2, respectively.

The number and ages of surficial and buried debris flows on the lower part of the escarpment and abyssal plain provide a basis for estimating the recurrence of large landslides along the escarpment during the past 1 to 2 million years. From these data it appears that the average recurrence interval between events on the ENSZ has been approximately 150,000 years. This average recurrence value is given the highest weight (0.6) in the hazard assessment, with values half and twice the average given a weight of 0.2 .

6.1.8 NORTHERN ESCARPMENT ZONE (ENZ)

The ENZ part of the Santa Lucia Escarpment exhibits ~1200 meters of relief and an average slope of 11°-13°. This part of the escarpment is mantled by sediment that exhibits dip-slope conditions. Although the lateral extent of landslide deposits on the abyssal plain is generally shorter than observed for the Sur Slide, there is evidence for large landslides in the seismic data.

Similar to the ENSZ, for the ENZ larger Sur Slide-scale events (10 km wide and 10.5 km long) with a weight of 0.5 are considered in addition to the smaller 5-kilometer-wide x 7-kilometer-long slide with a weight of 0.5. For the 10-kilometer x 10.5-kilometer slides, thicknesses of 25, 50, and 100 meters are used (weights 0.2, 0.6, 0.2). For the 5-kilometer x 7-kilometer slides, thicknesses of 25, 50, and 100 meters are considered, with weights of 0.2, 0.6, and 0.2, respectively.

The number and ages of surficial and buried debris flows on the lower part of the escarpment and abyssal plain provide a basis for estimating the recurrence of large

landslides along the escarpment during the past 1 to 2 million years. From these data it appears that the average recurrence interval between events on the ENZ appears to be slightly longer (~200,000 years). This average recurrence value is given the highest weight (0.6) in the hazard assessment, with values half and twice the average given a weight of 0.2.

6.1.9 CENTRAL ESCARPMENT ZONE (ECZ)

The ECZ part of the Santa Lucia Escarpment is identified as a separate zone based on the geometry of the escarpment and the presence of structures within the Santa Lucia Slope fault zone at the upper part of the escarpment which, if active, could potentially trigger a larger slope failure. This zone also has a moderate to high potential for generating landslides. There is a greater amount of sedimentation localized in this region by the channel system that originates in the upper part of the Santa Lucia basin along the western margin of the Santa Lucia Bank. Larger slope failures are indicated by the morphology and by the record of debris flows on the abyssal plain imaged in the seismic data.

Three slides are considered for the ECZ zone. A (10 km wide and 15 km long) event, a Sur Slide-scale event (10 km wide and 10.5 km long) and a smaller 5-kilometer-wide x 7-kilometer-long slide. These slide areas are given weights of 0.2, 0.4 and 0.4 respectively. For the 10-kilometer x 15-kilometer slides and the 10.5-kilometer x 10-kilometer slides the thicknesses are estimated to be: 25, 50, and 100 meters, with weights of 0.2, 0.6, and 0.2, respectively. For the 5-kilometer x 7-kilometer slides, thicknesses of 25, 50, and 100 meters are considered, with weights of 0.2, 0.6, and 0.2, respectively.

The number and ages of surficial and buried debris flows on the lower part of the escarpment and abyssal plain provide a basis for estimating the recurrence of large landslides along the escarpment during the past 1 to 2 million years. From these data it appears that the average recurrence interval between events on the ECZ, similar to the ENSZ, has been approximately 150,000 years. This average recurrence value is given the highest weight (0.6) in the hazard assessment, with values half and twice the average given a weight of 0.2.

6.1.10 SOUTHERN ESCARPMENT ZONE (ESZ)

Although the ESZ part of the Santa Lucia Escarpment is higher ~2200 to 2600 meters and slightly steeper (13° to 15° overall, with parts of the slope exceeding 25°), this part of

the escarpment is characterized by the lack of a significant sediment cover and the lack of bedding dips favorable for landsliding. It appears that sediment is trapped behind the Santa Lucia Bank within the offshore Santa Maria basin in the upper slope region. The southern part of the escarpment (ESZ) appears to have experienced subsequent Miocene strike-slip deformation in contrast to the escarpment region to the north of Morro promontory. Miller and others (1992) speculate that rapid dewatering of the subduction wedge during this period of deformation allowed the steep-sloped southern escarpment to form. The sediment record preserved on the abyssal plain also suggests that landslides along this part of the escarpment are smaller and less frequent than to the north. This zone, therefore, is judged to have a low to moderate potential for generating a landslide.

Based on the general dimensions of these possible previous slide masses interpreted from the sea-floor morphology as rendered in the bathymetry DEM, scenario events that might occur along the ESZ are estimated to be approximately 5 kilometers wide and 7 kilometers long (weight of 1.0). Due to the limited sediment thickness observed along the ESZ, slide thicknesses of 25, 35, and 50 meters are considered, with weights of 0.2, 0.6, and 0.2, respectively.

The number and ages of surficial and buried debris flows on the lower part of the escarpment and abyssal plain provide a basis for estimating the recurrence of large landslides along the escarpment during the past 1 to 2 million years. From these data it appears that the average recurrence interval between events on the ESZ appears to be similar to the ENZ (~200,000 years), with events on the ESZ being smaller and possibly less frequent. This average recurrence value is given the highest weight (0.6) in the hazard assessment, with values half and twice the average given a weight of 0.2.

6.1.11 PISMO FEATURE

The triangular-shaped 'Pismo feature' covers an approximately 115 km^2 area of the upper continental slope offshore of DCPP. The upper continental slope extends from the base of the shelf break, at a water depth of approximately 200 m, to the western margin of the Santa Lucia Bank where the water depth is about 1000 m. The 'Pismo feature' is approximately 15 km long, extending from an upper apex at a water depth of approximately 335 m to water depths of a little over 550 m. The maximum width of the feature, which occurs in the lower part at water depths between 500 to 550 m, is a little over 14 km.

Representative slope-perpendicular marine seismic reflection records show the hummocky sea floor character of the 'Pismo feature'. In an earlier report, McCulloch and others (1980) describe the 'Pismo feature' as a series of "discreet blocks of sediment that have been rotated downward on their up-slope edges along slip surfaces. The slip surfaces appear to merge downward with unbroken seismic reflectors that parallel the general slope of the seafloor. The slide geometry suggests progressive slumping along a buried failure zone or surface". McCulloch's later mapping (McCulloch, 1989) shows the 'Pismo feature" as a landslide slump. The proximity of the 'Pismo feature' to zones of gas charged sediments suggests that gas within the sediments may decrease the shear strength of the sediments - promoting lateral spreading and liquefaction types of failure that result in *little or no lateral displacement*.

There are morphologic and geologic similarities between the 'Pismo feature' and the 'Humboldt slide' in northern California. Both features were initially interpreted as retrogressive, shear-dominated submarine slides that had undergone *limited* movement (Gardner and others, 1999; McCulloch, 1989). Both features are located in areas of gas charged sediments. More recent high resolution seismic imaging and AMS measurements, however, indicated that the 'Humboldt slide' had a depositional (sand waves) rather than slope failure (slumping) origin. No high resolution seismic or AMS data are available to determine the fine scale stratigraphic structure of the 'Pismo feature' and it is not possible to exclude the possibility that slow down-slope sediment creep or in-place rotation and slumping of discrete sediment packages has contributed to the formation of the feature. Nevertheless, these types of slope and liquefaction failures appear to have resulted in *little or no lateral displacement*, and therefore would not lead to the development of a significant ocean disturbance or tsunami. The 'Pismo feature' is judged to have a low potential for generating a landslide tsunami and is not considered further in this study

6.2 SUBMARINE LANDSLIDE GENERATED TSUNAMI MODELING

The wave heights for 114 individual landslide scenarios were numerically simulated using shallow water long wave hydrodynamic wave equations (see Appendix 2). For the tsunami modeling, four parameters are needed for each slide: location, length, width, thickness, and slide velocity.

The slide velocities were computed using bathymetric profiles across the region of the slides to simulate the realistic effects of gravitational acceleration. The average velocity across the profile is chosen as the slide velocity for the tsunami modeling.

The slide velocity depends on the average slope, maximum slope, and coefficient of friction. The coefficient of friction is shown to have a linear relation with average slope. We assume a coefficient of friction to start the block in motion.

The individual slides modeled, including the direction of the slides are shown in Figure 6-2.

6.2.1 Santa Maria Slope Break Zone (SMSB)

Twenty slide scenarios of various sizes, speeds, and locations were analyzed. Out of the 20 scenarios, only 1 (scenario 18) produced wave amplitudes at the DCPP intake (2.4 m, 7.9 ft) and discharge (3.6 m, 11.8 ft) of any significance. The results are listed in Table 6-3. Scenario 18 is located closest to the DCPP sites and has the largest dimensions of the scenario events modeled along the SMSB. The breakwaters were inundated (toppled by waves) in 50 percent of these cases. The slide velocity for the SMSB scenario events is modeled as 3, 8, and 18 m/s with weight of 0.2, 0.6, and 0.2, respectively based on the slope profile and drop heights.

In this section, several combinations of slides triggered as a result of a Hosgri earthquake are considered. A range of models consisting of a combination of the Hosgri fault model and the middle SMBS slide were analyzed, with difference in initiation times varying from 0 to 120 s. Wave heights are on the order of 4 to 5 m (13 to 17 ft) for a range of models, which is higher than the majority of slide or fault scenarios modeled individually. These scenarios are on the high end of our range since the slide location that would give the highest individual amplitudes at the site was used in the analysis. Of course, other slide zones might be activated by an event on the Hosgri fault, but those waves would arrive at DCPP well after the initial waves from the Hosgri fault would have passed, and therefore, those scenarios (e.g., Hosgri + ESZ) would yield a maximum amplitude that would be similar to the maximum amplitude of the largest of the two scenarios.

6.2.2 Sur Shelf Break Zone (SSB)

Twenty scenario slides were modeled. Typically, the tsunami wave heights from the SSB slides are in the 1-m range at the sites; 11 of the 20 scenarios generated tsunami wave heights greater than 1 m. An east-west-trending canyon incises the Big Sur coast, and the slides at this location are limited to the northern side of this canyon before decelerating up the southern canyon slope. The slide may continue down the canyon floor, but will likely break up in the process into a turbidity flow rather than an intact slide. Based on the slope profile and drop heights, the slide velocity for the SSB scenario events is modeled as 19, 30, and 46 m/s with weights of 0.2, 0.6, and 0.2, respectively.

6.2.3 Arguello-Conception Zone (ACZ)

Seven scenario locations in this zone were modeled. Based on the slope profile and drop heights, the slide velocity for the ACZ scenario events is modeled as 10 m/s and 30 m/s with equal weights.

Six of the seven scenarios yield wave height that are well below the 1 m level, and in many cases less than half a meter. The largest wave heights are from scenario 7, causing a wave height of 1.3 m at the discharge and 0.84 m at the intake site.

6.2.4 Lower Slope Canyon Zone (LSC)

The slides in this zone are modeled with thicknesses of either 25 or 50 m, and widths of 2.5 km and 5 km. A length of 5 km is used in all cases. The slide velocities are low, ranging between 1 and 31 m/sec. In this area, a canyon cuts through the slope, thereby causing instability but limiting the slide runout potential to just one side of the canyon. With these modest dimensions, very small tsunami amplitudes of < 1 m (3.3 ft) at the intake and discharge sites are computed. Given the small wave heights from the LSC slides, this source is not included in the PTHA.

6.2.5 Southern Santa Lucia Basin Zone (SSL)

Twenty scenario SSL slides were analyzed. These slides occur along a relatively steep slope and have relatively long runout distances (as high as 30 km), but have relatively small dimensions (less than 5 km by 5 km and thicknesses less than 25 m) compared to the larger slides modeled along the escarpment zones. The slide velocity for the SSL scenario events is modeled as 20 m/s and 40 m/s with equal weights based on the slope profile and drop heights. These scenarios all produce tsunami amplitudes less than 1 m,

except for one case where the tsunami reached 2 m at the discharge site. Given the small wave heights from the SSL slides, this source is not included in the PTHA.

6.2.6 Northern Sur Escarpment Zone (ENSZ)

The Sur Slide (ENSZ-N) is northernmost of the regional slides that we modeled. The ENSZ zone has a sliding velocity of 68 m/s. Even though it is the most distant scenario from DCPP, the ENSZ-N scenarios still yield wave heights of up to 4.5 m at the discharge and intake structures (Tables 6-3, 6-4). The slide scenario, assuming a 100-m thickness, generates a significant wave at DCPP discharge site of 4.1 m but only a 2.6-m amplitude at the intake site (Table 6-3)

6.2.7 Southern Santa Lucia Basin Zone (SSL)

Six scenarios at two locations in the Northern Santa Lucia Escarpment Zone (ENZ-N and ENZ-S) were run. These slides all have high velocities > 50 m/s and as high as 93 m/s, but only three scenario slides with the largest dimensions generated significant tsunamis (> 3 m) in amplitude at DCPP intake (4 m) and discharge (6.7 m) sites (Table 6-3).

6.2.8 Central Escarpment Zone (ECZ)

Six scenarios were run for the ECZ. The largest tsunami wave height is 9.5 m at the discharge structure from scenario 4 of ECZ. The ECZ zone has a sliding velocity of 52 m/s. The largest wave height at the intake structure is 6.9 m from scenario 6 of ECZ. As an example, the wave form for the tsunami at the intake structure for ECZ case 6 is shown in Figure 6-3. This is one of the largest waves.

6.2.9 Southern Escarpment Zone (ESZ)

Two scenarios were run for the ESZ. Although the ESZ scenario events are smaller and thinner than events modeled on the northern parts of the escarpment, they have the steepest slope from the breakaway point that yields a velocity of 103 m/s.

6.3 MAXIMUM WAVE HEIGHT MODEL

6.3.1 MEDIAN MODEL FOR LANDSLIDE-GENERATED TSUNAMIS

For use in the PTHA, parametric models were fit to the computed maximum wave heights for the intake and discharge. The simulations indicate that slide thickness,

dimension, and velocity have the greatest effect on tsunami generation. The thickness and dimension are important because slide thickness translates to potential tsunami energy and dimension relative to water depth translates into wavelength, where longer wavelengths propagate energy more efficiently.

The ln(Max wave height) was fit to a constant value for each slide. The residuals from this initial model were evaluated for their dependence on the slide area, slide thickness, and slide velocity. The wave height scales strongest with the slide thickness and slide velocity. These results are consistent with findings from other studies (e.g., Watts, 2004). Based on these plots of the residuals, the dependence of the slide area, slide thickness, and slide velocity were added to the wave height model. The wave height is modeled by:

$$\ln(WaveHeight(m)) = \sum_{i=1}^{Nsource} a_i E_{ij} + b \ln(V / Vref_i) + c \ln(A / Aref_i) + d \ln(H / Href_i) \quad (6\text{-}1)$$

where E_{ij} is a dummy variable that is 1 if the j^{th} simulation is for the i^{th} source and 0 otherwise. The V, A, and H are velocity, area, and thickness, respectively; and $Vref_i$, $Aref_i$, and $Href_i$, are the average values used in the simulations for each source. The parameters a_i, b, c, and d are determined using ordinary least-squares.

The estimated parameters for the intake and discharge are listed in Tables 6-5 and 6-6, respectively. An example of the dependence of the wave height on slide velocity and slide thickness is shown in Figure 6-4 for the SMSB/ ECZ source.

6.3.2 ALEATORY VARIABILITY FOR LANDSLIDE-GENERATED TSUNAMIS

The standard deviation of the natural log wave height from the modeling is 0.46 for both the intake and the discharge. This is a lower estimate of the total aleatory standard deviation because it only includes the misfit between the parametric model and the simulated wave heights and does not include the contribution due to the variability between the numerical model estimates and the actual wave heights. For the earthquake sources, the aleatory variability should be smaller than for the landslides tsunamis because the relevant earthquake source parameters are less variable than the relevant slide source parameters. For landslide tsunamis, the total standard deviation of the wave height is assumed to be 0.7 natural log units based on a standard deviation of 0.46 from the regression and an assumed modeling variability standard deviation of 0.5 for the misfit between the numerical simulations and the actual wave heights for landslide

tsunamis. This is larger than the average of 0.6 natural log units estimated for the earthquake-generated tsunamis (Section 4.2.1).

We estimated an aleatory standard deviation of 0.7 for landslides generated tsunamis with an epistemic uncertainty of 0.1 natural log units. Three values of the aleatory variability and weights (in parentheses) were selected: 0.6 (0.2), 0.7 (0.6), and 0.8 (0.2). There are no wave height observations from local landslides that can be used to estimate the modeling variability and the bias of the numerical model. Given this lack of data, the epistemic uncertainty in the numerical model for slides should be larger than for earthquake-generated tsunamis. The epistemic uncertainty for the bias from earthquake-generated tsunamis is 0.1 natural log units. Therefore, we assume that the uncertainty in the bias for landslide-generated tsunamis is 0.25 natural log units. With the commonly used three point distribution, bias values of -0.4, 0.0, and 0.4 natural log units with weights of 0.2, 0.6, 0.2, respectively, are selected. These correspond to factors of 0.7, 1.0, and 1.5 on the median value from numerical simulations of landslide-generated tsunamis.

6.4 DRAWDOWN MODEL

For the drawdown, the minimum amplitude from the landslides is modeled using the functional form shown in eq. 6-1. The drawdown only impacts the intake. Therefore, only the intake drawdown is modeled. The estimated parameters for the intake drawdown are given in Table 6-7.

6.5 PEAK VELOCITY MODEL

The peak velocity is correlated with the wave height. Therefore, instead of developing an independent model for the peak velocity for use in PTHA, a model for the ratio of the peak velocity to the wave height is developed. This model can then be applied to the wave heights from the PTHA to develop the peak velocities for a given probability level that are consistent with the maximum wave height.

For this evaluation, the ratios of the peak velocity to maximum wave height from the distant and local earthquakes are combined with the ratios from the landslides. Two peak velocities are considered: the peak velocity during the tsunami and the peak velocity that

occurs at the time of the peak amplitude. Models are developed for both of these parameters.

The velocity to wave height ratio is fit to a quadratic functional form. For application, the model will need to be extrapolated outside of the range constrained by the numerical simulations. The model assumes a linear extrapolation beyond the range of the data . The resulting model form is given by:

$$\ln(vel) = \begin{cases} b_1 + b_2 \ln(W_{tsu}) + b_3 \ln(W_{tsu})^2 & for W_{tsu} < W_1 \\ b_1 + b_2 \ln(W_1) + b_3 \ln(W_1)^2 + \left(b_2 + 2b_3 \ln(W_1)\right) \ln\left(\frac{W_{tsu}}{W_1}\right) & for W_{tsu} \geq W_1 \end{cases}$$

The coefficients were estimated using ordinary least-squares. Four sets of coefficients are listed in Table 6-8 corresponding to the intake and discharge sites for the two peak velocity parameters. The median model and the data for the four cases are shown in Figures 6-5 to 6-8.

Table 6-1. Source Parameters for local submarine landslides

Source	Recurrence Interval (weight)	Length (km)	Width (km)	Weight	Thickness (m)
Santa Maria Slope Break Zone (SMSB)	Independent 2000 (0.33) 5000 (0.34) 100,000 (0.33) Simultaneous with Hosgri – see Section 5	2.6	2	0.6	8 (0.5) 20 (0.5)
		2.6	5	0.4	8 (0.5) 20 (0.5)
Sur Shelf-Break Zone (SSB)	10,000 (0.4) 50,000 (0.4) 100,000 (0.2)	4	2	0.5	50 (0.5) 100 (0.5)
		6	3	0.5	50 (0.5) 100 (0.5)
Arguello-Conception Zone (ACZ)	1,000 (0.5) 2,000 (0.5)	3	2	1	10
	2,000 (0.3) 5,000 (0.4) 10,000 (0.3)	4	3	1	10 (0.5) 35 (0.5)
	15,000 (0.2) 50,000 (0.4) 100,000 (0.2) 200,000 (0.2)	6	6	1	10 (0.5) 35 (0.5)
Lower Slope Canyon Zone (LSC)	20,000 (0.2) 50,000 (0.2) 100,000 (0.2) 200,000 (0.2) 400,000 (0.2)	5	2.5	0.6	25 (0.6) 50 (0.4)
		5	5	0.4	25 (0.6) 50 (0.4)
Southern Santa Lucia Basin Zone (SSL)	20,000 (0.25) 50,000 (0.25) 100,000 (0.25) 200,000 (0.25)	5	2.5	0.6	25 (0.5) 50 (0.5)
		5	5	0.4	25 (0.5) 50 (0.5)
Northern Sur Escarpment Zone (ENSZ)	75,000 (0.2) 150,000 (0.6) 300,000 (0.2)	7	5	0.6	25 (0.2) 50 (0.6) 100 (0.2)
		10.5	10	0.4	75 (0.2) 100 (0.6)

Source	Recurrence Interval (weight)	Length (km)	Width (km)	Weight	Thickness (m)
					125 (0.2)
Northern Escarpment Zone (ENZ)	100,000 (0.2) 200,000 (0.6) 400,000 (0.2)	7	5	0.6	25 (0.2) 50 (0.6) 100 (0.2)
		10.5	10	0.4	75 (0.5) 100 (0.50)
Central Escarpment Zone (ECZ)	75,000 (0.2) 150,000 (0.6) 300,000 (0.2)	7	5	0.2	25 (0.2) 50 (0.6) 100 (0.2)
		10	10	0.6	25 (0.2) 50 (0.6) 100 (0.2)
		15	10	0.2	25 (0.2) 50 (0.6) 100 (0.2)
Southern Escarpment Zone (ESZ)	100,000 (0.2) 200,000 (0.6) 400,000 (0.2)	7	5	1	25 (0.2) 35 (0.6) 50 (0.2)

Table 6.2 Slide Velocities for Submarine Landslides

Source	Slide Velocity (m/s) (weight)
Santa Maria Slope Break Zone (SMSB)	3 (0.2) 8 (0.6) 18 (0.2)
Sur Shelf-Break Zone (SSB)	19 (0.2) 30 (0.6) 46 (0.2)
Arguello-Conception Zone (ACZ)	10 (0.5) 30 (0.5)
Lower Slope Canyon Zone (LSC)	1-31
Southern Santa Lucia Basin Zone (SSL)	20 (0.5) 40 (0.5)
Northern Sur Escarpment Zone (ENSZ)	68 (1)
Northern Escarpment Zone (ENZ)	85 (1)
Central Escarpment Zone (ECZ)	52 (1)
Southern Escarpment Zone (ESZ)	103 (1)

Table 6-3. Tsunami Modeling Results for Submarine Landslides at the Intake Structure

Source	Case	Length (km)	Width (km)	Height (m)	Slide Velocity (m/s)	Long	Lat	Strike	Max amp	Min Amp	Peak Velocity (m/s)	Peak Velocity at Max Amp (m/s)
SMSB	1	2.6	2	8	13	238.982	35.3564	160	0.46	-0.70	0.81	0.61
SMSB	2	2.6	2	8	1	239.018	35.2524	160	0.03	-0.03	0.03	0.00
SMSB	3	2.6	2	8	12	239.073	35.1696	160	0.45	-0.74	0.83	0.12
SMSB	4	2.6	2	8	7	239.117	35.1191	160	0.19	-0.16	0.24	0.15
SMSB	5	2.6	2	8	25	239.143	35.063	160	0.22	-0.18	0.20	0.11
SMSB	6	2.6	2	20	13	238.982	35.3564	160	0.77	-0.89	1.11	0.56
SMSB	7	2.6	2	20	1	239.018	35.2524	160	0.07	-0.06	0.11	0.01
SMSB	8	2.6	2	20	12	239.073	35.1696	160	1.24	-1.25	1.38	0.41
SMSB	9	2.6	2	20	7	239.117	35.1191	160	0.40	-0.40	0.58	0.45
SMSB	10	2.6	2	20	25	239.143	35.063	160	0.51	-0.32	0.74	0.35
SMSB	11	2.6	5	8	13	238.982	35.3564	160	0.57	-0.78	0.95	0.42
SMSB	12	2.6	5	8	1	239.018	35.2524	160	0.04	-0.04	0.03	0.02
SMSB	13	2.6	5	8	12	239.073	35.1696	160	0.86	-1.04	1.28	0.33
SMSB	14	2.6	5	8	7	239.117	35.1191	160	0.23	-0.22	0.23	0.05
SMSB	15	2.6	5	8	25	239.143	35.063	160	0.35	-0.33	0.75	0.57
SMSB	16	2.6	5	20	13	238.982	35.3564	160	0.71	-1.20	1.36	0.96
SMSB	17	2.6	5	20	1	239.018	35.2524	160	0.11	-0.07	0.13	0.04
SMSB	18	2.6	5	20	12	239.073	35.1696	160	2.37	-1.69	2.50	2.47
SMSB	19	2.6	5	20	7	239.117	35.1191	160	0.48	-0.75	1.06	0.13
SMSB	20	2.6	5	20	25	239.143	35.063	160	0.59	-0.53	0.79	0.47
LSC	1	5	2.5	25	1	238.216	35.418	110	0.10	-0.12	0.15	0.04
LSC	2	5	2.5	25	31	238.244	35.4065	90	0.28	-0.34	0.37	0.11
LSC	3	5	2.5	25	27	238.28	35.4156	80	0.41	-0.34	0.66	0.31
LSC	4	5	2.5	50	1	238.216	35.418	110	0.18	-0.20	0.20	0.05
LSC	5	5	2.5	50	31	238.244	35.4065	90	0.46	-0.76	0.97	0.46
LSC	6	5	2.5	50	27	238.28	35.4156	80	0.63	-0.76	1.08	0.37
LSC	7	5	5	25	1	238.216	35.418	110	0.15	-0.16	0.19	0.02
LSC	8	5	5	25	31	238.244	35.4065	90	0.38	-0.40	0.64	0.12
LSC	9	5	5	25	27	238.28	35.4156	80	0.50	-0.43	0.76	0.48

Source	Case	Length (km)	Width (km)	Height (m)	Slide Velocity (m/s)	Long	Lat	Strike	Max amp	Min Amp	Peak Velocity (m/s)	Peak Velocity at Max Amp (m/s)
LSC	10	5	5	50	1	238.216	35.418	110	0.23	-0.30	0.49	0.08
LSC	11	5	5	50	31	238.244	35.4065	90	0.70	-0.78	1.17	0.75
LSC	12	5	5	50	27	238.28	35.4156	80	0.93	-0.92	1.33	0.68
ESZ	1	7	5	25	103	238.2375	34.73765	145	1.88	-1.34	2.27	2.27
ESZ	2	7	5	50	103	238.2375	34.73765	145	3.14	-1.79	3.75	2.33
ECZ	1	7	5	25	52	238.1275	34.993	200	0.98	-0.78	1.15	0.53
ECZ	2	7	5	100	52	238.1275	34.993	200	3.03	-1.44	2.85	2.85
ECZ	3	10	10	25	52	238.1275	34.993	200	2.06	-1.37	1.56	1.46
ECZ	4	10	10	100	52	238.1275	34.993	200	6.10	-1.89	3.95	3.94
ECZ	5	15	10	25	52	238.1275	34.993	200	2.03	-1.68	1.70	1.63
ECZ	6	15	10	100	52	238.1275	34.993	200	6.88	-2.19	5.54	3.86
SSL	1	5	2.5	25	46	238.6153	34.6321	115	1.21	-0.78	1.35	0.57
SSL	2	5	2.5	25	52	238.6747	34.6072	115	1.17	-0.78	1.06	0.69
SSL	3	5	2.5	25	30	238.734	34.5822	115	0.53	-0.47	0.74	0.48
SSL	4	5	2.5	25	17	238.7633	34.5632	115	0.4	-0.3	0.55	0.17
SSL	5	5	2.5	25	21	238.7927	34.5443	115	0.34	-0.37	0.6	0.05
SSL	6	5	2.5	50	46	238.6153	34.6321	115	2.03	-1.34	1.89	1.89
SSL	7	5	2.5	50	52	238.6747	34.6072	115	2.08	-1.33	1.5	1.5
SSL	8	5	2.5	50	30	238.734	34.5822	115	0.93	-0.89	0.9	0.51
SSL	9	5	2.5	50	17	238.7633	34.5632	115	0.73	-0.77	0.95	0.27
SSL	10	5	2.5	50	21	238.7927	34.5443	115	0.67	-0.77	0.99	0.43
SSL	11	5	5	25	46	238.6153	34.6321	115	2.11	-1.36	2.1	2.1
SSL	12	5	5	25	52	238.6747	34.6072	115	1.93	-1.36	1.43	1.21
SSL	13	5	5	25	30	238.734	34.5822	115	1.06	-0.9	0.96	0.59
SSL	14	5	5	25	17	238.7633	34.5632	115	0.69	-0.74	1.02	0.09
SSL	15	5	5	25	21	238.7927	34.5443	115	0.59	-0.76	0.85	0.33
SSL	16	5	5	50	46	238.6153	34.6321	115	3.42	-1.65	2.86	1.94
SSL	17	5	5	50	52	238.6747	34.6072	115	3.18	-1.65	2.51	2.19
SSL	18	5	5	50	30	238.734	34.5822	115	1.42	-1.47	1.63	1.1
SSL	19	5	5	50	17	238.7633	34.5632	115	1.07	-1.08	1.24	1.17
SSL	20	5	5	50	21	238.7927	34.5443	115	1.15	-1.34	1.53	1.17
SSB	1	4	2	50	40	238.1212	36.2389	105	1.08	-0.88	1.75	1.60
SSB	2	4	2	50	52	238.2298	36.2069	105	2.45	-1.26	2.48	2.09

Source	Case	Length (km)	Width (km)	Height (m)	Slide Velocity (m/s)	Long	Lat	Strike	Max amp	Min Amp	Peak Velocity (m/s)	Peak Velocity at Max Amp (m/s)
SSB	3	4	2	50	30	238.0853	36.1407	105	0.67	-0.76	1.00	0.09
SSB	4	4	2	50	17	238.1942	36.1099	105	0.41	-0.36	0.54	0.16
SSB	5	4	2	50	21	238.1515	36.1574	105	0.56	-0.75	0.73	0.28
SSB	6	4	2	100	40	238.1212	36.2389	105	2.07	-1.80	2.19	1.49
SSB	7	4	2	100	52	238.2298	36.2069	105	3.66	-1.69	3.97	2.54
SSB	8	4	2	100	30	238.0853	36.1407	105	1.58	-1.30	1.53	0.43
SSB	9	4	2	100	17	238.1942	36.1099	105	0.66	-0.77	1.03	0.11
SSB	10	4	2	100	21	238.1515	36.1574	105	1.00	-0.80	1.15	0.32
SSB	11	6	3	50	40	238.1212	36.2389	105	1.70	-1.59	2.24	2.07
SSB	12	6	3	50	52	238.2298	36.2069	105	2.72	-1.84	3.10	2.88
SSB	13	6	3	50	30	238.0853	36.1407	105	0.76	-1.17	1.14	0.62
SSB	14	6	3	50	17	238.1942	36.1099	105	0.42	-0.76	0.74	0.09
SSB	15	6	3	50	21	238.1515	36.1574	105	0.75	-0.75	0.97	0.24
SSB	16	6	3	100	40	238.1212	36.2389	105	2.90	-2.37	4.61	2.93
SSB	17	6	3	100	52	238.2298	36.2069	105	4.40	-2.71	4.55	3.27
SSB	18	6	3	100	30	238.0853	36.1407	105	1.44	-1.86	1.93	1.07
SSB	19	6	3	100	17	238.1942	36.1099	105	0.81	-1.14	1.24	0.48
SSB	20	6	3	100	21	238.1515	36.1574	105	1.32	-0.79	1.36	0.60
ENSZ	1	10.5	10	75	72	23A4.489	36.2286	140	3.09	-2.00	3.23	1.46
ENSZ	2	10.5	10	100	72	23A4.489	36.2286	140	3.83	-2.71	3.62	2.47
ENSZ	3	7	5	25	64.9	-122.428	36.150	100	0.88	-1.34	1.38	0.23
ENSZ	4	7	5	100	64.9	-122.428	36.150	100	2.58	-2.43	3.42	2.85
ENZ-S	1	7	5	25	79.3	-122.064	35.451	159	0.49	-0.73	0.71	0.42
ENZ-S	2	7	5	100	79.3	-122.064	35.451	159	1.7	-1.29	2.51	1.48
ENZ-S	3	10.5	10	75	79.3	-122.064	35.451	159	4.01	-1.7	3.04	2.99
ENZ-N	1	7	5	25	93.8	-122.193	35.720	147	0.99	-1.06	1.42	0.62
ENZ-N	2	7	5	100	93.8	-122.193	35.720	147	3.39	-1.2	3.13	2.27
ENZ-N	3	10.5	10	75	93.8	-122.193	35.720	147	3.88	-2.13	4.86	2.68
ACZ	1	3	2	10	12.2	-120.709	34.431	138	0.07	-0.06	0.06	0.01
ACZ	2	4	3	10	30.6	-120.6398	34.468	116	0.24	-0.33	0.51	0.08
ACZ	3	4	3	35	30.6	-120.6398	34.468	116	0.74	-0.84	0.96	0.33
ACZ	4	6	6	10	10.3	-120.82649	34.65086	152	0.17	-0.19	0.17	0.04
ACZ	5	6	6	35	10.3	-120.82649	34.65086	152	0.39	-0.76	1.13	0.04

Source	Case	Length (km)	Width (km)	Height (m)	Slide Velocity (m/s)	Long	Lat	Strike	Max amp	Min Amp	Peak Velocity (m/s)	Peak Velocity at Max Amp (m/s)
ACZ	6	3	2	10	31.1	-120.78019	34.60873	153	0.34	-0.39	0.53	0.17
ACZ	7	3	2	35	31.1	-120.78019	34.60873	153	0.84	-1.29	1.35	0.75
SMSB18 + Hosgri	1								3.2	-2.4	6.4	3.3
SMSB18 + Hosgri	2								3.7	-2.4	3.0	2.4
SMSB18 + Hosgri	3								3.7	-2.4	3.7	1.1
SMSB18 + Hosgri	4								3.9	-2.4	3.5	2.2
SMSB18 + Hosgri	5								3.2	-2.3	3.0	2.1

Table 6-4. Tsunami Modeling Results for Submarine Landslides at the Discharge Structure

Source	Case	Length (km)	Width (km)	Height (m)	Slide Velocity (m/s)	Long	Lat	Strike	Max amp	Min Amp	Peak Velocity (m/s)	Peak Velocity at Max Amp (m/s)
SMSB	1	2.6	2	8	13	238.982	35.3564	160	0.71	-0.73	2.25	1.75
SMSB	2	2.6	2	8	1	239.018	35.2524	160	0.05	-0.05	0.27	0.07
SMSB	3	2.6	2	8	12	239.073	35.1696	160	0.59	-0.74	3.67	0.8
SMSB	4	2.6	2	8	7	239.117	35.1191	160	0.19	-0.2	0.48	0.39
SMSB	5	2.6	2	8	25	239.143	35.063	160	0.24	-0.2	0.57	0.29
SMSB	6	2.6	2	20	13	238.982	35.3564	160	0.59	-0.74	3.78	1.12
SMSB	7	2.6	2	20	1	239.018	35.2524	160	0.11	-0.12	0.37	0.16
SMSB	8	2.6	2	20	12	239.073	35.1696	160	1.2	-0.74	3.48	1.04
SMSB	9	2.6	2	20	7	239.117	35.1191	160	0.5	-0.51	1.36	0.63
SMSB	10	2.6	2	20	25	239.143	35.063	160	0.57	-0.45	1.35	1.1
SMSB	11	2.6	5	8	13	238.982	35.3564	160	0.55	-0.74	3.58	1.54
SMSB	12	2.6	5	8	1	239.018	35.2524	160	0.06	-0.09	0.27	0.19
SMSB	13	2.6	5	8	12	239.073	35.1696	160	1.27	-0.74	3.5	1.76
SMSB	14	2.6	5	8	7	239.117	35.1191	160	0.22	-0.26	0.39	0.07
SMSB	15	2.6	5	8	25	239.143	35.063	160	0.34	-0.34	0.51	0.16
SMSB	16	2.6	5	20	13	238.982	35.3564	160	0.8	-0.74	3.99	1.39
SMSB	17	2.6	5	20	1	239.018	35.2524	160	0.13	-0.18	0.59	0.11
SMSB	18	2.6	5	20	12	239.073	35.1696	160	3.56	-0.74	3.58	1.79
SMSB	19	2.6	5	20	7	239.117	35.1191	160	0.57	-0.6	1.17	0.47
SMSB	20	2.6	5	20	25	239.143	35.063	160	0.65	-0.63	1.49	0.07
LSC	1	5	2.5	25	1	238.216	35.418	110	0.13	-0.11	0.65	0.33
LSC	2	5	2.5	25	31	238.244	35.4065	90	0.32	-0.62	1.66	0.17
LSC	3	5	2.5	25	27	238.28	35.4156	80	0.46	-0.69	1.58	1.38
LSC	4	5	2.5	50	1	238.216	35.418	110	0.21	-0.23	0.95	0.91
LSC	5	5	2.5	50	31	238.244	35.4065	90	0.59	-0.74	3.46	0.25
LSC	6	5	2.5	50	27	238.28	35.4156	80	0.89	-0.74	3.45	2.36
LSC	7	5	5	25	1	238.216	35.418	110	0.19	-0.2	0.68	0.4
LSC	8	5	5	25	31	238.244	35.4065	90	0.49	-0.66	1.55	0.36
LSC	9	5	5	25	27	238.28	35.4156	80	0.66	-0.74	3.57	0.4

Source	Case	Length (km)	Width (km)	Height (m)	Slide Velocity (m/s)	Long	Lat	Strike	Max amp	Min Amp	Peak Velocity (m/s)	Peak Velocity at Max Amp (m/s)
LSC	10	5	5	50	1	238.216	35.418	110	0.32	-0.37	1.5	0.84
LSC	11	5	5	50	31	238.244	35.4065	90	0.93	-0.74	3.54	1.02
LSC	12	5	5	50	27	238.28	35.4156	80	1.28	-0.74	3.8	0.88
ESZ	1	7	5	25	103	238.2375	34.73765	145	3.39	-0.74	3.47	1.9
ESZ	2	7	5	50	103	238.2375	34.73765	145	5.66	-0.74	6.18	2.72
ECZ	1	7	5	25	52	238.1275	34.993	200	0.99	-0.74	3.62	0.47
ECZ	2	7	5	100	52	238.1275	34.993	200	5.15	-0.74	4.52	1.37
ECZ	3	10	10	25	52	238.1275	34.993	200	2.49	-0.74	4.22	1.1
ECZ	4	10	10	100	52	238.1275	34.993	200	9.48	-0.74	6.11	1.8
ECZ	5	15	10	25	52	238.1275	34.993	200	3.29	-0.74	3.77	1.25
ECZ	6	15	10	100	52	238.1275	34.993	200	8.68	-0.74	6.9	1.91
SSL	1	5	2.5	25	46	238.6153	34.6321	115	1.16	-0.74	4.54	1.96
SSL	2	5	2.5	25	52	238.6747	34.6072	115	1.64	-0.74	3.84	1.43
SSL	3	5	2.5	25	30	238.734	34.5822	115	0.62	-0.74	3.6	0.67
SSL	4	5	2.5	25	17	238.7633	34.5632	115	0.41	-0.47	1.49	0.42
SSL	5	5	2.5	25	21	238.7927	34.5443	115	0.44	-0.59	1.61	0.6
SSL	6	5	2.5	50	46	238.6153	34.6321	115	1.78	-0.74	3.67	1.47
SSL	7	5	2.5	50	52	238.6747	34.6072	115	2.52	-0.74	3.69	1.47
SSL	8	5	2.5	50	30	238.734	34.5822	115	1.02	-0.74	3.47	1.2
SSL	9	5	2.5	50	17	238.7633	34.5632	115	0.6	-0.74	3.42	0.74
SSL	10	5	2.5	50	21	238.7927	34.5443	115	0.81	-0.74	3.76	1.22
SSL	11	5	5	25	46	238.6153	34.6321	115	1.83	-0.74	5.56	1.62
SSL	12	5	5	25	52	238.6747	34.6072	115	2.29	-0.74	4.06	1.34
SSL	13	5	5	25	30	238.734	34.5822	115	1.13	-0.74	3.52	1.37
SSL	14	5	5	25	17	238.7633	34.5632	115	0.61	-0.74	3.43	0.73
SSL	15	5	5	25	21	238.7927	34.5443	115	0.69	-0.74	3.62	0.7
SSL	16	5	5	50	46	238.6153	34.6321	115	3.1	-0.74	3.8	1.16
SSL	17	5	5	50	52	238.6747	34.6072	115	3.98	-0.74	3.96	0.66
SSL	18	5	5	50	30	238.734	34.5822	115	2.48	-0.74	3.73	1.35
SSL	19	5	5	50	17	238.7633	34.5632	115	0.96	-0.74	3.64	0.96
SSL	20	5	5	50	21	238.7927	34.5443	115	1.26	-0.74	3.7	1.27
SSB	1	4	2	50	40	238.1212	36.2389	105	2.01	-0.74	3.69	0.89
SSB	2	4	2	50	52	238.2298	36.2069	105	3.48	-0.74	4.46	1.14

Source	Case	Length (km)	Width (km)	Height (m)	Slide Velocity (m/s)	Long	Lat	Strike	Max amp	Min Amp	Peak Velocity (m/s)	Peak Velocity at Max Amp (m/s)
SSB	3	4	2	50	30	238.0853	36.1407	105	1.04	-0.74	3.56	2.39
SSB	4	4	2	50	17	238.1942	36.1099	105	0.42	-0.56	1.73	0.85
SSB	5	4	2	50	21	238.1515	36.1574	105	0.65	-0.58	2.32	1.38
SSB	6	4	2	100	40	238.1212	36.2389	105	3.85	-0.74	4.1	1.04
SSB	7	4	2	100	52	238.2298	36.2069	105	6.48	-0.74	4.99	1.61
SSB	8	4	2	100	30	238.0853	36.1407	105	1.21	-0.74	3.86	2.15
SSB	9	4	2	100	17	238.1942	36.1099	105	0.79	-0.74	3.48	1.15
SSB	10	4	2	100	21	238.1515	36.1574	105	0.96	-0.74	3.83	1.86
SSB	11	6	3	50	40	238.1212	36.2389	105	2.54	-0.74	4.04	0.83
SSB	12	6	3	50	52	238.2298	36.2069	105	4.4	-0.74	4.46	1.36
SSB	13	6	3	50	30	238.0853	36.1407	105	1.03	-0.74	3.8	0.8
SSB	14	6	3	50	17	238.1942	36.1099	105	0.81	-0.74	3.76	1.5
SSB	15	6	3	50	21	238.1515	36.1574	105	0.87	-0.74	3.65	1.14
SSB	16	6	3	100	40	238.1212	36.2389	105	5.09	-0.74	4.26	1.48
SSB	17	6	3	100	52	238.2298	36.2069	105	A4.22	-0.74	5.58	1.57
SSB	18	6	3	100	30	238.0853	36.1407	105	2.46	-0.74	3.53	0.88
SSB	19	6	3	100	17	238.1942	36.1099	105	1.22	-0.74	3.63	1.47
SSB	20	6	3	100	21	238.1515	36.1574	105	1.54	-0.74	3.74	3.01
ENSZ	1	10.5	10	75	72	23A4.489	36.2286	140	3.51	-0.74	4.08	0.62
ENSZ	2	10.5	10	100	72	23A4.489	36.2286	140	4.52	-0.74	3.98	0.91
ENSZ	3	7	5	25	64.9	-122.428	36.150	100	1.24	-0.74	3.89	0.03
ENSZ	4	7	5	100	64.9	-122.428	36.150	100	4.08	-0.74	4.05	0.97
ENZ-S	1	7	5	25	79.3	-122.064	35.451	159	1.18	-0.74	3.5	1.47
ENZ-S	2	7	5	100	79.3	-122.064	35.451	159	2.78	-0.74	4.84	1.99
ENZ-S	3	10.5	10	75	79.3	-122.064	35.451	159	6.64	-0.74	3.88	1.53
ENZ-N	1	7	5	25	93.8	-122.193	35.720	147	1.02	-0.74	3.64	1.04
ENZ-N	2	7	5	100	93.8	-122.193	35.720	147	5.47	-0.74	4.71	1.62
ENZ-N	3	10.5	10	75	93.8	-122.193	35.720	147	6.71	-0.74	5.03	1.59
ACZ	1	3	2	10	12.2	-120.709	34.431	138	0.09	-0.1	0.43	0.12
ACZ	2	4	3	10	30.6	-120.6398	34.468	116	0.27	-0.3	0.9	0.18
ACZ	3	4	3	35	30.6	-120.6398	34.468	116	0.92	-0.74	3.63	0.28
ACZ	4	6	6	10	10.3	-120.82649	34.65086	152	0.23	-0.28	0.91	0.24
ACZ	5	6	6	35	10.3	-120.82649	34.65086	152	0.5	-0.74	3.8	0.67

Source	Case	Length (km)	Width (km)	Height (m)	Slide Velocity (m/s)	Long	Lat	Strike	Max amp	Min Amp	Peak Velocity (m/s)	Peak Velocity at Max Amp (m/s)
ACZ	6	3	2	10	31.1	-120.78019	34.60873	153	0.39	-0.67	1.51	0.82
ACZ	7	3	2	35	31.1	-120.78019	34.60873	153	1.27	-0.74	4.51	0.78
SMSB18 + Hosgri	1								6.4	-0.74	4.4	3.3
SMSB18 + Hosgri	2								5.6	-0.74	4.5	3.0
SMSB18 + Hosgri	3								6.1	-0.74	4.1	3.2
SMSB18 + Hosgri	4								5.0	-0.74	4.0	2.3
SMSB18 + Hosgri	5								5.5	-0.74	3.4	2.2

TABLE 6-5 Estimated Coefficients for the Wave Height Model for the DCPP Intake Structure

Source		Aref (km^2)	Href (m)	Vref (m/s)	Coeff	Estimate	Coeff s.e.
SMSB		7.5	12.7	7.7	a1	-1.14	0.08
ESZ		35	37.5	103	a7	0.94	0.26
ECZ		52	50	77.2	a2	1.20	0.16
ENZ-S		79.3	50	60.6	a3	0.25	0.22
ENZ-N		93.8	50	60.6	a4	0.63	0.22
SSB		29.5	70.7	12	a5	-0.19	0.13
ENSZ		68.4	57	60.6	a6	0.65	0.18
SSL		17.5	50	30	a7	0.36	0.09
all		-	-	-	b	0.89	0.07
all		-	-	-	c	0.45	0.10
all		-	-	-	d	0.82	0.09

TABLE 6-6 Estimated Coefficients for the Wave Height Model for the DCPP Discharge Structure

Source		Aref (km^2)	Href (m)	Vref (m/s)	Coeff	Estimate	Coeff s.e.
SMSB		7.5	12.7	7.7	a1	-0.97	0.10
ESZ		35	37.5	103	a7	1.52	0.05
ECZ		52	50	77.2	a2	1.48	0.20
ENZ-S		79.3	50	60.6	a3	0.90	0.26
ENZ-N		93.8	50	60.6	a4	1.02	0.26
SSB		29.5	70.7	12	a5	0.18	0.16
ENSZ		68.4	57	60.6	a6	0.93	0.22
SSL		17.5	50	30	A7	0.44	0.10
all		-	-	-	b	0.85	0.08
all		-	-	-	c	0.47	0.11
all		-	-	-	d	0.81	0.11

TABLE 6-7 Estimated Coefficients for the Minimum Wave Height Model for the DCPP Intake Structure

Source		Aref (km^2)	Href (m)	Vref (m/s)	Coeff	Estimate	Coeff s.e.
SMSB		7.5	12.7	7.7	a1	-1.11	0.09
ESZ		35	37.5	103	a7	0.47	0.29
ECZ		52	50	77.2	a2	0.53	0.18
ENZ-S		79.3	50	60.6	a3	0.06	0.24
ENZ-N		93.8	50	60.6	a4	0.17	0.25
SSB		29.5	70.7	12	a5	-0.22	0.15
ENSZ		68.4	57	60.6	a6	0.60	0.20
SSL		17.5	50	30	a7	0.07	0.09
all		-	-	-	b	0.80	0.07
all		-	-	-	c	0.42	0.11
all		-	-	-	d	0.50	0.10

TABLE 6-8. Estimated Coefficients for the Peak Velocity Model.

Location	Parameter	b1	b2	b3	c	Std Dev (LN units)
Intake	Peak Velocity	0.21	0.92	0	1	0.40
Intake	Peak Velocity at Max Amp	-0.2	0.92	-0.27	1	36
Discharge	Peak Velocity	0.98	0.54	-0.167	2	0.47
Discharge	Peak Velocity at Max Amp	-0.19	0.67	-0.043	8	0.85

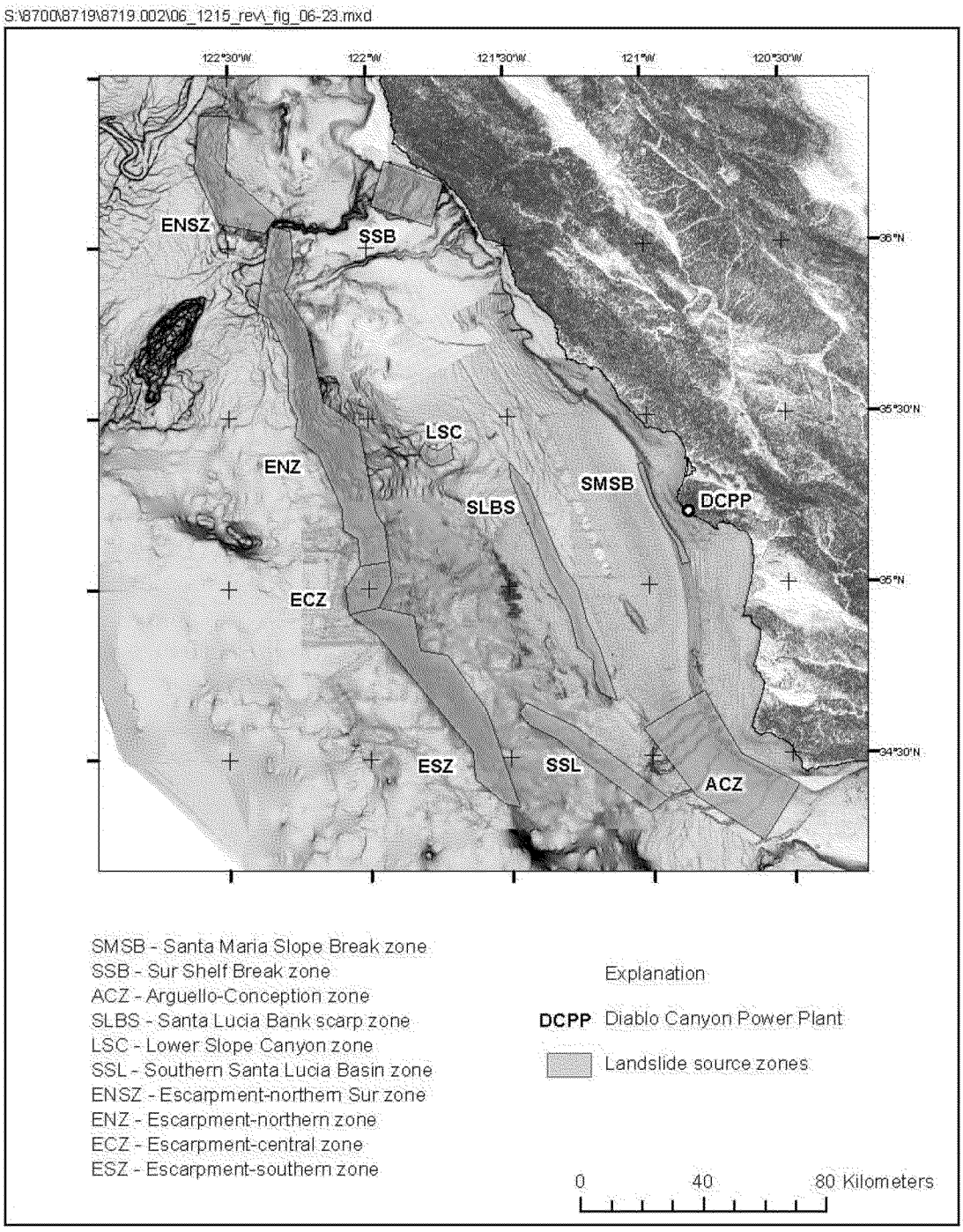

Figure 6-1 Offshore map showing locations of landslide source zones used in tsunamigenic slope failure simulations.

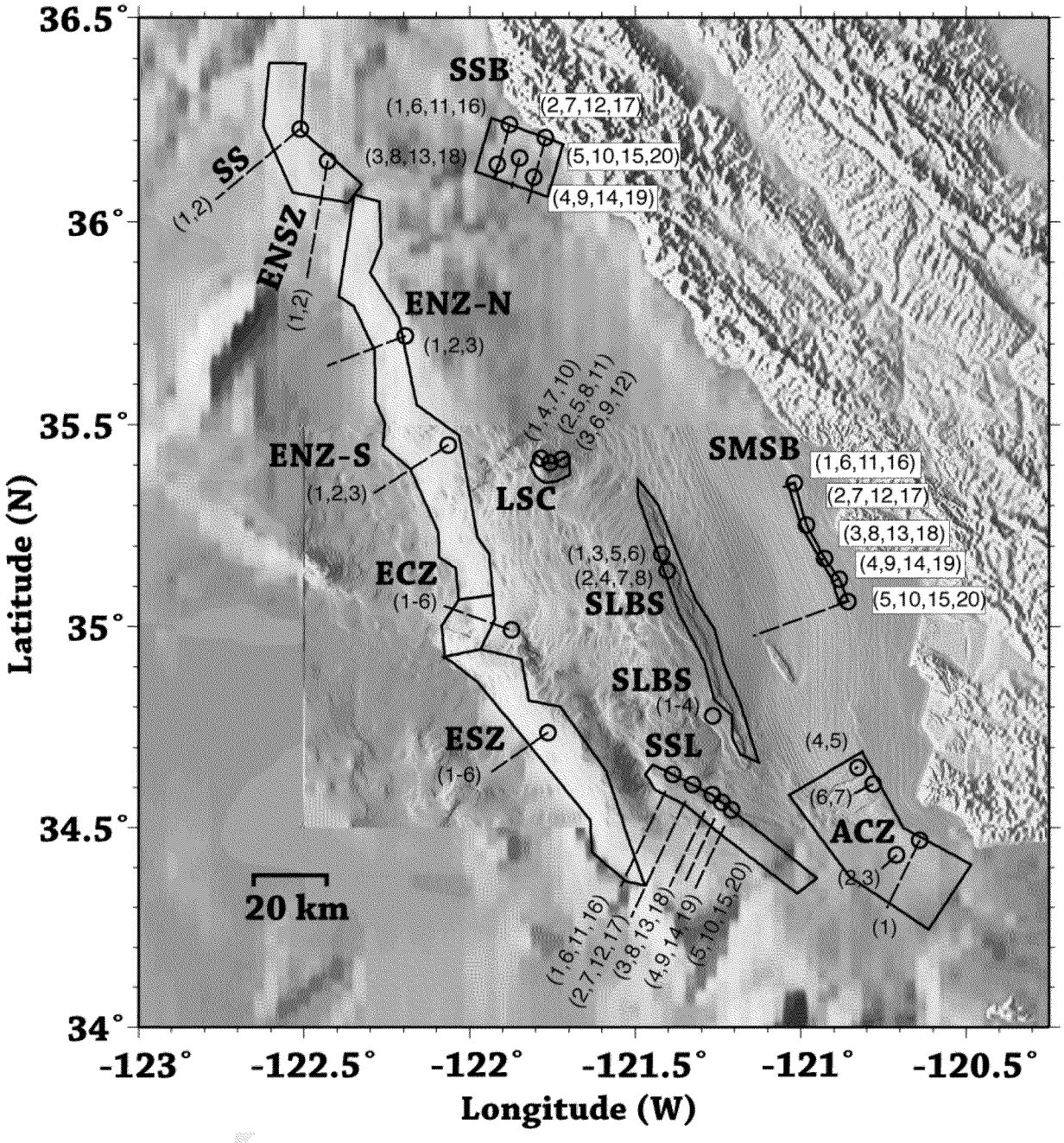

Figure 6-2 Map of the landslide scenarios showing location, slide direction and run out distance. Individual numbers refer to case numbers in Table 6-3.

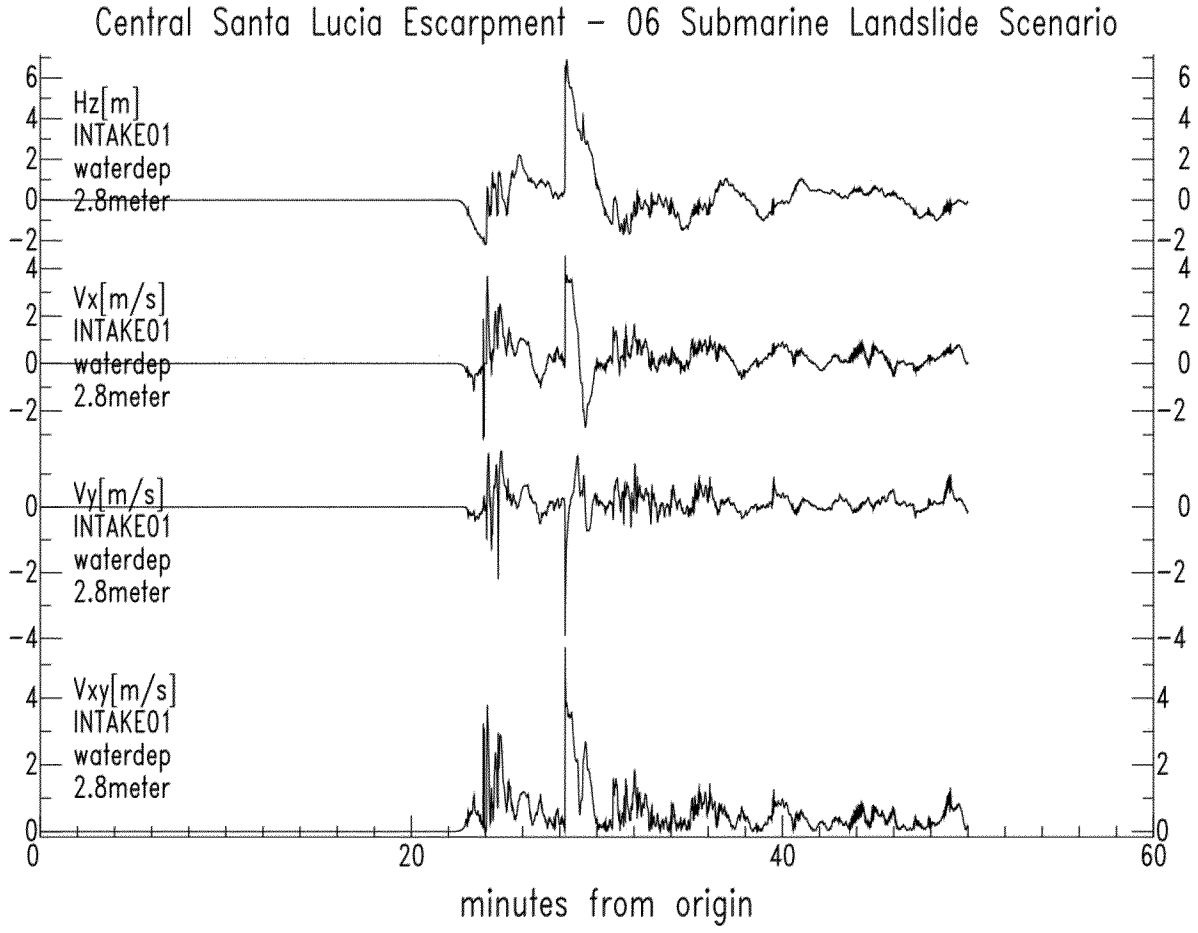

Figure 6-3 Example of Tsunami waveforms at the intake structure for the submarine landslides. This example is for the largest ECZ scenario (ECZ_06 shown in Table 6-3)

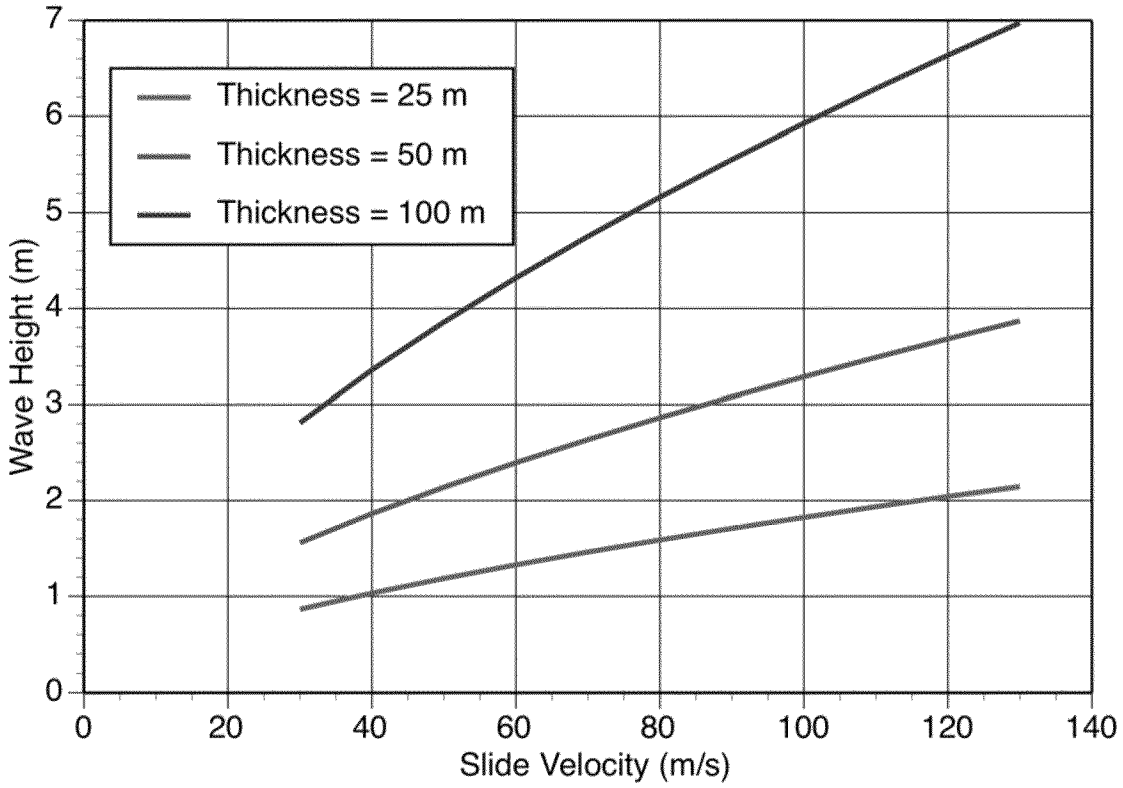

Figure 6-4. Example of the dependence of the median wave height model for landslides on slide velocity and slide thickness. This example is for the ECZ source.

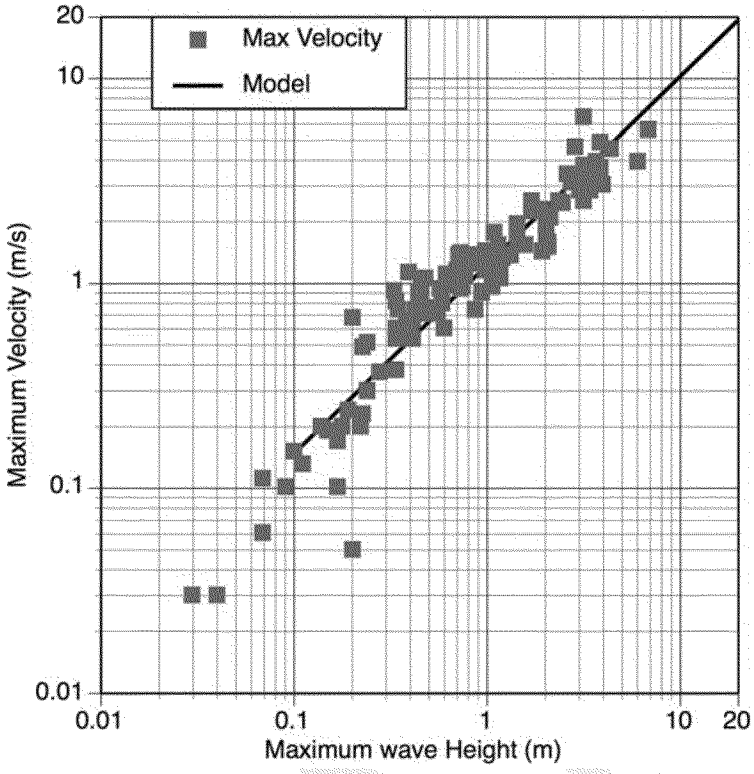

Figure 6-5 Data and model for the peak velocity at the Intake.

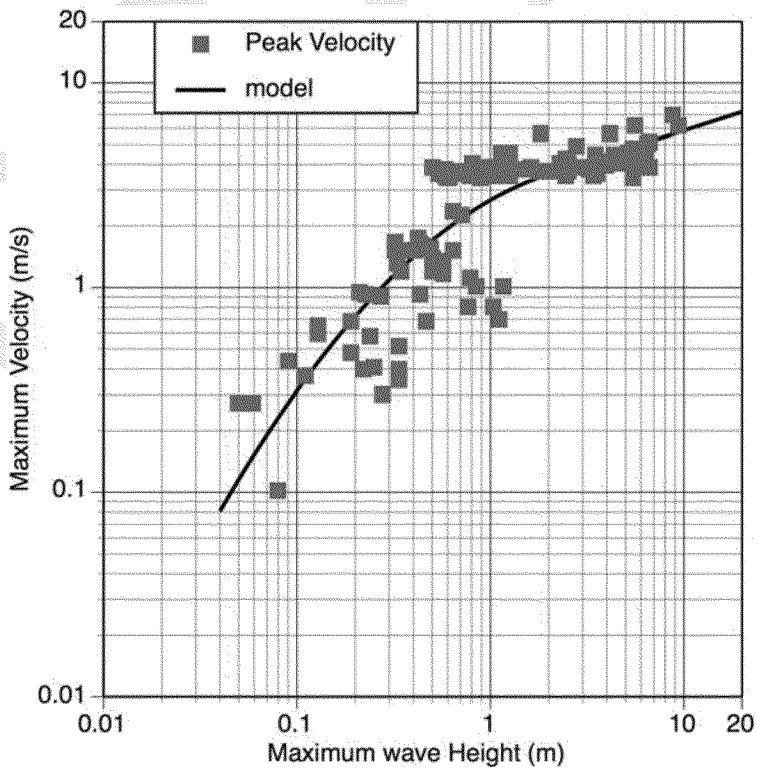

Figure 6-6 Data and model for the peak velocity at the Discharge.

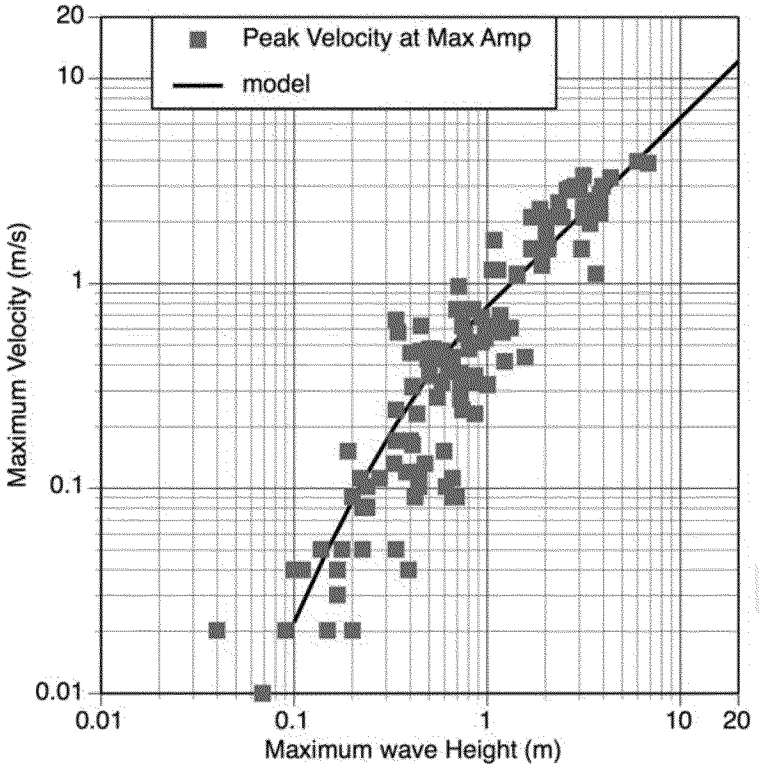

Figure 6-7 Data and model for the peak velocity during the maximum amplitude at the Intake.

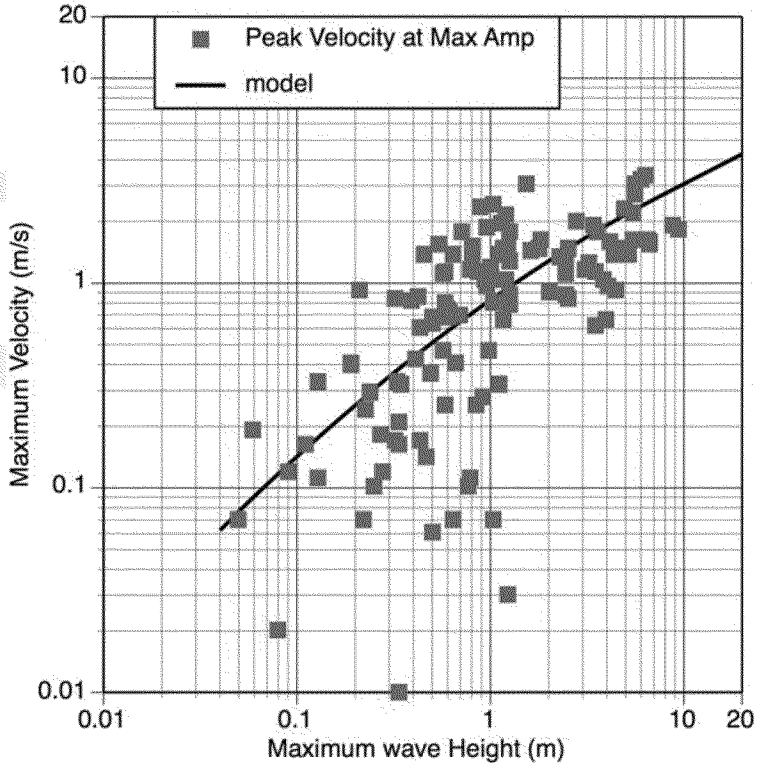

Figure 6-8 Data and model for the peak velocity during the maximum amplitude at the Discharge.

SECTION 7

Distant Tsunamis: Hawaiian Landslides and Volcanic Collapses

7.1 HAWAIIAN LANDSLIDES AND VOLCANIC COLLAPSES

Volcanic eruptions, collapses, and landslides have been sources for locally catastrophic tsunamis. Scenarios describing the consequences of volcanic collapses in the Pacific (Hawaiian Islands) and Atlantic Oceans (Canary Islands) (Ward, 2001; Ward and Day, 2001; Pararas-Carayannis, 2002; Tsunami Society, 2003) have drawn attention to this source of tsunamis, but the effects volcanic collapses at large distances is not well established.

Giant landslide deposits on the flanks of ocean island volcanoes such as Hawaii provide geologic evidence of these catastrophic events. McMurtry and others (2004) note that the occurrence of these events correlates with high stands of sea level, opposite to those observed for continental margin slides, which seem to occur preferentially at low stands of sea level (Maslin and others, 2004).

The Hawaiian Islands are one of the fastest growing and largest features in the world. Their high relief (up to 8.5 km) and large volume (~80,000 km^3) cause them to be unstable and prone to landsliding. The largest mapped submarine slide deposits have volumes of about 5,000 cubic kilometers, making them some of the largest known slope failures on earth (Decker and Decker, 1998). Figure 7-1 shows the location of the landslide debris fields surrounding the Hawaiian Islands. The southern flanks of both Mauna Loa and Kilauea exhibit seaward gravitational spreading, largely occurring along a basal decollement at the boundary between old sea floor and the volcanic pile (Lipman and others, 2006). The south flank of Kilauea creeps seaward at a rate of more than 6 cm/yr (Miklius and others, 2005).

The Pololu avalanche and Laupahoehoe slump on the northeastern side of the island (Figure 7-1) are some of the oldest landslides on the island of Hawaii, having formed during the end of the shield building phase of Kohala and Mauna Kea volcanoes approximately 128 million years ago (Smith and others, 2002). Their morphology is similar to other, younger, Hawaiian slumps, such as the Hilina slump on the south flank of Kilauea or the South Kona and Alika slide complex southwest of Mauna Loa. The Alika submarine landslides, which are suggested to have deposited debris on the coasts of Lanai and Kohoolawe islands, occurred approximately 110,000 years ago (McMurtry and others, 2004). Movement along the southern flanks of both volcanoes during the past 200 years is associated with the two largest historical earthquakes and tsunamis in the Hawaiian Islands.

Historical tectonic activity on the southeastern and southwestern flanks of the island of Hawaii may indicate where future landslide and tsunami activity may occur. The great M_W 7.9 Kau earthquake in April 1868 caused subsidence along the south flank of Mauna Loa volcano (Wyss, 1988). The maximum wave heights along the Hawaiian coast ranged from 6 to 13.7 meters (Lander and Lockridge, 1989). This event produced small waves along the California coast (10 cm at San Diego and 5 cm at Fort Point in San Francisco). Wyss (1988) suggests the failure mechanism of the 1868 Kau event is similar to that of the 1975 Kalapana event, discussed below.

The November 1975 M_W 7.2 Kalapana earthquake occurred east of the 1868 earthquake and generated the largest local tsunami of the 20th Century in Hawaii (~3 m) (Lander and Lockridge, 1989). This event was recorded in California at Port San Luis (0.4 m), at Fort Point, and at San Diego (0.1 m). A tsunami was generated by failure of Kilauea's southern flank along the Kalapana fault, the Hilina slump, and the basal decollement between the old sea floor and the volcanic flank (Day and others, 2005; Pararas-Carayannis, 2005). The Hilina slump is the offshore continuation of Kilauea's mobile southern flank. Kilauea does not have evidence of large-scale slope failures similar to those seen offshore Mauna Loa. The lack of extensive submarine landslide fields offshore Kilauea, the depositional nature of Kilauea's upper slope, and the young age of the Hilina fault system (<39,000 years) are consistent with the relative youth of this volcano (Lipman and others, 2006). Recurrence times for similar failures along the south flank of Kilauea are estimated to be about 200 years (Pararas-Carayannis, 1976). Day and others (2005) note that the type of deformation seen in the 1975 Kalapana earthquake may, in fact, serve to stabilize Kilauea and make catastrophic failure of the volcano flank less likely.

Moore and others (1994) estimate the average recurrence time for giant submarine landslides along the Hawaiian Island chain to be about 350,000 years (or an annual frequency of 3×10^{-6}), based on mapped surficial deposits. Recent drilling offshore Ko'olau volcano, in the vicinity of the Nuuanu landslide (Figure 7-2), indicates the frequency of submarine landsliding may be much greater. At least four major and three significant landslides have occurred there during the past 700,000 years (Garcia and others, 2006). The effect on the coast of California of a giant flank collapse along the northeastern side of the Hawaiian chain could be very dramatic, as suggested by Satake and others (2002), who computed wave heights of 30 to 70 meters along the California

coast for a simulation of the Nuuanu landslide that occurred approximately 2 million years ago on the northeastern flank of Oahu (Figure 7-2).

7.2 TSUNAMI MODELING OF HAWAIIAN VOLCANIC COLLAPSES

We modeled a large, listric, Kalapana-type event at the location of the Hilina slide off the southeastern flank of the island of Hawaii (Figure 7-2) to evaluate the tsunami effects along the central California coast at the DCPP site. The dimensions of the slide are 70 km by 30 km with a maximum thickness of 2 km tapering off to 0 km over a distance of 3 km at the toe of the slide. The sliding distance is assumed to be 20 m, which is substantially more than that estimated for the slide caused by the Kalapana earthquake (~8 m). Given the limited sliding distance, the slide would not have time to develop any higher velocities, even in freefall. Therefore, the slide velocity was set at a low value of 10 m/sec. The short sliding distance also limits the amount of vertical deformation because the only net deformation occurs at the head and the toe of the slide which are its thinnest parts.

The overall geologic character of northeast-directed volcanic rifting on the island of Hawaii and submarine land-sliding along the southeastern and southwestern flanks of the island favor collapses in the direction of South America. Because the tsunami wave propagation is away from the western United States, the wave heights the DCPP site will be small: the wave height at the discharge and intake are 0.5 m at the discharge structure and 0.25 m at the intake. Given the small amplitude of the tsunami from the Hawaiian collapse, this source is not included in the PTHA.

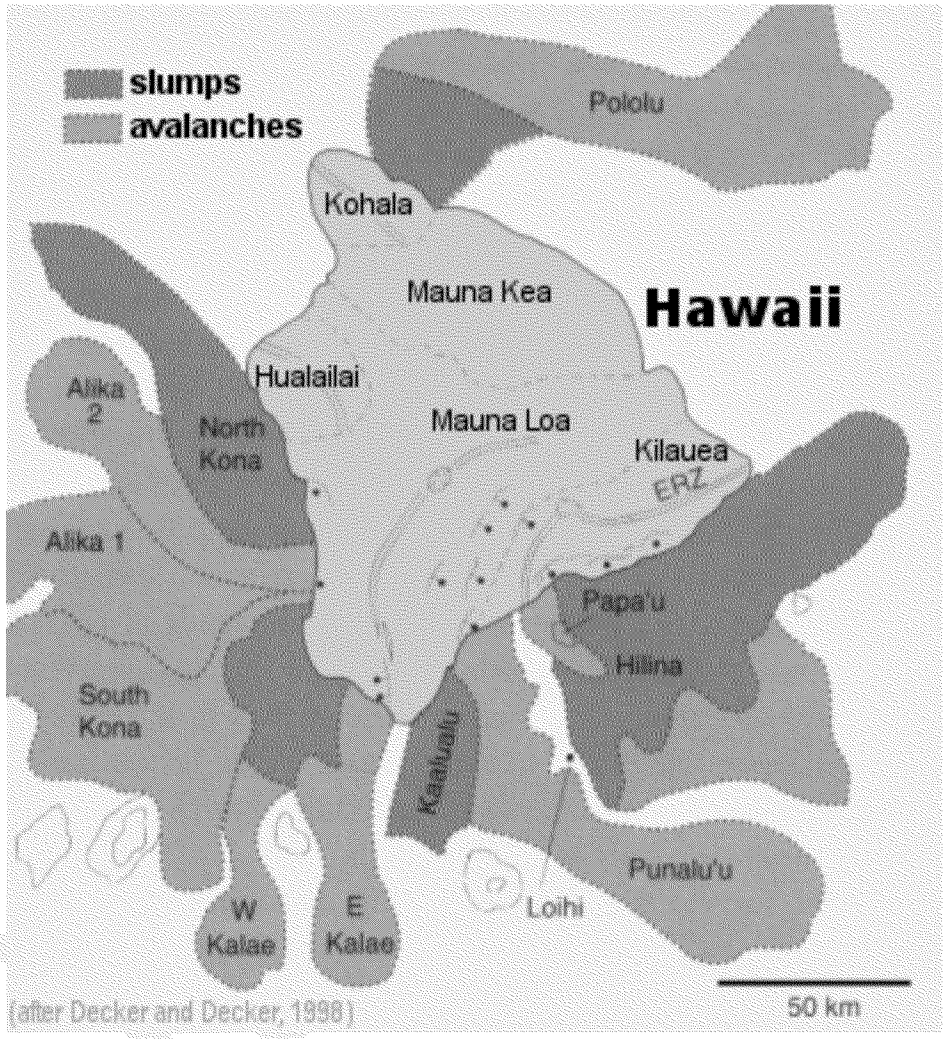

Figure 7-1 Major mapped submarine slides surrounding the Island of Hawaii. The Pololu slide to the northeast is associated with the old, now inactive Kohala/Mauna Kea volcano. Current submarine slide activity is occurring along the southwestern flank of the Mauna Loa volcano and southeastern flank of the Kilauea volcano.

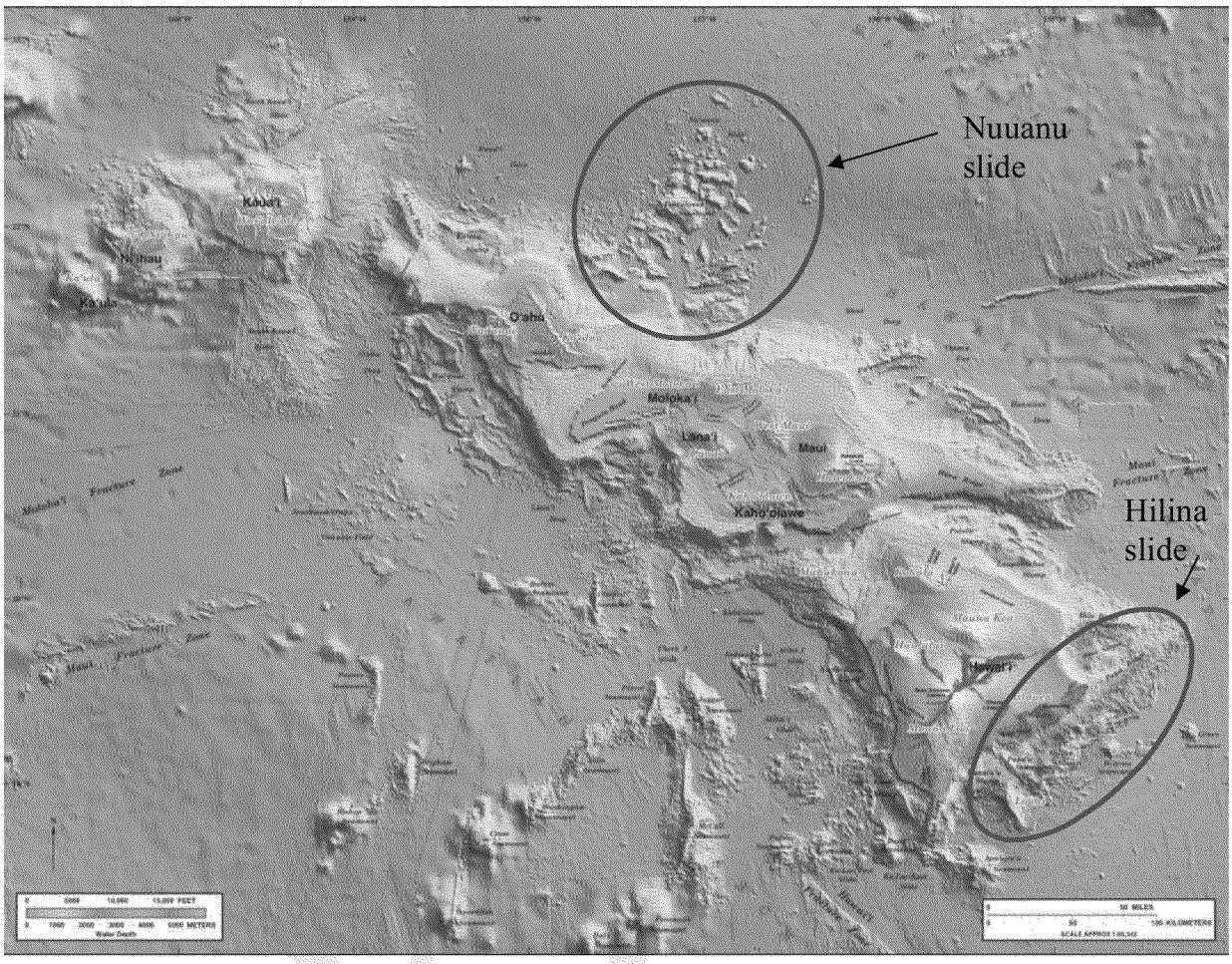

Figure 7-2 Bathymetric map of the Hawaiian Island chain showing the distribution of landslide fields around the islands (from Eakins and others, 2003).

SECTION 8

Storm and Tide Models

8.1 STORM MODEL

8.1.1 STORM DATA AT DCPP

The wave heights from storms have been measured offshore DCPP since 1983. There are a variety of different measurements that have been made since 1983 as shown in Table 8-1. Some of the wave height data are given in terms of the "significant swell height" and some are given in term of the "maximum wave height". Significant swell height is the average of the top third of waves measured in a 10 minute interval, where the height of the wave is measured from the peak to the trough. Maximum wave height is the largest wave, measured from the peak to the trough, for the day.

The reporting of the significant swell height also varies in the data set. As shown in Table 8-1, the values are reported as the largest significant swell height over different time periods. The values are given as the largest value for either 3-hour periods (1994), 6 hours periods (1983-1988), or 24-hour periods (1989-1993,1995-2006). To develop a consistent data set, we first found the daily maximum of the significant swell height for the time periods of 1983-1988 (using the largest value reported each day). These data were then combined with the daily maximum wave heights reported from 1994 to 2006.

For the PTHA, the tsunami wave heights will be combined with the storm wave heights probabilistically. The duration of a tsunami wave is typically 10s of minutes. Ideally, we would have a model of the significant wave heights over 10 minute periods throughout the day, however, the shortest interval for which the significant wave heights are available is 3 hours during the 1994 storm season. With this limitation on available data, we use the largest significant swell height during a three-hour period to combine with the tsunami wave height. This approach has some conservatism in that the significant swell height during the 10-minute tsunami will, in most cases, be less than the largest significant swell height in a 3-hour period.

The three-hour measurements of significant swell height are only available for 1994. The 1994 data is used to develop a model of the distribution of the ratio of the 3-hour significant swell heights to the largest daily significant swell height. To keep the ratio applicable to storm waves, and not to calm seas, the ratio is only computed for daily maximums of 2 m or greater. The resulting distribution is shown in Figure 8-1. We assume that this ratio is applicable to all storms. Applying this distribution of the ratios, we estimate the distribution of significant swell heights in three-hour intervals for the full data set.

Finally, for the PTHA, we want to find the combined heights of the tsunami waves, storm waves, and tides. For this combination, the tsunami waves and storm waves should be the peak wave height relative to the tide level, not the peak to trough height. Therefore, the amplitudes of the significant swell heights are divided by 2.

8.1.2 HISTORICAL STORM MODEL

In addition to the recorded wave heights at DCPP, there is also historical information about storms in the last century. There was a large storm in 1905. While the wave height at DCPP was not measured directly, a hindcast of the wave height was made by Resio (1982) and by Strange and Graham (1982). The estimates of the peak to trough wave heights range from 5.5 to 9.4m. Using one half of the peak to trough height gives wave heights of 2.75m to 4.7m. We use this historical data to help constrain the recurrence model at longer return periods. We used three different estimates of the 1905 storm: best estimate (3.7m), lower estimate (2.7m), and higher estimate (4.7m).

8.1.3 STORM WAVE HEIGHT MODEL

The data set of the largest storm wave over 3 hour intervals and measured zero to peak (e.g. peak above the tide level) is used to develop a probability model for the storm wave heights in the following section. In the remainder of the report, the term wave height will refer to the zero to peak height, not the peak to trough height.

The 3-hour wave height distribution is shown by the red curve in Figure 8-2. For wave heights greater than 1 m, the observed recurrence is consistent with a truncated exponential distribution as shown by the black short dashed curve. A limitation of this data set is that is only covers a 19 year time period and we need to extrapolate the model to much lower probability levels. The 1905 storm is used to extend the duration of the data set from 19 years to 102 years. We assume that there were no other storms equal to or larger than the 1905 storm from 1905 to 1983. With this assumption, point estimates of the storm waves hazard are computed and are shown in Figure 8-2.

The probability density function for a truncated exponential distribution is given by:

$$f_{Storm}(W_S) = \begin{cases} b\ln(10)10^{-b(W_S - S_{\min})} & for S_{\min} < W_S \le S_{Max} \\ 0 & for W_S > S_{Max} \end{cases} \quad (8\text{-}1)$$

where S_{max} is the maximum storm wave height and S_{min} is the minimum storm wave height considered.

The cumulative annual rate of storm wave heights exceeding z in 3 hours intervals is given by:

$$N(W_S > z) = N_0 \int_z^{\infty} f_{storm}(w)dw \qquad (8\text{-}2)$$

The coefficients of the model were estimated for each of the three estimates of the 1905 storm and are listed in Table 8-2. For the low and median estimates of the 1905 storm, the S_{max} value could be determined from the data. For the upper estimate of the 1905 storm, the data do not provide a constraint on the maximum storm wave height. For this case, we assumed a value of 6 m for S_{max}.

The three models are compared to the observations in Figure 8-2. The observations (red curve) are consistent with the lower estimate of the 1905 storm. Therefore, we assign the highest weight to the lower estimate and the smallest weight to the upper estimate. The following weights are assigned to the three storm hazard models: 0.6 for the lower estimate, 0.3 for the central estimate, and 0.1 for upper estimate.

8.2 TIDE MODEL

The model for the tide height was developed using the measured tides offshore DCPP from 2004 to 2007. The data set includes the two high tides and two low tides for each day. The average of each high-low tide pair was computed and the high, low, and average tides are combined into a single data set. The tsunami hazard is being computed relative to mean water level. Therefore, the average value of the tides is removed.

For simplicity, we assume that the tide values are equally likely and represent the tide height for 3-hour periods. Because the high and low tides do not last for the full 3 hour period, this assumption leads to slightly broader distribution of tide heights than would be found for the average tide over 3 hour periods. The resulting distribution of the tide heights is plotted in Figure 8-3 and the values of the distribution are listed in Table 8-3.

There is an 18-year cycle to the tides that is not captured by this data set which covers only 4 years. Incorporating the 18-year cycle would increase the variability of the tides

about the mean value, resulting a slightly broader distribution. This would tend to offset the overly broader distribution that resulted from assuming the high and low tide values applied to a 3 hour time period. In this study, we have not corrected the tide distribution for the 18-year cycle.

8.3 COMBINED STORM AND TIDE HAZARD

The hazard from storms and tides are combined into a single hazard curve to simplify the implementation of the PTHA. The hazard is given by:

$$N_{S\&T}(W_{S\&T} > z) = \sum_{j=1}^{N_S} N(W_S > x_j) \sum_{i=1}^{N_T} H(W_{Ti} + x_j - z) P(W_{Ti}) \qquad (8\text{-}3)$$

where N_S is the number of storm wave heights listed in Table 8-4, N_T is the number of tide heights listed in Table 8-5, H(x) is the Heaviside function, W_{Ti} and $P(T_i)$ are the height and probability of the i^{th} tide, respectively, given in Table 8-5.

The resulting hazard from combined storms and tides are listed in Table 8-6 for the three estimates of the 1905 storm.

Table 8-1 Available Storm Datasets for DCPP

Start Date	End Date	Data
1/1/83	12/31/83	Largest Significant Swell Heights (in 6 hour time periods)
1/1/84	12/31/84	Largest Significant Swell Heights (in 6 hour time periods)
1/1/85	12/31/85	Largest Significant Swell Heights (in 6 hour time periods)
1/1/86	12/31/86	Largest Significant Swell Heights (in 6 hour time periods)
1/1/87	12/30/87	Largest Significant Swell Heights (in 6 hour time periods)
1/1/88	12/31/88	Largest Significant Swell Heights (in 6 hour time periods)
1/1/89	12/4/89	Significant Swell Heights Greater than 8.8 ft Limited data – buoy lost during storm
1/14/91	12/30/91	Significant Swell Heights Greater than 8.8 ft
1/26/92	12/12/92	Significant Swell Heights Greater than 8.8 ft
1/14/93	3/4/93	Significant Swell Heights Greater than 8.8 ft
1/1/94	12/31/94	Largest Significant Swell Heights (in 3 hour time periods)
1/1/95	4/30/95	Maximum Daily Significant Swell Height
9/1/95	4/29/96	Maximum Daily Significant Swell Height
9/1/96	4/30/97	Maximum Daily Significant Swell Height
9/1/07	8/31/98	Maximum Daily Significant Swell Height
9/1/98	8/31/99	Maximum Daily Significant Swell Height
9/1/99	8/31/00	Maximum Daily Significant Swell Height
9/1/00	8/31/01	Maximum Daily Significant Swell Height
9/1/01	8/31/02	Maximum Daily Significant Swell Height
9/1/02	8/31/03	Maximum Daily Significant Swell Height and Partial Maximum Daily Wave Height
9/1/03	8/31/04	Maximum Daily Significant Swell Height and Maximum Daily Wave Height
9/1/04	8/31/05	Maximum Daily Significant Swell Height and Maximum Daily Wave Height
9/1/05	8/31/06	Maximum Daily Significant Swell Height and Maximum Daily Wave Height

Table 8-2. **Distribution of the ratio of the 3-hour maximum wave heights to the daily maximum from 1994 for days with daily maximum wave heights greater than 2 m.**

Ratio	Probability
0.34	0.005
0.44	0.015
0.54	0.057
0.64	0.096
0.74	0.200
0.84	0.262
0.94	0.217
1.00	0.148

Table 8-3. **Coefficients for the storm model**

Coefficient	1905 - Lower Estimate	1905 - Best Estimate	1905 - Upper Estimate
N_0	7000	7000	7000
B	-1.3	-1.3	-1.3
S_{max}	3.2	3.7	6
H_{min}	0.1	0.1	0.1

Table 8-4. **Hazard from Storms**

	Annual Rate of Exceedance During 3 Hour Intervals		
Storm Wave Height (m)	1905 - Lower Estimate	1905 - Median Estimate	1905 - Upper Estimate
0.4	3.154E+03	3.153E+03	3.153E+03
0.6	1.733E+03	1.733E+03	1.733E+03
0.8	9.525E+02	9.523E+02	9.523E+02
1.0	5.234E+02	5.233E+02	5.233E+02
1.2	2.876E+02	2.876E+02	2.876E+02
1.4	1.581E+02	1.580E+02	1.580E+02
1.6	8.687E+01	8.685E+01	8.685E+01
1.8	4.774E+01	4.773E+01	4.773E+01
2.0	2.623E+01	2.623E+01	2.623E+01
2.2	1.442E+01	1.441E+01	1.441E+01
2.4	7.922E+00	7.921E+00	7.921E+00
2.6	4.354E+00	4.353E+00	4.353E+00
2.8	2.392E+00	2.392E+00	2.392E+00
3.0	1.315E+00	1.315E+00	1.314E+00
3.2	4.730E-02	7.224E-01	7.224E-01
3.4	0.000E+00	3.970E-01	3.970E-01
3.6	0.000E+00	1.359E-01	2.181E-01
3.8	0.000E+00	0.000E+00	1.199E-01
4.0	0.000E+00	0.000E+00	6.588E-02
4.2	0.000E+00	0.000E+00	3.620E-02
4.4	0.000E+00	0.000E+00	1.990E-02
4.6	0.000E+00	0.000E+00	1.093E-02
4.8	0.000E+00	0.000E+00	6.008E-03
5.0	0.000E+00	0.000E+00	3.302E-03
5.2	0.000E+00	0.000E+00	1.814E-03
5.4	0.000E+00	0.000E+00	9.971E-04
5.6	0.000E+00	0.000E+00	5.480E-04
5.8	0.000E+00	0.000E+00	3.011E-04
6.0	0.000E+00	0.000E+00	1.083E-05
6.2	0.000E+00	0.000E+00	0.000E+00

Table 8-5. **Distribution of Tides Heights Relative to Mean Water Level at DCPP from 2004 to 2007**

Tide (m)	Probability
-1.6	0.000E+0
-1.4	7.130E-3
-1.2	1.943E-2
-1	3.868E-2
-0.8	3.975E-2
-0.6	3.681E-2
-0.4	8.360E-2
-0.2	1.328E-1
0	2.266E-1
0.2	1.667E-1
0.4	1.046E-1
0.6	6.123E-2
0.8	4.688E-2
1	2.638E-2
1.2	9.180E-3
1.4	1.783E-4
1.6	0.000E+0

Table 8-6. **Hazard from storms and tides.**

	Annual Rate of Exceedance During 3 Hour Intervals		
Combined Storm and Tide Wave Height (m)	1905 - Lower Estimate	1905 - Median Estimate	1905 - Upper Estimate
1.0	9.70E+02	9.70E+02	9.70E+02
1.2	6.51E+02	6.50E+02	6.50E+02
1.4	4.08E+02	4.08E+02	4.08E+02
1.6	2.38E+02	2.38E+02	2.38E+02
1.8	1.31E+02	1.31E+02	1.31E+02
2.0	7.19E+01	7.19E+01	7.19E+01
2.2	3.95E+01	3.95E+01	3.95E+01
2.4	2.17E+01	2.17E+01	2.17E+01
2.6	1.19E+01	1.19E+01	1.19E+01
2.8	6.47E+00	6.55E+00	6.56E+00
3.0	3.47E+00	3.59E+00	3.60E+00
3.2	1.75E+00	1.96E+00	1.98E+00
3.4	8.42E-01	1.06E+00	1.09E+00
3.6	3.88E-01	5.55E-01	5.98E-01
3.8	1.69E-01	2.75E-01	3.29E-01
4.0	5.96E-02	1.30E-01	1.81E-01
4.2	1.37E-02	5.85E-02	9.92E-02
4.4	6.69E-04	2.37E-02	5.45E-02
4.6	8.43E-06	7.36E-03	3.00E-02
4.8	0.00E+00	1.32E-03	1.65E-02
5.0	0.00E+00	2.42E-05	9.04E-03
5.2	0.00E+00	0.00E+00	4.96E-03
5.4	0.00E+00	0.00E+00	2.72E-03
5.6	0.00E+00	0.00E+00	1.48E-03
5.8	0.00E+00	0.00E+00	7.94E-04
6.0	0.00E+00	0.00E+00	4.00E-04
6.2	0.00E+00	0.00E+00	1.93E-04
6.4	0.00E+00	0.00E+00	8.88E-05
6.6	0.00E+00	0.00E+00	3.87E-05
6.8	0.00E+00	0.00E+00	1.37E-05
7.0	0.00E+00	0.00E+00	3.15E-06
7.2	0.00E+00	0.00E+00	1.53E-07
7.4	0.00E+00	0.00E+00	1.93E-09
7.6	0.00E+00	0.00E+00	0.00E+00

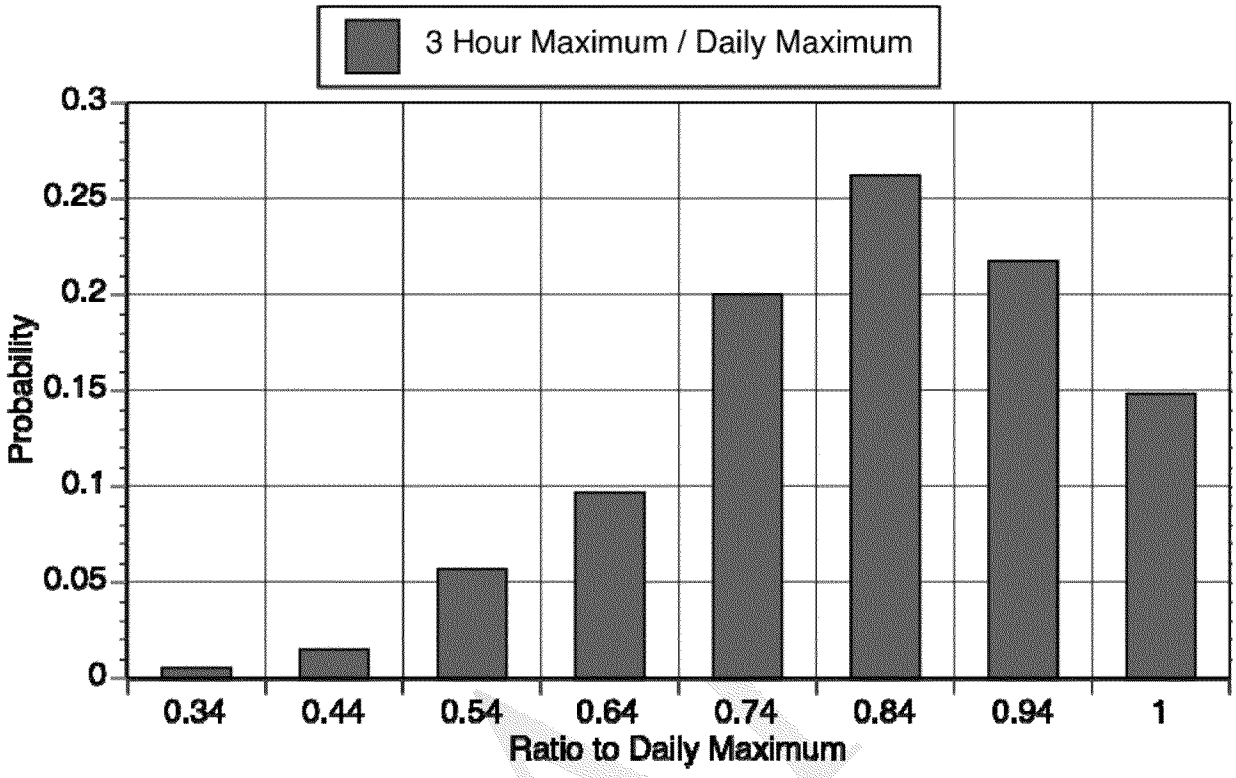

Figure 8-1. Distribution of the ratio of the 3 hour maximum wave heights to the daily maximum.

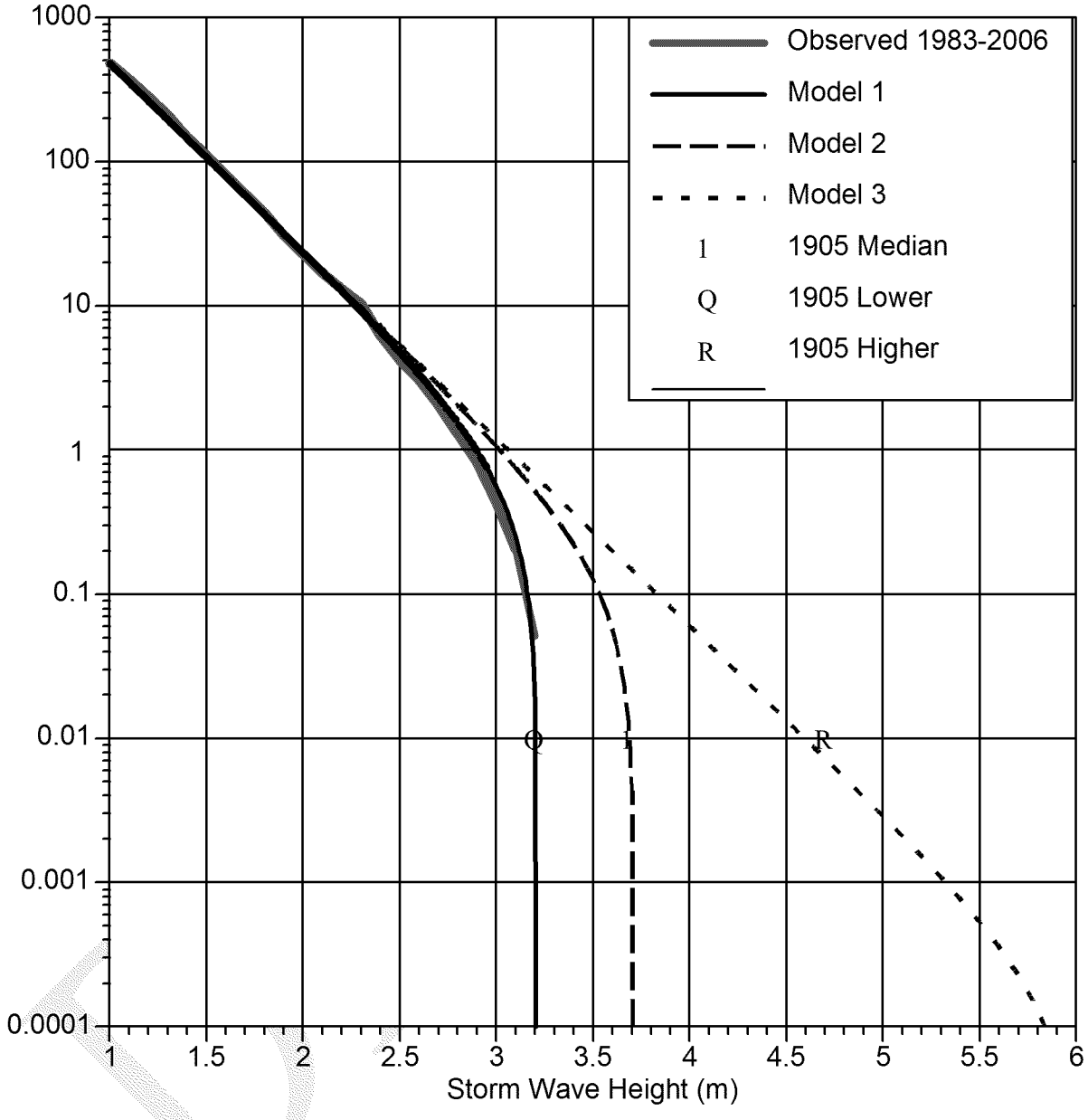

Figure 8-2. Storm hazard models (without tides) for 3 hour intervals.

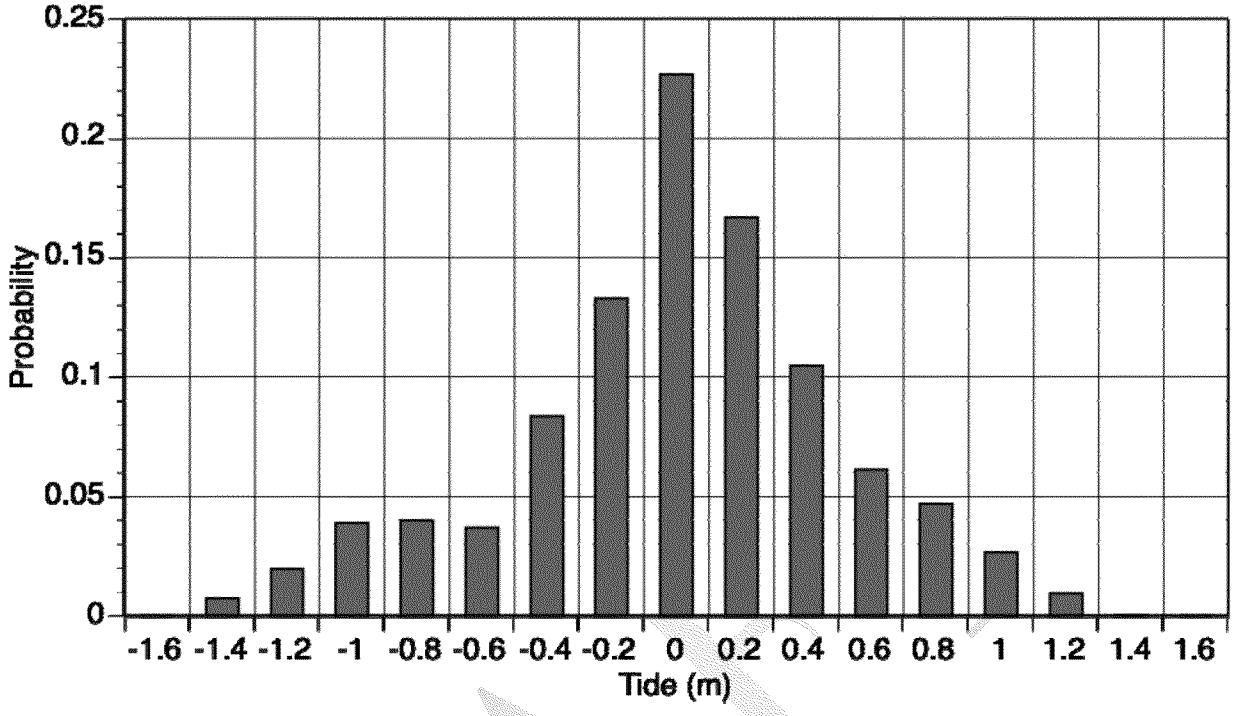

Figure 8-3. Distribution of tide levels (low, median, high) at DCPP from 2004 to 2007.

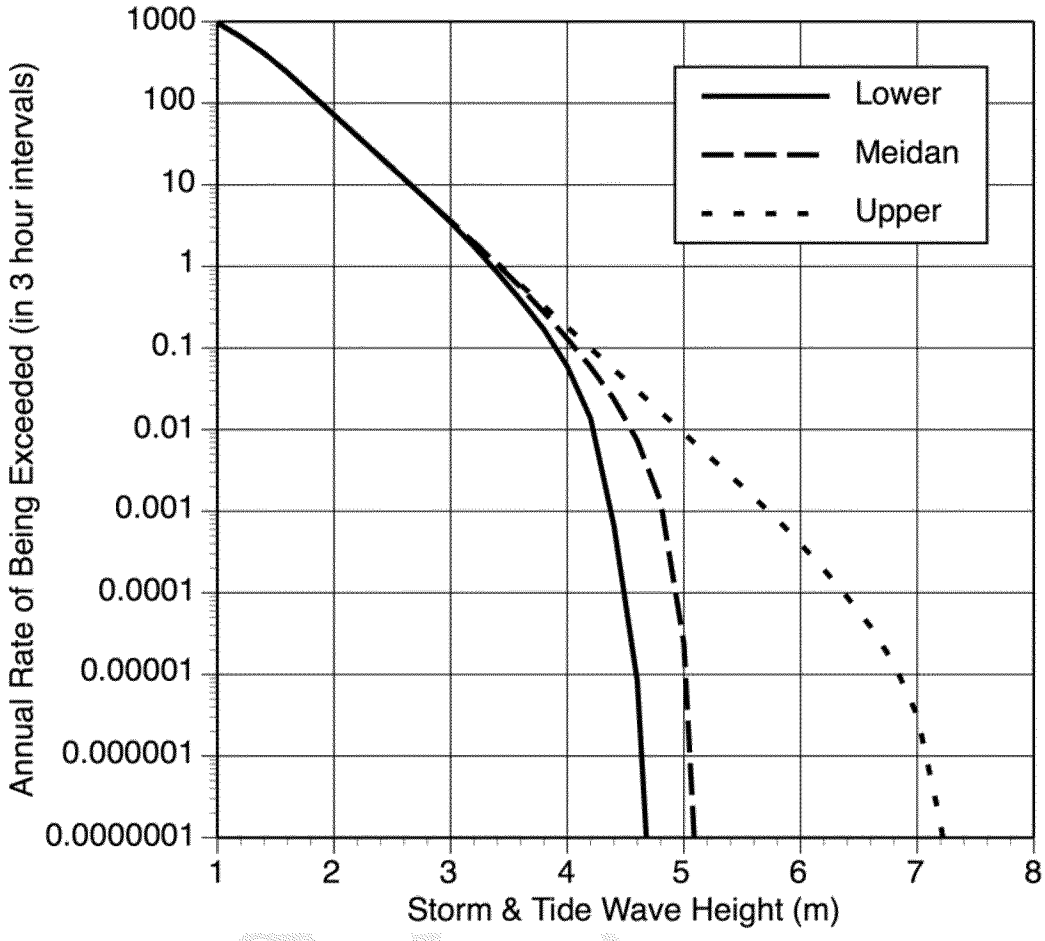

Figure 8-4. Storm and tide hazard models above mean sea level for 3 hour intervals.

SECTION 9

PTHA RESULTS

9.0 INTRODUCTION

Using the source characterization, tsunami modeling results, and the storm and tide models described in Sections 4, 5, 6, and 8, a probabilistic tsunami hazard analysis was conducted for the DCPP site. The results of this trail application of the proposed PTHA methodology is described in this section. First, we show the tsunami hazard by itself, without considering the effects of storms and tides. Next, we show the combined hazard from tsunamis and storms and tides.

9.1 TSUNAMI HAZARD WITHOUT STORMS AND TIDES

The mean tsunami hazard at the DCPP intake structure due to distant earthquake sources, local earthquakes, and submarine landslides are shown separately in Figures 9-1, 9-2, and 9-3, respectively. In each figure, the tsunami hazard curves from the individual sources are also shown. For the distant earthquake-generated tsunamis, the hazard is dominated by the Kamchatka source zone. For the local earthquake-generated tsunamis, the hazard is dominated by the Hosgri and Santa Lucia Banks faults. For the local earthquake-generated tsunamis, the hazard for wave heights greater than 8 m is dominated by the ECZ and ENSZ landslide zones.

The mean tsunami hazard at the DCPP intake structure due to distant earthquake sources, local earthquakes, and submarine landslides are compared in Figure 9-4. The distant earthquake-generated tsunamis dominate the hazard for wave heights up to 3.5m, whereas the landslide-generated tsunamis dominate the hazard for wave heights greater than 4.5 m. The local faulting do not contribute significantly to the hazard at any wave height.

9.1.1 Sensitivity to Aleatory Variability

The sensitivity of the tsunami hazard to the level of the truncation of the log-normal distribution is also shown in Figure 9-5. The hazard was computed with truncation of the aleatory variability at 0, 1, 2, 3, and 4 standard deviations. The differences between truncations at 3 and 4 sigmas are small. The 2 sigma truncation significantly deviates from the 3 and 4 sigma truncation at 2-3 m wave heights. This is due to the truncation from the relatively frequent distant earthquake-generated tsunamis. At wave heights greater than 5 m, the hazard is dominated by the landslides with much higher median wave heights and the effect of the selected truncation level is reduced. This difference will increase at wave heights greater than 10 m.

The basis for truncating the distribution is based on considering that the there is a limit to the volume of water that is displaced. The selected truncation at 2 sigma is based on the recommendation from Thio (personal communication, 2007). This remains an uncertain parameter in the model.

9.2 TSUNAMI HAZARD WITH STORMS AND TIDES

The PTHA is conducted for the maximum wave height, drawdown, and peak velocity. The results are given below.

9.2.1 Maximum Wave Height

The hazard from storms and tides is combined with the tsunami hazard using eq 2-9. The mean hazards for the intake structure and discharge structure are shown in Figures 9-6 and 9-7, respectively. For both the intake and discharge structures, the hazard for wave heights up to 6 m is dominated by storm waves. Tsunamis from distant and local earthquakes are much smaller than the storm waves. For wave heights greater than 7m, the hazard is dominated by the submarine landslides.

The epistemic uncertainty in the tsunami hazard is shown in Figure 9-8 for the intake structure in terms of fractiles on the hazard curve. These fractiles are computed by considering the alternative inputs and weights given in Sections 4-8. For wave heights less than 5 m, the uncertainty is small because the hazard is controlled by the storms and tides and the rates of storms up to 5 m wave heights is well constrained by the observations at DCPP (Section 8). Above 5 m, the uncertainty increases due to the uncertainty in the extrapolation of the storm model (see Figure 8-2) and due to the large uncertainty in the recurrence intervals of the submarine landslides.

Improving the estimation of recurrence intervals for landslides is difficult due to the difficulty in dating past landslides and accounting for the large changes in sea level during the times of past submarine landslides. The rate of landslides for the current sea level may be very different from the rate over the past 10,000 – 100,000 years.

9.2.2 Drawdown

The PTHA was computed for the drawdown following the same methodology as used for the maximum wave height, but without storm waves. The PTHA for the drawdown combines the effects of tsunami waves and tides, but excludes storms because for

drawdown, we are interested in the water receding for a significant time duration (not just for a single wave).

As discussed n Section 4.2.1, the aleatory variability was not calibrated for the drawdown. Therefore, two bounding values were assumed to demonstrate the drawdown hazard: for the first case, the aleatory variability for the drawdown is assumed to be the same as the aleatory variability for the maximum wave height; for the second case, the aleatory variability is assumed to be zero. The zero variability case is intended to show the lower bound for the drawdown hazard and does not represent a best estimate.

The resulting hazard curves are shown in Figures 9-9 and 9-10. In the bathymetry model used in the calculations, the water depth at the intake structure is 4 m. Therefore, the maximum drawdown is 4 m. The results cannot be reliably extrapolated to greater drawdowns. The results show that the drawdown hazard (up to 4 m) is dominated by the relatively frequent distant earthquake-generated tsunamis. Comparing Figures 9-9 and 9-10, there is a large difference due to the assumed aleatory variability.

9.2.3 Peak Velocity

The hazard for the peak velocity is computed using the maximum wave height hazard and the relation between peak velocity and wave height given in Section 6.5. The hazard is computed by integrating over the range of maximum wave heights and over the aleatory variability of the peak velocity for a given maximum wave height:

$$\nu(PeakVel > z) = \int \frac{d\nu_{Tsu}(W)}{dW} P\left(PeakVel > z \mid W\right) dW$$

where $\nu_{Tsu}(W)$ is the hazard for the maximum wave height from tsunamis only (excluding storms and tides) and $P\left(PeakVel > z \mid W\right)$ is the conditional probability of exceeding the peak velocity for a given maximum wave height.

The resulting hazard curves for the intake structure and discharge structure are shown in Figure 9-11. The solid lines shown the hazard for the peak velocity at any time during the tsunami and the dashed lines show the hazard for the peak velocity that occurs at the time of the maximum wave height.

9.3 CONCLUSIONS

A deterministic approach that combines the tsunami generated by a rare local submarine landslide with a large storm wave would lead to an unreasonably rare combination of events. The probabilistic approach developed here can be used to estimate the level of conservatism in current design values and to estimate probabilities of critical flood levels for use in probabilistic risk analyses of nuclear power plants.

The trail application of the PTHA methodology shows that the hazard at DCPP can be captured by selecting the appropriate wave heights from storms and tides for hazard levels greater than 1E-5 and from submarine landslides for hazard levels less than 1E-6. The results show that rare large storm wave should not be added to tsunamis from rare large submarine landslides.

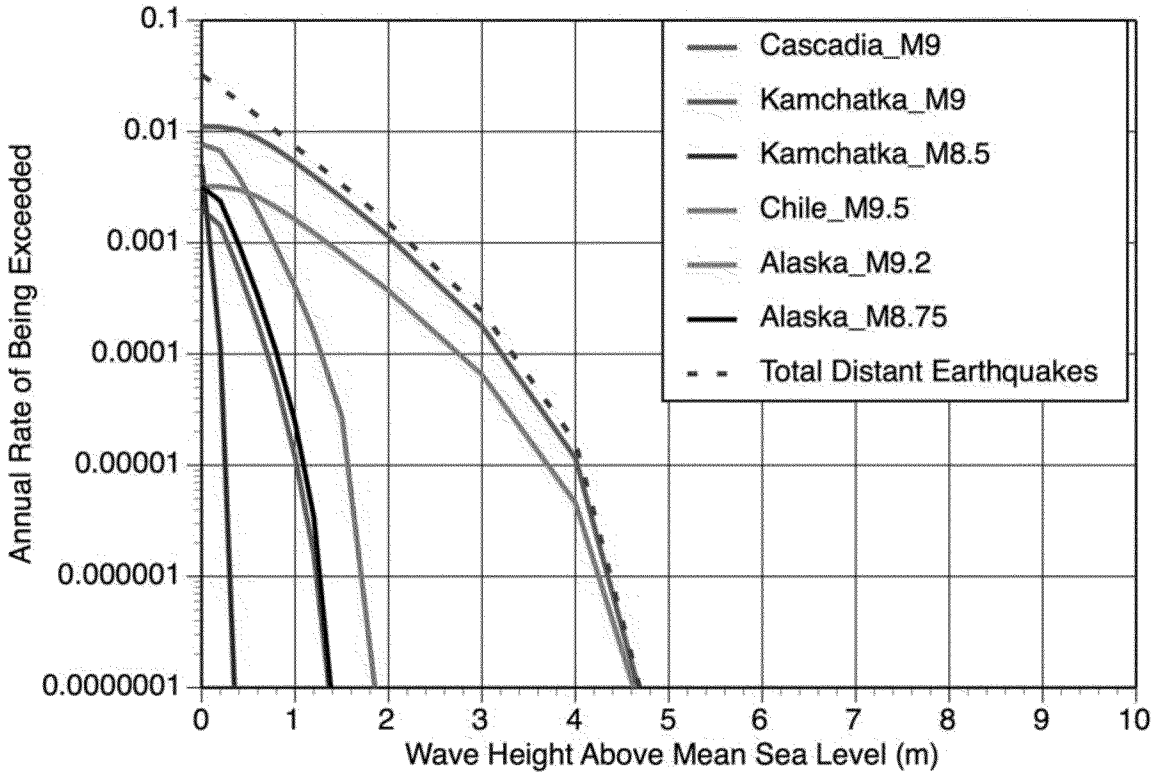

Figure 9-1. Tsunami hazard from distant earthquakes for the DCPP intake.

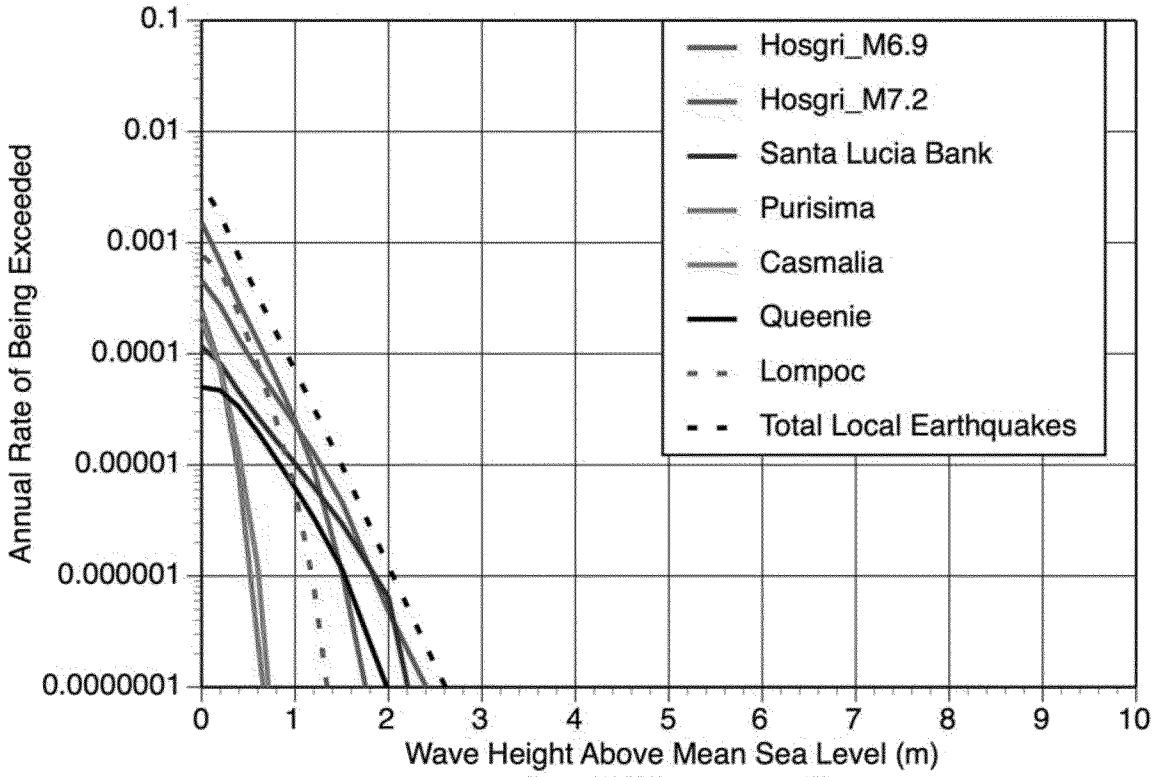

Figure 9-2. Tsunami hazard from local earthquakes for the DCPP intake.

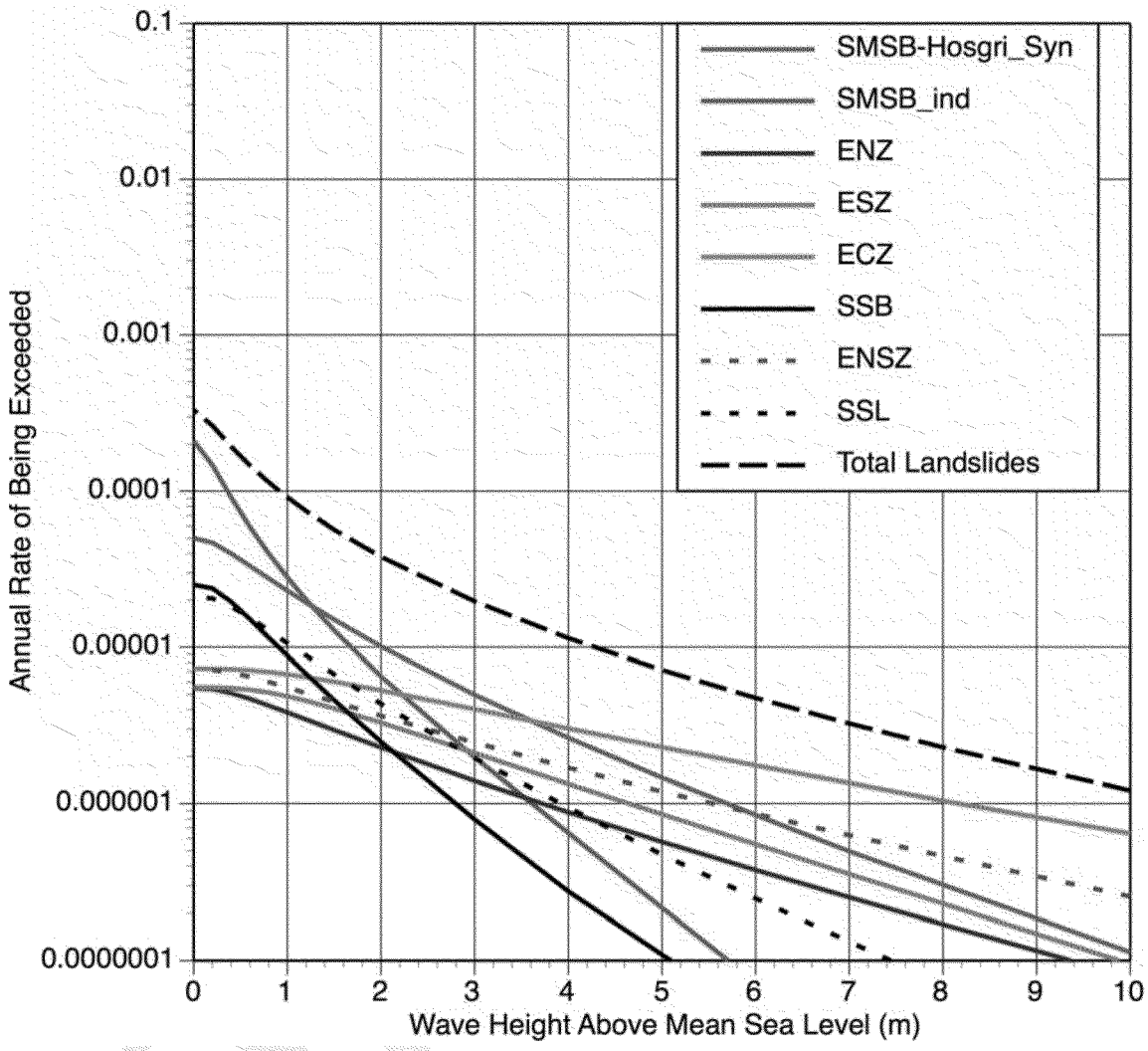

Figure 9-3. Tsunami hazard from submarine landslides earthquakes for the DCPP intake.

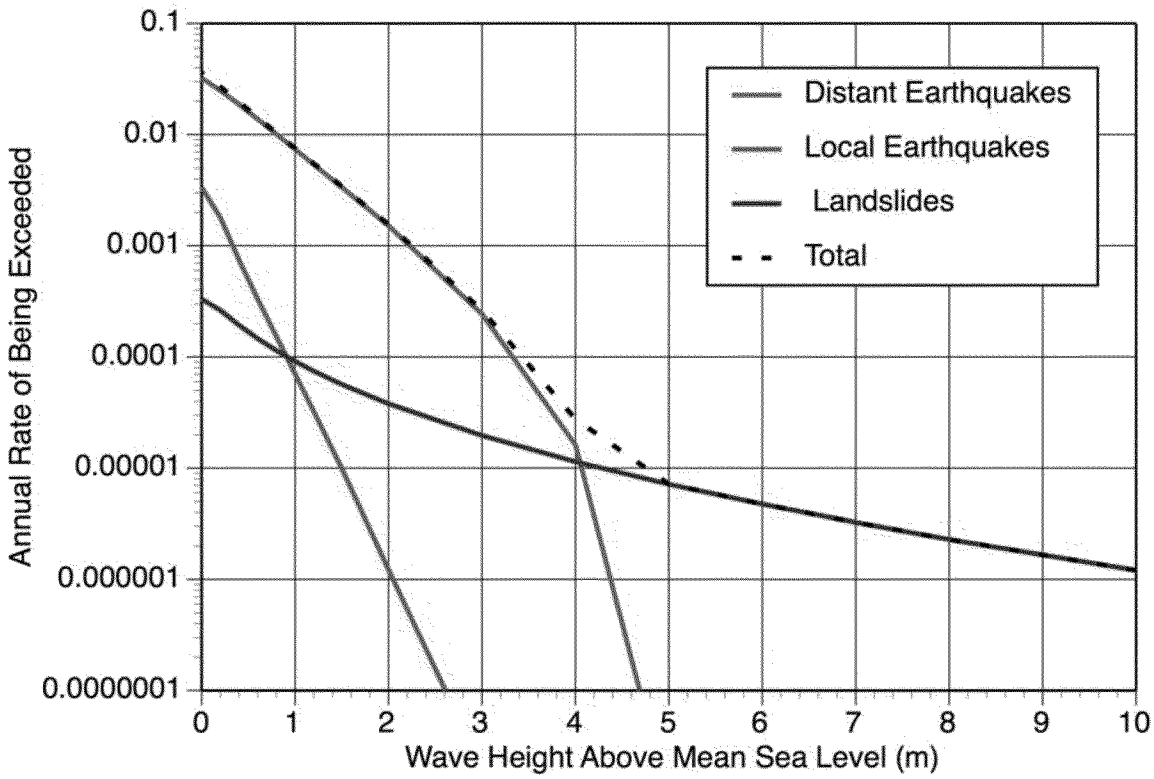

Figure 9-4. Tsunami hazard for the DCPP intake

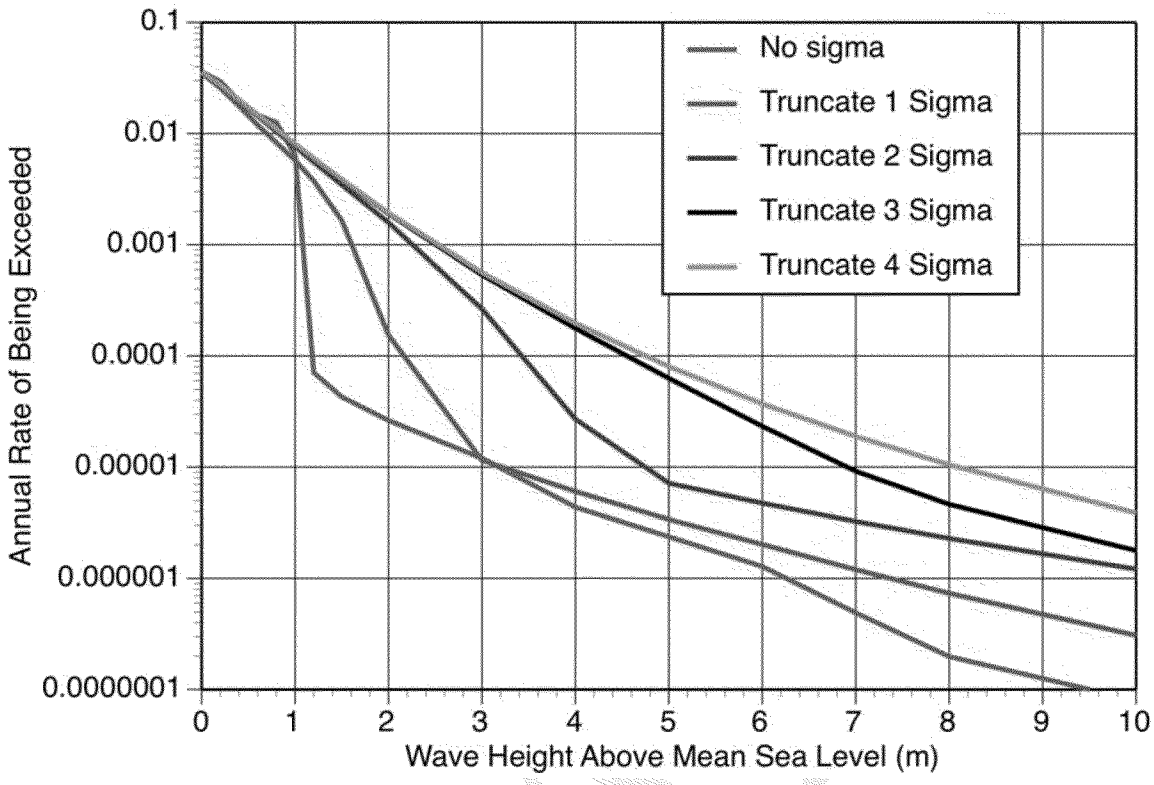

Figure 9-5. Aleatory variability sensitivity of tsunami hazard for the DCPP intake

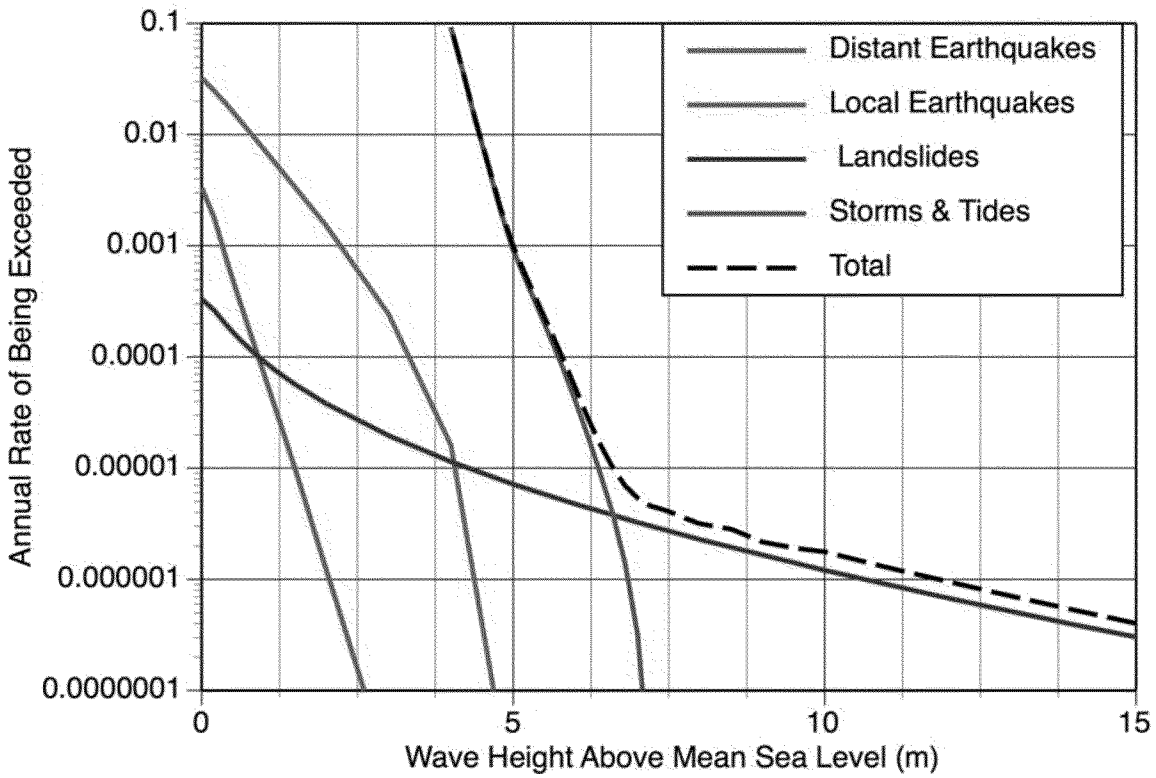

Figure 9-6. Mean hazard from storms, tides, and tsunamis for the DCPP intake structure.

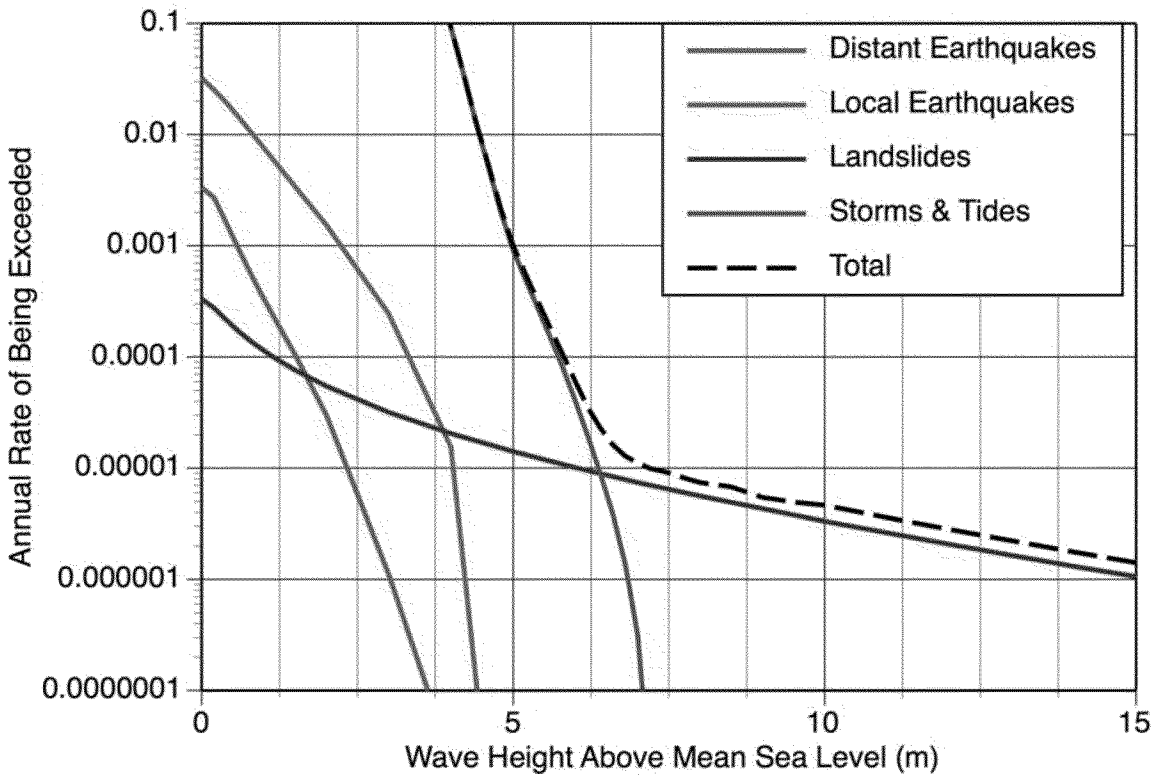

Figure 9-7. Mean hazard from storms, tides, and tsunamis for the DCPP discharge structure.

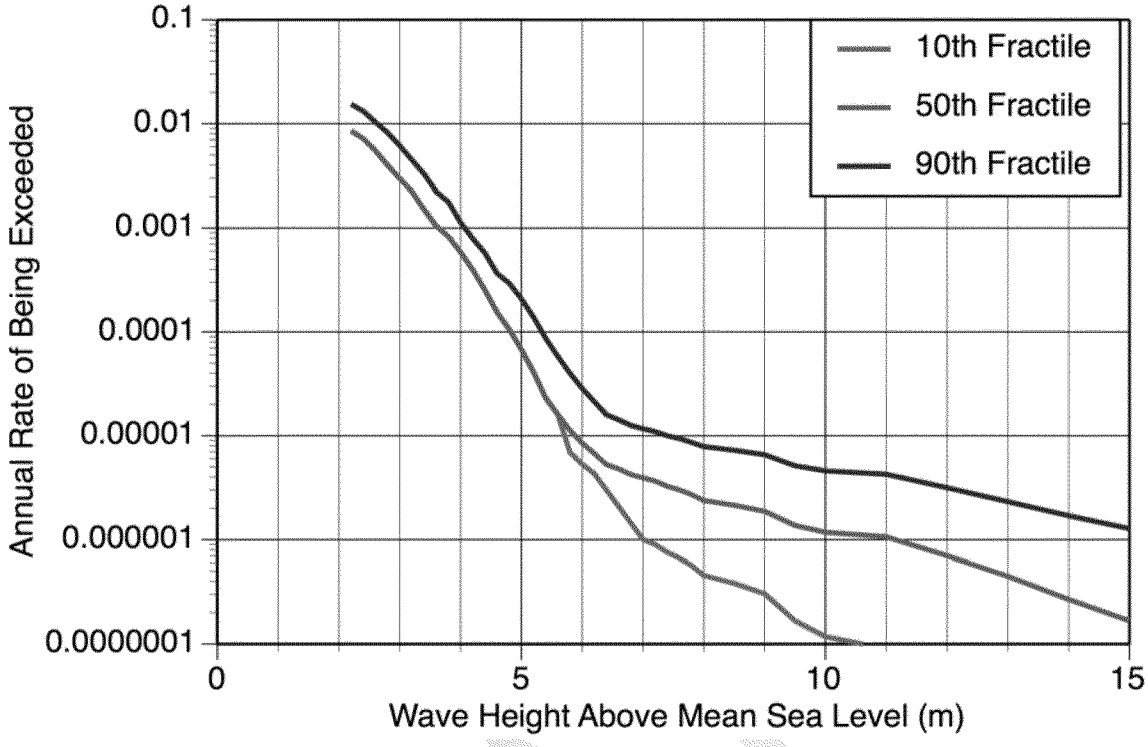

Figure 9-8. Uncertainty fractiles of the hazard for the DCPP intake structure.

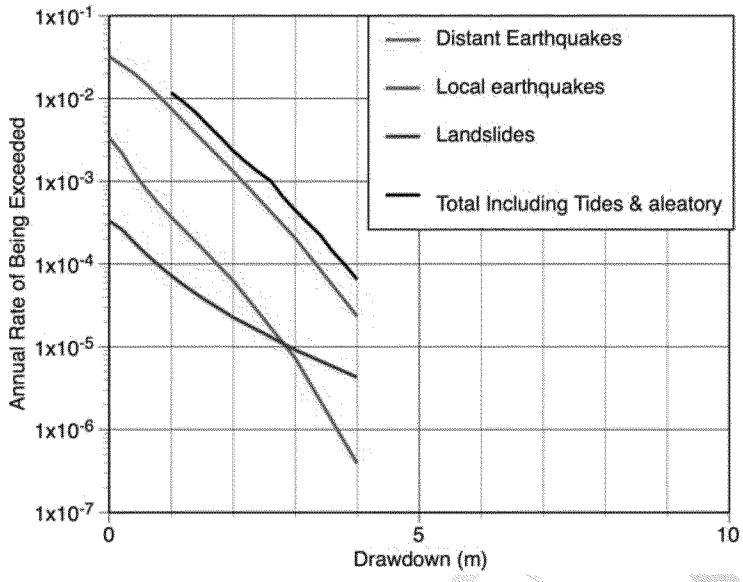

Figure 9-9. Mean drawdown hazard from tides and tsunamis for the DCPP intake structure using the aleatory variability estimated for the maximum wave height. The depth of water for the calculation point used to represent the intake location is 4 m.

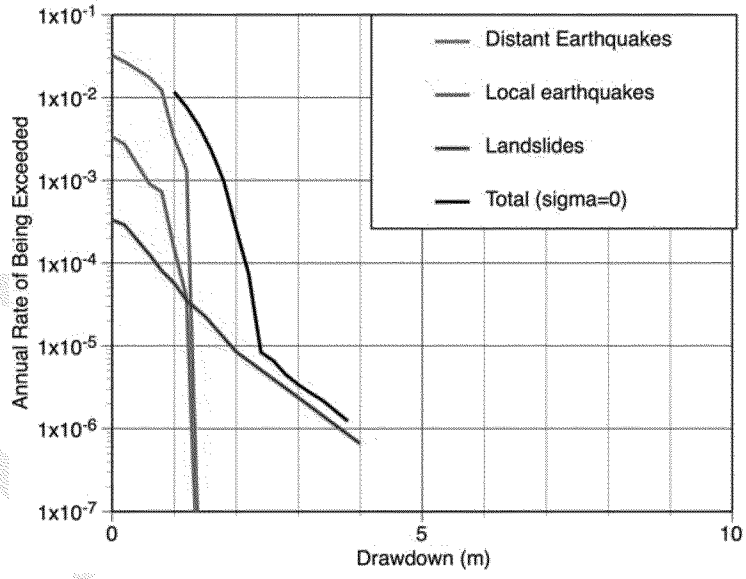

Figure 9-10. Mean drawdown hazard from tides and tsunamis for the DCPP intake structure using the zero aleatory variability. The depth of water for the calculation point used to represent the intake location is 4 m.

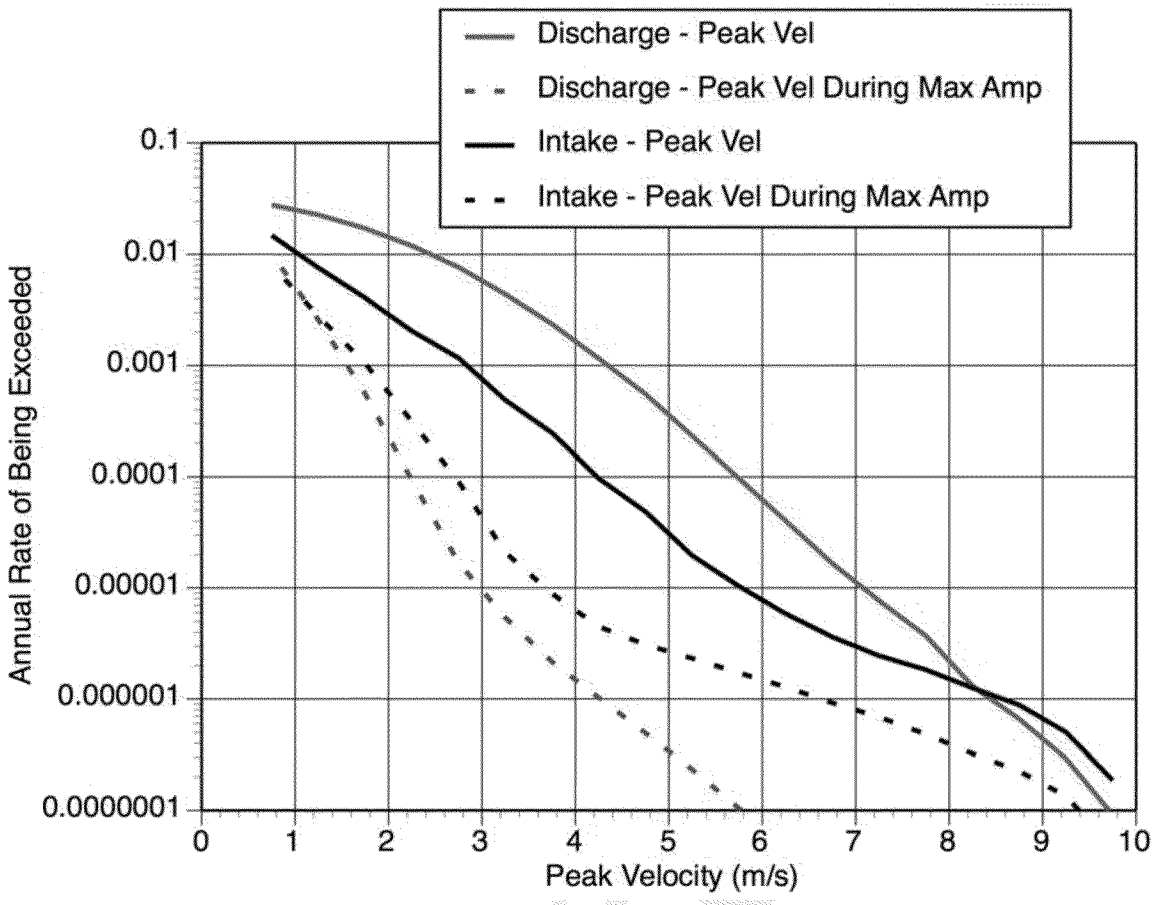

Figure 9-11. Mean peak velocity hazard from tsunamis for the DCPP intake and discharge structures.

10

REFERENCES

Abe, K., 1979, Size of great earthquakes of 1837-1974 inferred from tsunami data: Journal of Geophysical Research, v. 84, no. B4, p. 1561-1568.

Abrahamson, N. A., P. G. Somerville, and C. A. Cornell (1990). Uncertainty in numerical strong ground motion predictions, Proc, Fourth U.S. National Conference on Earthquake Engineering, Palm Springs, CA, 1:407-416.

Barrientos, S.E., and Ward, S.N., 1990, The 1960 Chile earthquake: inversion for slip distribution from surface deformation: Geophysical Journal International, v. 103, p. 589-598.

Bommer, J. and N. A. Abrahamson (2006). Why do modern probabilistic seismic-hazard analyses often lead to increased hazard estimates?, Bull. Seism. Soc. Am., 96:1967-1977.

Byerly, P., 1930, The California earthquakes of November 4, 1927: Bulletin of the Seismological Society of America, v. 20, p. 53-66.

Cisternas, M., Atwater, B.F., Torrejon, F., Sawai, Y., Machuca, G., Lagos, M., Eipert, A., Youlton, C., Salgado, I., Kamataki, T., Shisikura, M., Rajendran., J.K., Rizal, Y., and Husni, M., 2005, Predecessors of the giant 1960 Chile earthquake: Nature, v. 437, p. 404-407.

Clark, D.G., Slemmons, D.B., Caskey, S.J., and DePolo, D.M., 1994, Seismotectonic framework of coastal central California Coast Ranges: Geological Society of America Special Paper 292, p. 9-30.

Clark, D.H., 1990, Quaternary tectonic history and seismic hazard of the Casmalia Range, Santa Barbara County, California: Reno, University of Nevada, M.S. thesis, 130 p.

Clark, D.H., Hall, N.T., Hamilton, D.H., and Heck, R.G., 1991, Structural analysis of late Neogene deformation in the central offshore Santa Maria Basin, California: Journal of Geophysical Research, v. 96, no. B4, p. 6435-6457.

Day, S.J., Watts, P., Grilli, S.T., and Kirby, J.T., 2005, Mechanical models of the 1975 Kalapana, Hawaii earthquake and tsunami, Marine Geology, v. 215, p. 59-92.

Decker, R., and Decker, B., 1998, Volcanoes: Freeman and Co., New York, p. 321.

Dickinson, W.R., Ducea, M., Rosenberg, L.I., Greene, H.G., Graham, S.A., Clark, J.C., Weber, G.E., Kidder, S., Ernst, W.G., and Brabb, E.E., 2005, Net dextral slip, Neogene San Gregorio-Hosgri fault zone, coastal California: Geologic evidence and tectonic implications: Geological Society of America Special Paper 391, p. 43.

Eakins, B.W., Robinson, J.E., Kanamatsu, T., Naka, J., Smith, J.R., Takahashi, E. and Clague, D.A., 2003, Hawaii's Volcanoes Revealed, U.S. Geological Survey Geologic Investigations Series I-2809.

Ellsworth, W., 2003, Magnitude and area data for strike slip earthquakes, in Working Group on California Earthquake Probabilities, Earthquake Probabilities in the San Francisco Bay region: 2002-2031, U.S. Geological Survey Open File Report 03-214, Appendix D,

Fugro West, Inc., Geomatrix Consultants, Inc., and William Lettis & Associates, Inc., 2005, Evaluation of Potential Tsunami Sources in the Diablo Canyon Power Plant Region, Final Report – The Digital Elevation Models: Report to Pacific Gas and Electric Company, November.

Gawthrop, W.H., 1978, Seismicity and tectonics of the central California coastal region: California Division of Mines and Geology Special Report 137, p. 45-56.

Garcia, M. O., Sherman, S. B., Moore, G.F., Goll, R., Popova-Goll, I., Natland, J.H. and Acton, G., 2006, Frequent landslides from Koolau Volcano: Results from ODP Hole 1223A, Journal of Volcanology and Geothermal Research, 151, 251-268. .

Gardner, J.V., Prior, D.B. and Field, M.E., 1999, Humboldt Slide- a retrogressive slope failure, Marine Geology, 154, 323-358.

Gutmacher, C.E., and Normark, W.R., 1993, Sur submarine landslide, a deep-water sediment slope failure, in Schwab, W.C., Lee, H.J., and Twichell, D.C. (eds.), Submarine Landslides: Selected Studies in the U.S. Exclusive Economic Zone: U.S. Bulletin 2002, p. 158-166.

Hampton, M.A., Lee, H.J., and Locat, J., 1996, Submarine landslides: Reviews of Geophysics, v. 34, no. 1, p. 33-59.

Hampton, M.A., Lemke, R.W., and Coulter, H.W., 1993, Submarine landslides that had a significant impact on man and his activities: Seward and Valdez, Alaska, in Schwab, W., Lee, H.J., and Twichell, D.C. (eds.), Submarine Landslides: Selected Studies in the U.S. Economic Zone: U.S. Geological Survey Bulletin 2002, p. 123-134.

Hanks, T. C. and W. H. Bakun (2002). A Bilinear Source-Scaling Model for M-log *A* Observations of Continental Earthquakes, Bull. Seism. Soc. Am., 92:1841-1846.

Hanson, K.L., Lettis, W.R., McLaren, M.K., Savage, W.U., and Hall, N.T., 2005, Style and rate of Quaternary deformation of the Hosgri fault zone, offshore south-central California, in Keller, M.A., Evolution of Sedimentary Basins/Offshore Oil and Gas Investigations--Santa Maria Province: U.S. Geological Bulletin 1995 BB, p. 1- 37. Available at http://pubs.usgs.gov/bul/1995/bb/.

Hapke, C.J., and Green, K.R., 2005a, Decadal-scale analysis of coastal landslides along the Big Sur coast: Rates and processes: U.S. Geological Survey Open-File Report 2005-1434, 20 p.

Hapke, C.J., and Green, K.R., 2005b, Rates of landsliding and cliff retreat along the Big Sur coast, California--Measuring a crucial baseline: U.S. Geological Survey Fact Sheet 2004-3099, p. 1-17, http://pubs.usgs.gov/fs/2004/3099.

Helmberger, D.V., Somerville, P.G., and Garnero, E., 1992, The location and source parameters of the Lompoc, California, earthquake of 4 November 1927: Bulletin of the Seismological Society of America, v. 82, p. 1678-1709.

Johnson, J. M., Satake, K., Holdahl, S. R., and Sauber, J.,1996, The 1964 Prince William Sound earthquake: Joint inversion of tsunami and geodetic data, Journal of Geophysical Research, 101, 523-532.

Johnson, J. M. and Satake, K.,1999, Asperity distribution of the 1952 great Kamchatka earthquake and its relation to future earthquake potential in Kamchatka, Pure and Applied Geophysics, 154, 541-553

Joy, J.W., 1968, Tsunamis and their occurrence along the San Diego County coast: Westinghouse Ocean Research Laboratory, Report 68-567-OCEAN-RL, San Diego, CA, 59 p.

Lander, J.F., and Lockridge, P.A., 1989, United States Tsunamis (including United States Possessions) 1690-1988: National Geophysical Data Center Publication 41-2, Boulder, CO, 265 p.

Lander, J.F., Lockridge, P.A., and Kozuch, M.J., 1993, Tsunamis Affecting the West Coast of the United States, 1806-1992: National Geophysical Data Center, KGRD 29, Boulder, CO, 242 p.

Lee, H.J., Kayen, R.E., Gardner, J.V., and Locat, J., 2003, Characteristics of several tsunamigenic submarine landslides, in Locat, J., and Mienert, J. (eds.), Submarine Mass Movements and Their Consequences: Kluwer Academic Publishers, Netherlands, p. 57-366.

Lee, H.J., Schwab, W.C., and Booth, J.S., 1993, Submarine landslides: An introduction, in Schwab, W.C., Lee, H.J. and Twichell, D.C., (eds.), Submarine landslides: Selected studies in the U.S. Exclusive Economic Zone: U.S. Geological Survey Bulletin 2002, p. 1-13.

Lettis, W.R., and Hanson, K.L., 1991, Crustal strain partitioning--Implications for seismic hazard assessment in Western California: Geology, v. 19, p. 559-562.

Lettis, W.R., Hanson, K.L., Unruh, J.R., McLaren, M., and Savage, W.U., 2004, Quaternary tectonic setting of south-central coastal California, in Keller, M.A., Evolution of Sedimentary Basins/Offshore Oil and Gas Investigations--Santa Maria Province: U.S. Geological Bulletin 1995 AA, 21 p. 1 plate (1:250,000). Available at http://pubs.usgs.gov/bul/1995/aa/.

Lipman, P.W., Sisson, T.W., Coombs, M.L., Calvert, A. and Kimura, J-I., 2006, Piggyback tectonics: Long-term growth of Kilauea on the south flank of Mauna Loa, Journal of Volcanology and Geothermal Research, 151, 73-108.

Marine Advisors, 1966, An evaluation of tsunami potential at the Diablo Canyon site: Report A-253 to Pacific Gas and Electric Company, December.

Maslin, M., Owen, M., Day, S., and Long, D., 2004, Linking continental slope failures and climate change: testing the clathrate gun hypothesis: Geology, v. 32, p. 53-56.

McCulloch, D.S., 1985, Evaluating tsunami potential, in Ziony, J.I. (ed.), Evaluating Earthquake Hazards in the Los Angeles Region – an Earth Science Perspective: U.S. Geological Survey Prof. Paper 1360, p. 374-413.

McCulloch, D.S., 1987, Regional geology and hydrocarbon potential of offshore central California, in Scholl, D.W., Grantz, A., and Vedder, J.G. (eds.), Geology and resource potential of the continental margin of western North America and adjacent ocean basins--Beaufort Sea to Baja California: Houston, Texas, Circum-Pacific Council for Energy and Mineral Resources, Earth Science Series, v. 6, p. 353-401.

McCulloch, D.S., 1989, Geologic map of the south-central California continental margin-Map No. 4A (Geology), Sheet 1 of 4, in Greene, H.G., and Kennedy, M.P. (eds.), California Continental Margin Geologic Map Series South-Central California Continental Margin Area 4 of 7, scale 1:250,000.

McCulloch, D.S., and Greene, H.G., 1990, Geologic map of the central California continental margin-Map No. 5A (Geology), in Greene, H.G., and Kennedy, M.P. (eds.), California Continental Margin Geologic Map Series -Central California Continental Margin - Area 5 of 7, sheet 1 of 4, scale 1:250,000.

McCulloch, D.S., Greene, H.G., Heston, K.S., and Rubin, D.M., 1980, A summary of the geology and geologic hazards in proposed lease sale 53, central California outer continental shelf: U.S. Geological Survey Open-File Report 80-1095, 76 p., 12 plates.

McIntosh, K.D., Reed, D.L., Silver, E.A., and Meltzer, A.S., 1991, Deep structure and structural inversion along the central California continental margin from EDGE seismic profile RU-3: Journal of Geophysical Research, v. 96, no. B4, p. 6459-6473.

McMurtry, G.M., Fryer, G.J., Tappin, D.R., Wilkinson, I.P., Williams, M., Fietzke, J., Garbe-Schoenberg, D., and Watts, P., 2004b, Megatsunami deposits on Kohola volcano, Hawaii, from flank collapse of Mauna Loa: Geology, v. 32, p. 741-744.

Meltzer, A.S., and Levander, A.R., 1991, Deep crustal reflection profiling offshore southern Central California: Journal of Geophysical Research, v. 96, no. B4, p. 6475-6491.

Miklius, A., Cervelli, P., Sako, M., Lisowski, M., Owen, S., Segal, P., Foster, J., Kamibayashi, K., and Brooks, B., 2006, Global positioning system measurements on the island of Hawaii: 1997 through 2004, U.S. Geological Survey Open File Report 2005-1425, 46 pp.

Miller, K.C., Howie, J.M., and Ruppert, S.D., 1992, Shortening within underplated oceanic crust beneath the central California margin: Journal of Geophysical Research, v. 97, no. B13, p. 19,961-19,980.

Monterey Bay Aquarium Research Institute (MBARI), 2000, Monterey Bay multibeam survey: Digital Data Series No. 3.

Moore, J.G., Normark, W.R., and Holcomb, R.T., 1994, Giant Hawaiian landslides: Annual Review, Earth and Planetary Science, v. 22, p. 119-144.

Namson, J.S., and Davis, T., 1990, Late Cenozoic fold and thrust belt of the southern Coast Ranges and Santa Maria Basin, California: American Association of Petroleum Geologists Bulletin, v. 74, p. 467-492.

National Science and Technology Council, 2005, Tsunami risk reduction for the United States: A framework for action, Washington D.C., 27 p.

Nishenko, S. P., 1985, Seismic potential for large and great interpolate earthquakes along the Chilean and southern Peruvian margins of South America: a quantitative reappraisal, Jour. Geophys. Res., **90**, 3589-3615.

Nishenko, S., Plafker, G., and Page, W., 2004, Tsunami hazard based on empirical data from tsunamigenic earthquakes: Eos Transactions, AGU, v. 85 no. 47, Fall Meeting Supplement.

Pacific Gas and Electric Company, 1988, Final Report of the Diablo Canyon Long Term Seismic Program: Pacific Gas and Electric Company, Docket nos. 50-275 and 50-323.

Pacific Gas and Electric Company, 1989, Question Q43l-1: Attachment Q43l-1, Analysis of sea floor geomorphic features associated with the Hosgri fault zone between Point Estero and San Luis Obispo Bay, Diablo Canyon Long Term Seismic Program: U.S. Nuclear Regulatory Commission docket nos. 50-275 and 50-323.

Pacific Gas and Electric Company, 1990, Attachment GSG Q1-A, Montage of geophysical data and interpretations, Hosgri fault zone, eastern offshore Santa Maria basin, database interpretational procedures, and key observations, Response to Questions GSG Q1, Diablo Canyon Long Term Seismic Program: U.S. Nuclear Regulatory Commission docket nos. 50-275 and 50-323.

Pacific Gas and Electric Company, 2010, Characterization of submarine landslides offshore DCPP.

Pararas-Carayannis, G., 1976, The earthquake and tsunami of 29 November 1975 in the Hawaiian Islands, http://www.drgeorgepc.com/Tsunami1975Hawaii.html

Pararas-Carayannis, G., 2002, Evaluation of the threat of mega tsunami generation from postulated massive slope failures of island stratovolcanoes on La Palma, Canary Islands, and the island of Hawaii: Science of Tsunami Hazards, v. 20, p. 251-277.

Pararas-Carayannis, G., 2005, Instability of Kilauea volcano's southern flank- evaluation of mass edifice failures, flank collapses and potential tsunami generation, at http://www.drgeorgepc.com/VolcanoHawaiiKilaueaInstab.html (visited 11/24/2006)

Petersen, Mark D., Frankel, Arthur D., Harmsen, Stephen C., Mueller, Charles S., Haller, Kathleen M., Wheeler, Russell L., Wesson, Robert L., Zeng, Yuehua, Boyd, Oliver S., Perkins, David M., Luco, Nicolas, Field, Edward H., Wills, Chris J., and Rukstales, Kenneth S., 2008, Documentation for the 2008 Update of the United States National Seismic Hazard Maps: U.S. Geological Survey Open-File Report 2008–1128, 61 p.

Plafker, G., 1969, Tectonics of the March 27, 1964 Alaska earthquake: USGS Prof. Paper 543-I, 74 p.

Plafker, G., 1972, Alaskan earthquake of 1964 and Chilean earthquake of 1960: Implications and tectonics: Journal of Geophysical Research, v. 77, p. 901-925.

Plafker, G., Kachadoorian, R., Eckel, E.B., and Mayon, L.R., 1969, Effects of the earthquake of March 27, 1964, on various communities: U.S. Geological Survey Professional Paper 542-G, 50 p.

Resio, D.T., 1982, Report on wave climatology for Diablo Canyon, California, report to Pacific Gas and Electric Company, 43 pp.

Richmond, W.C., Burdick, D.J., Phillips, D., and Norris, P.J., 1981, Regional geology, seismicity, and potential geologic hazards and constraints, OCS oil and gas lease sale 53, northern and central California: USGS Open File Report 81-318, 39 p.

Rikitake, T., and Aida, I., 1988, Tsunami hazard probability in Japan: Bulletin of the Seismological Society of America, v. 78, p. 268-1278.

Satake, K., Smith, J.R., and Shinozaki, K., 2002, Three-dimensional reconstruction and tsunami model of the Nuuanu and Wailau landslides, Hawaii, in Takahashi, E., Lipman, P., Garcia, M., Naka, J., and Aramaki, S. (eds.), Hawaiian Volcanoes: Deep Underwater Perspectives: Geophysical Monograph 128, p. 333-346.

Satake, K., and Somerville, P., 1992, Location and size of the 1927 Lompoc, California earthquake from tsunami data: Bulletin of the Seismological Society of America, v. 82, p. 1710-1725.

Satake, K., Wang, K., and Atwater, B.F., 2003, Fault slip and seismic moment of the 1700 Cascadia earthquake inferred from Japanese tsunami descriptions: Journal of Geophysical Research, v. 108, no. B11, p. 2535.

Smith, J.R., Satake, K., Morgan, J.K., and Lipman, P.W., 2002, Submarine landslides and volcanic features on Kohala and Mauna Kea volcanoes and the Hana ridge, Hawaii, in Takahashi, E., Lipman, P.W., Garcia, M.O., Naka, J., and Aramaki, S., eds., Hawaiian Volcanoes, Deep Underwater Perspectives, Geophysical Monograph 128, Am. Geophys. Union, p. 11-28.

Strange, R.R. and Graham, N.,1982, A hindcast of severe storm waves at Diablo Canyon, California, report to Pacific Gas and Electric Company, 43 pp. – section 8

Tsunami Society, 2003. Mega tsunami hazards, at http://www.sthjournal.org/media.htm.

URS Corp (2010). Uncertainties in tsunami wave-height and run-up calculations, Report to Pacific Gas and Electric Company,, xx pp. .

US NRC (2007). A performance-based approach to define the site-specific earthquake ground motion, Regulatory Guide 1.208, March 2007.

Ward, S.N., 2001, Landslide tsunami: Journal of Geophysical Research, v. 106, p. 11,201-11,215.

Ward, S., and Day, S., 2001, Cumbre Vieja Volcano – Potential collapse and tsunami at La Palma, Canary Islands: Geophysical Research Letters, v. 28, p. 3397-3400.

Watts, P., 2004, Probabilistic predictions of landslide tsunamis off Southern California, Marine geology, 203, 281-301

Wells, D.L., and Coppersmith, K.J., 1994, New empirical relationships among magnitude, rupture length, rupture width, rupture area, and surface displacement: Bulletin of the Seismological Society of America, v. 84, p. 974-1002.

Wesson, R.L., Boyd, O.S., Mueller, C.S., Bufe, C.G., Frankel, A.D. and Petersen, M.D., 2007, Revision of time-independent probabilistic seismic hazard maps for Alaska, U.S. Geological Survey Open File Report 2007-1043, 33 pp.

Willingham, C.R., Rietman, J.D., Shiller, G.I., Heck, R.G., and DiSilvestro, L.A., 2006, in review, Seismic images of the Hosgri Fault Zone, offshore south-central California, in Keller, M.A. (ed.), Evolution of sedimentary basins/onshore oil and gas investigations-Santa Maria Province: U.S. Geological Survey Bulletin 1995CC.

Wills, C.J., Manson, M.W., Brown, K.D., Davenport, C.W., and Domrose, C.J., 2001, Landslides in the Highway 1 corridor: Geology and slope stability along the Big Sur coast between Point Lobos and San Carpoforo Creek, Monterey and San Luis Obispo Counties, California: California Division of Mines and Geology, Special Report to the Coast Highway Management Plan Caltrans District 5, Project F99TL34, 29 p.

Wyss, M., 1988, A proposed source model for the great Kau, Hawaii earthquake of 1868, Bull. Seism. Soc. Am., 78, 1450-1462.

Youngs, R. R. and K. J. Coppersmith (1985). Implications of fault slip rates and earthquake recurrence models to probabilistic seismic hazard estimates, Bull. Seism. Soc. Am., 75: 939 - 964.

APPENDIX 1
DIGITAL ELEVATION MODELS

TABLE OF CONTENTS

FIGURES

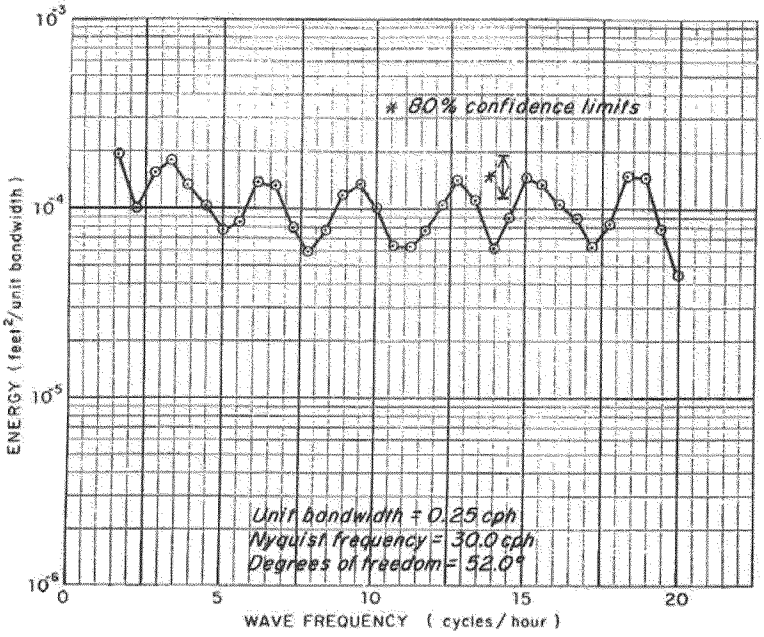

Long-wave energy spectrum at Diablo Canyon.
November 1966

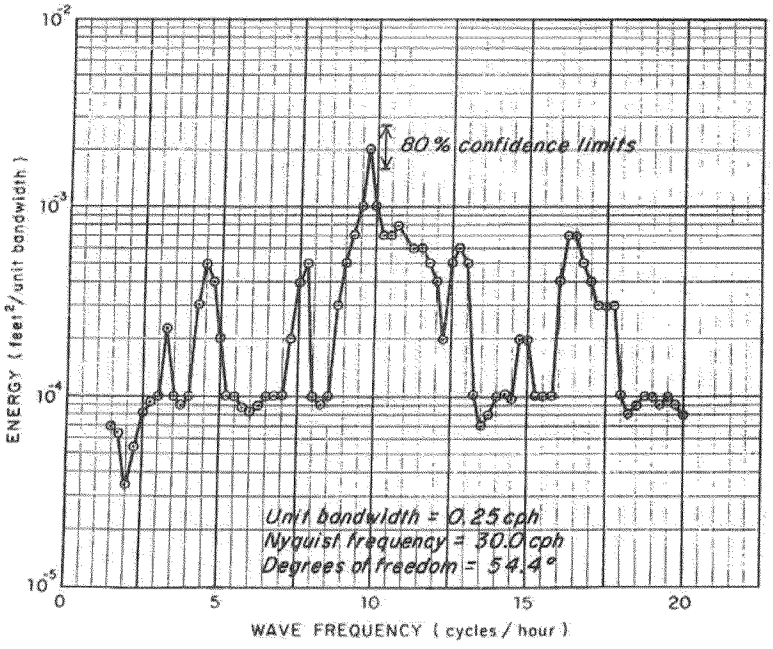

Long-wave energy spectrum at Avila.
November 1966

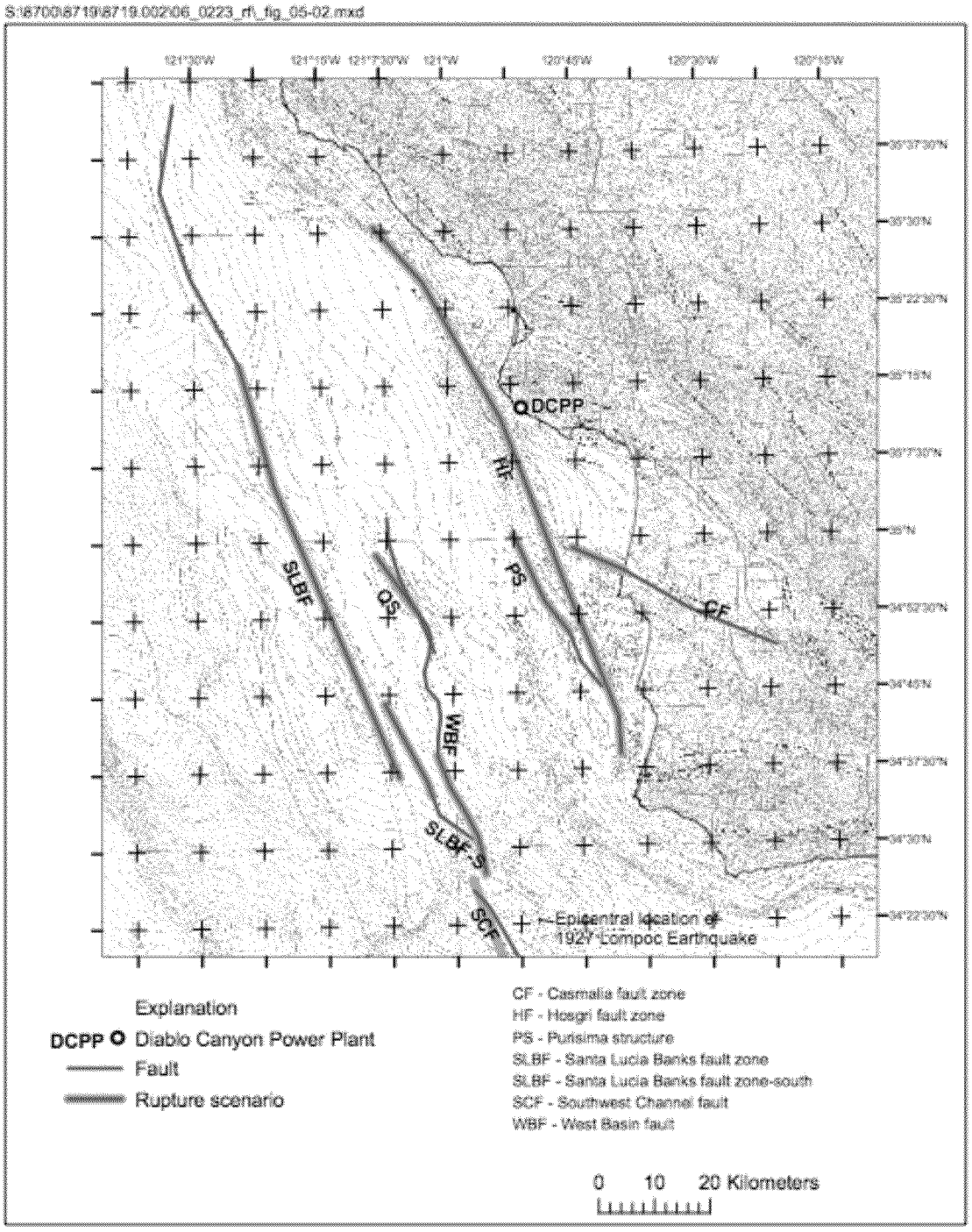

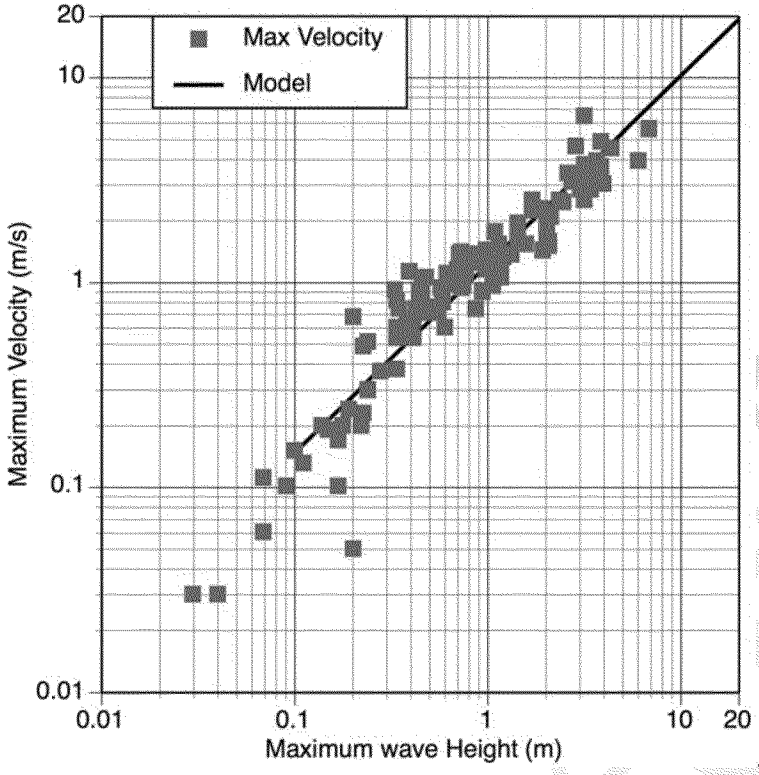

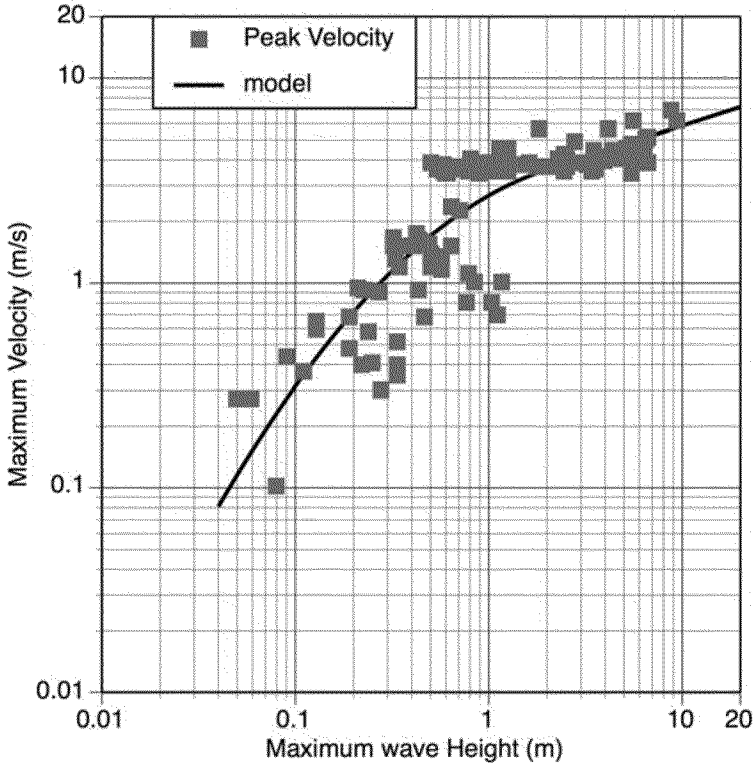

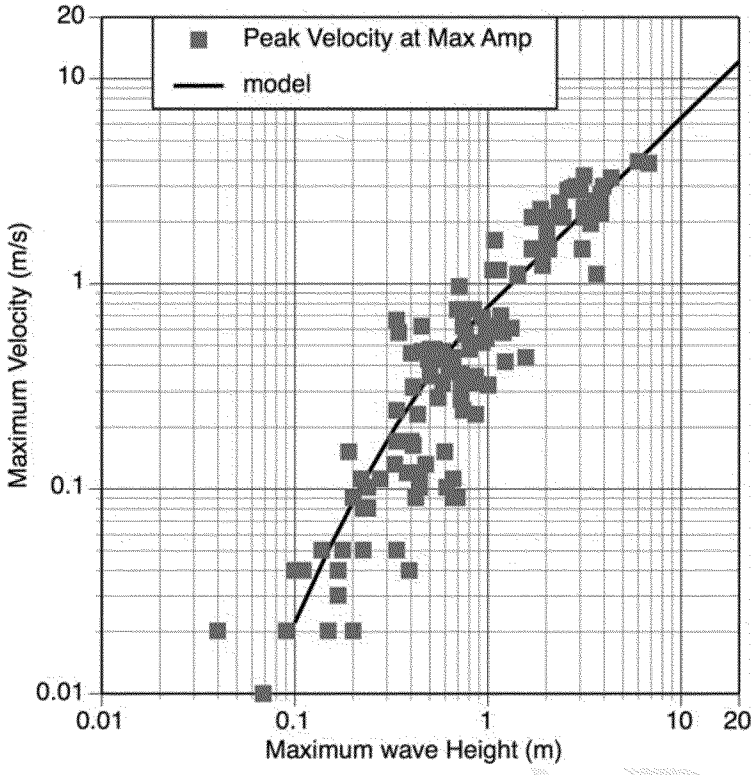

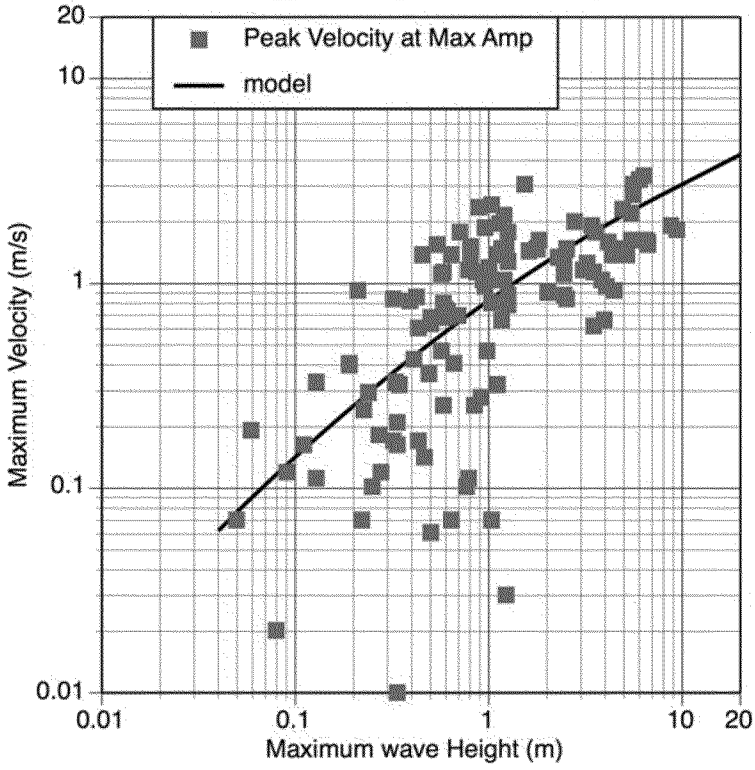

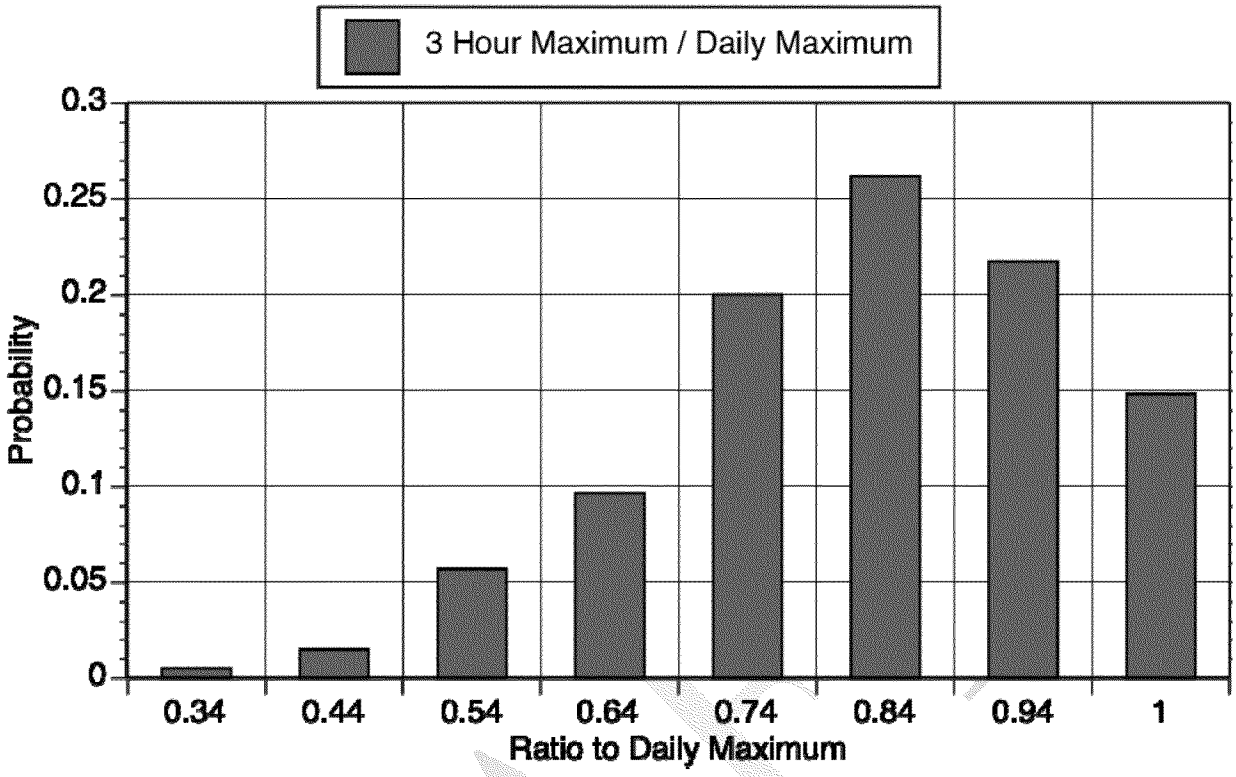

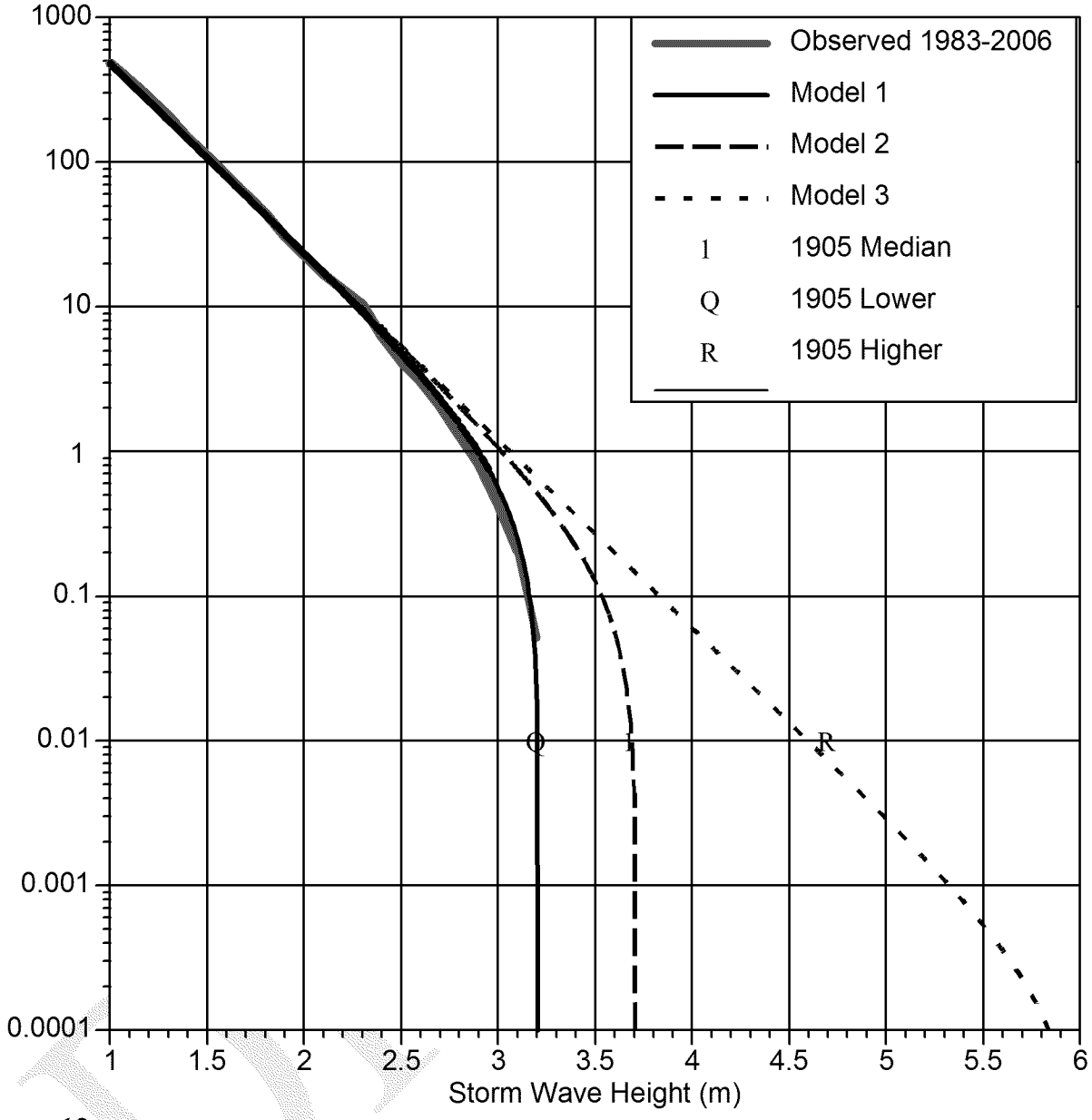

12

FIGURE 8-2. STORM HAZARD MODELS (WITHOUT TIDES) FOR 3 HOUR INTERVALS..... 12

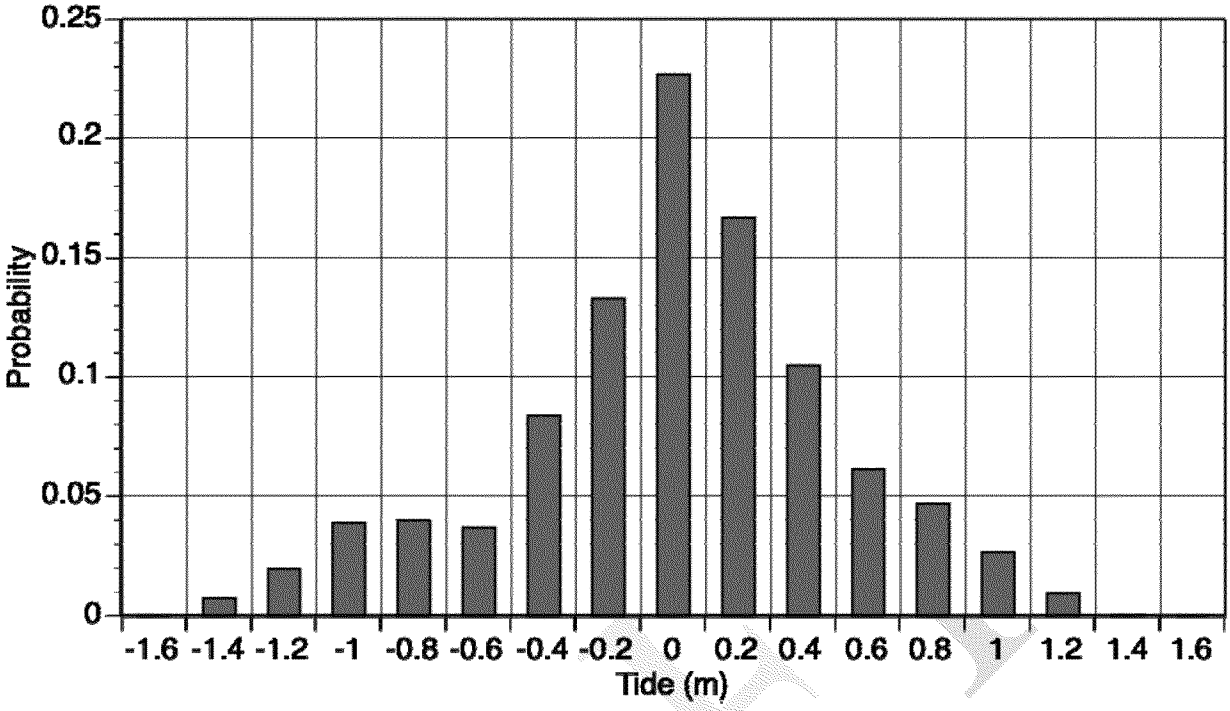

13

FIGURE 8-3. DISTRIBUTION OF TIDE LEVELS (LOW, MEDIAN, HIGH) AT DCPP FROM 2004 TO 2007..... 13

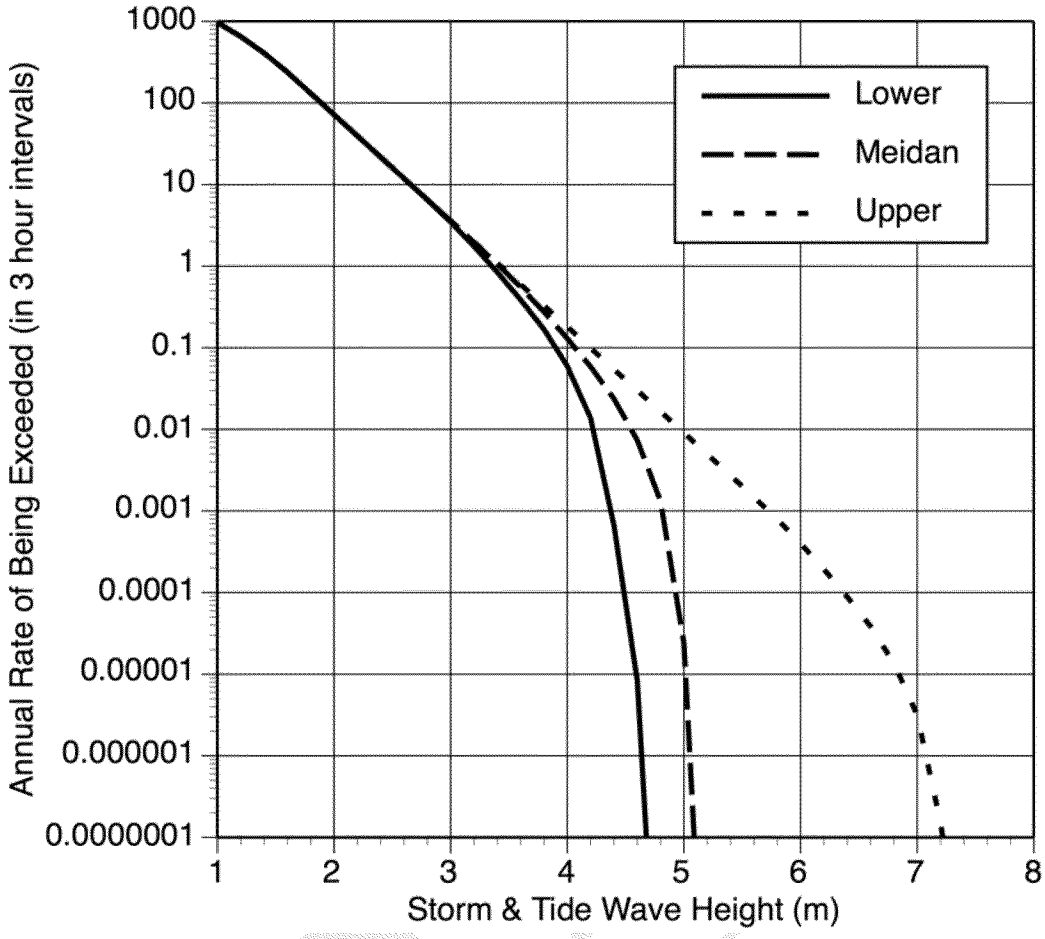

FIGURE 8-4. STORM AND TIDE HAZARD MODELS ABOVE MEAN SEA LEVEL FOR 3 HOUR INTERVALS..... 14

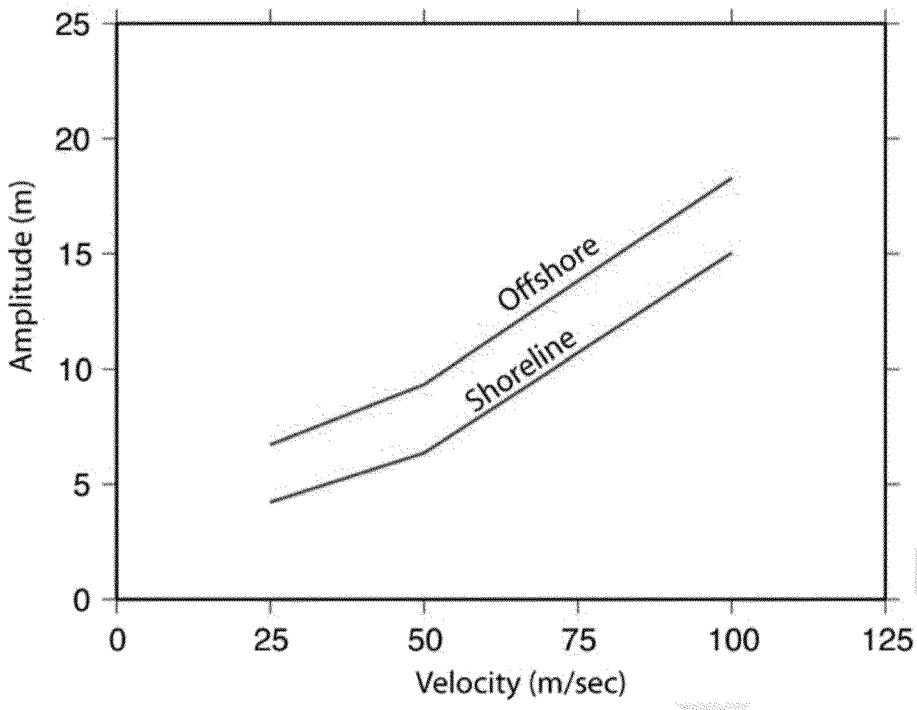

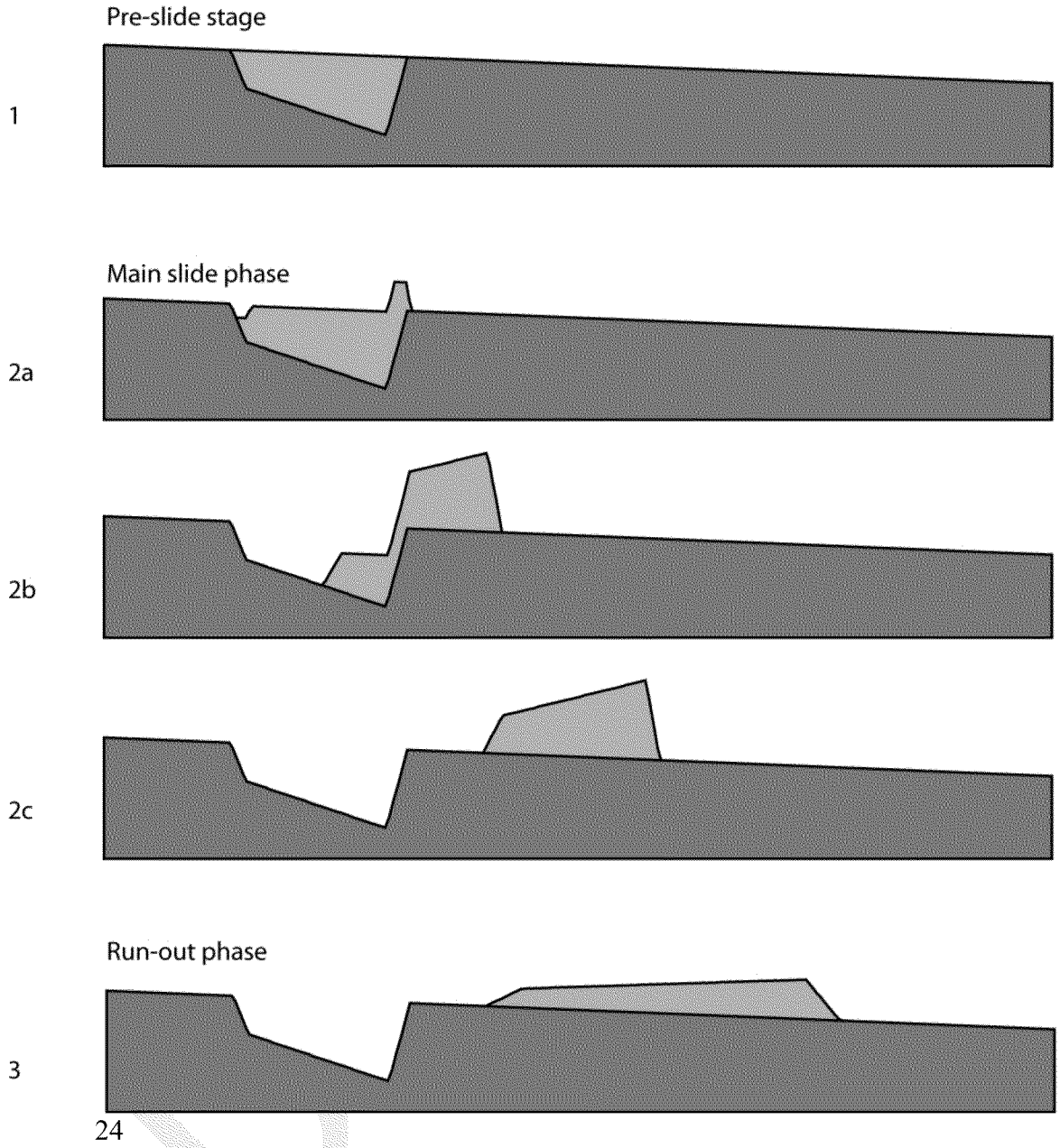

24

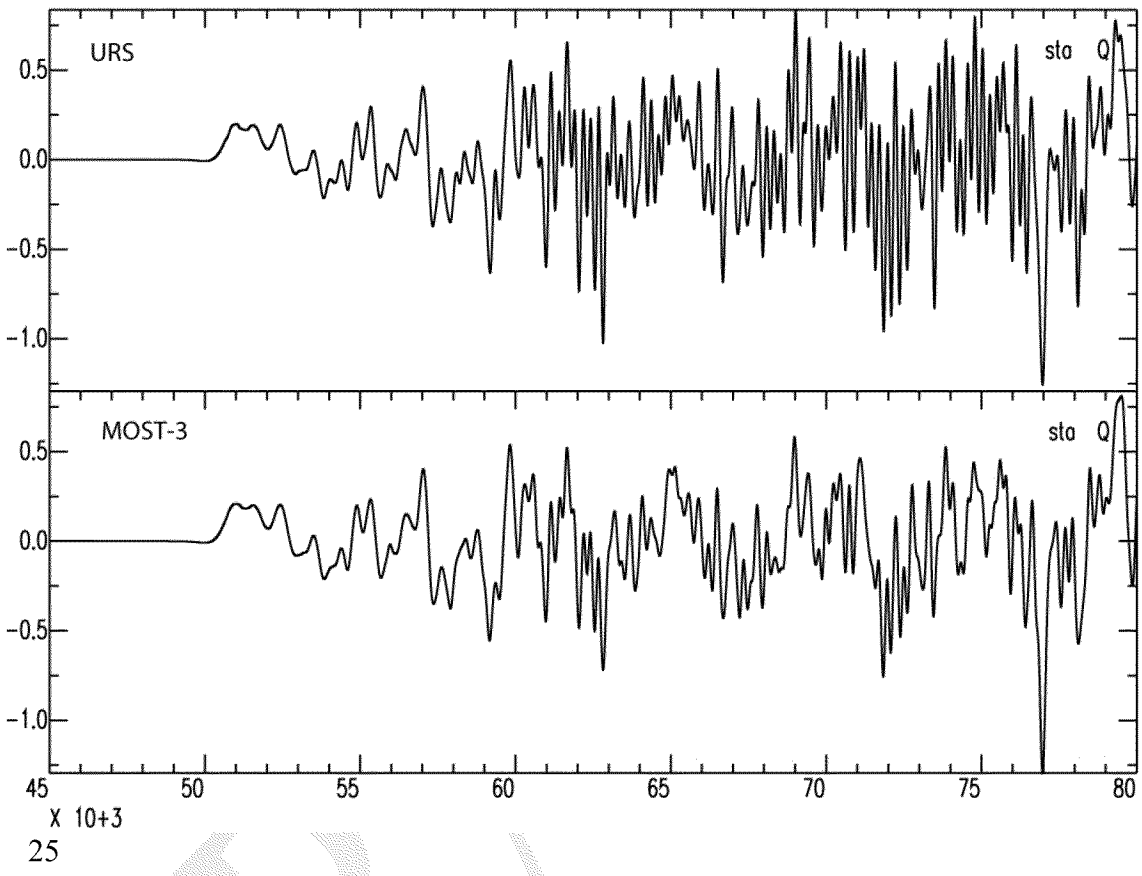

FIGURE A2-5 COMPARISON OF SIMULATED TSUNAMI WAVEFORMS FOR THE 1960 CHILE EARTHQUAKE USING THE URS (TOP) AND MOST (BOTTOM) CODES. 25

APPENDIX 1
DIGITAL ELEVATION MODELS

A1.1 INTRODUCTION

Five digital elevation models (DEMs) were constructed for the central California continental shelf and slope between latitudes 34° N to 36° N and longitudes 120° W to 122° W. Additional DEMs also were obtained from the Monterey Bay Aquarium Research Institute (MBARI). The DEMs were used for two objectives:

- To provide a reference sea floor and coastal zone topographic surface to be used in calculating tsunami propagation, run-up and drawdown effects at DCPP that could result from tsunamis generated either locally (within the model area) or from regional and far-field sources at greater distances, and
- To aid in the identification of potential local tsunami sources in the model area including slope failures (landslides and other forms of down-slope mass movement) and sea floor offsets resulting from faulting.

Figure A1-1 shows the outlines of the DEM areas incorporated into the project database. The Regional and Nearshore DEMs were used in the tsunami modeling analysis. The other DEMs were used in the analyses of sea floor features that are potential local tsunami sources.

A1.2 DATA SOURCES

Data from the following sources were incorporated into the DEMs:

- DCPP site hydrographic surveys conducted between 1967 and 1981,
- DCPP site topographic surveys conducted between 1966 and 2000 and re-compiled in 2001,
- The LTSP (Long Term Seismic Program) 1989 bathymetric chart compilations offshore DCPP,
- The NGDC/NOAA (National Geophysical Data Center/National Oceanic and Atmospheric Administration) Coastal Relief Model (90-meter grid) (NGDC, 2005),
- Digital elevation data from the USGS (U. S. Geological Survey) 7.5 minute topographic quadrangles within the model areas (10-m grid),
- Raw, unprocessed bathymetric survey data provided by NGDC/NOAA.

Additional details concerning the data and processing techniques used to create the grids are documented in FugroWest et al., (2005).

A1.3 DATA COMPILATION AND CHARTING PARAMETERS

The topographic and bathymetric data used for the digital elevation models were collected between 1933 and 2000 and were, at the time they were collected and first reported, referenced to various horizontal and vertical datums. All data points were referenced to the project datums listed below prior to being integrated into the digital models. Conversions were, for the most part, done in the GIS program ArcMap v 9.1. In some cases individual points were converted using Corpscon for Windows v 5.11.03 developed by the U.S. Army Corps of Engineers.

UNITS USED IN THE REPORT AND DIGITAL DATA SETS

Linear units are meters (m) or kilometers (km).

Angular units are degrees (o).

Geographic coordinates are in the report are in degrees and decimal minutes.

Geographic coordinates in the DEMs are in decimal degrees to 10 places.

UTM coordinates are in meters.

PROJECT VERTICAL DATUMS

All DEM elevation data are in meters referenced to mean lower low water (MLLW). Sea floor elevations are negative, onshore elevations positive. The following vertical datums are now commonly in use along the central California coast by NOS/NOAA and U.S. Geological Survey.

Bathymetric vertical datum – Mean Lower Low Water (MLLW); and

Topographic vertical datum – Mean Sea Level (MSL).

Mean Sea Level (MSL) is the reference datum for plant elevations at DCPP. MLLW is 2.6 feet (0.8 m) below MSNL (DCM T-9, Rev 13-A, 4.4). Along the central California coast the difference between MSL and MLLW ranges from 0.83 m to 0.86 m. The closest reporting station to DCPP is Port San Luis where NOAA (2003) reports that MSL is 0.853 m above MLLW. For the DEMs developed in this study all elevations (offshore and onshore) are referenced to MLLW. Offshore elevations are negative, onshore are positive. The onshore elevations were converted to MLLW datum by adding 0.8 m to each data point.

PROJECT HORIZONTAL DATUM

Horizontal datum – North American Datum of 1983 (NAD 83);

Grid – Universal Transverse Mercator (UTM), Zone 10 North in meters; and

Geographic Coordinates are in decimal degrees to 10 places.

The Regional DEM is available in both UTM and geographic coordinate systems. All other DEMs are in UTM coordinates. Additional details concerning the data and processing techniques used to create the grids are documented in FugroWest et al., (2005).

A1.4 SEA FLOOR AND TOPOGRAPHIC REFERENCE SURFACES FOR TSUNAMI MODELING

Two DEMs were constructed to provide a reference surface for the tsunami modeling, a Nearshore DEM for the 5 to 10 kilometer area surrounding the DCPP and a Regional DEM to cover the entire project area.

The ***Nearshore DEM*** contains elevation points on a 5-meter grid. The DEM extends approximately 5 kilometers (km) north and south of DCPP, up to 10 km offshore and 0 to 10 km onshore at the northeast corner (Figure A1-1). It is based on the integration of data compilations conducted for the LTSP in 1989, data from the DCPP onshore and offshore site surveys, and 10-m onshore DEM grid data from the USGS.

The 1989 LTSP data compilations included data sets from the National Ocean Survey (NOS) of NOAA, data collected during geophysical surveys conducted for PG&E between 1976 and 1988, and data collected for the Minerals Management Service (MMS) of the USGS in the 1970s and 1980s.

The DCPP site surveys include two offshore surveys and a compilation of onshore survey data. The offshore surveys cover Diablo Cove, directly offshore DCPP, and the Intake Cove immediately to the south of DCPP. These data were collected on surveys conducted for PG&E in 1967/1968 and 1981. The offshore surveys extend approximately 600 m north and south of DCPP and up to 400 m offshore. Elevations in the offshore area nominally range from 0 m (MLLW) to -30 m. The onshore surveys were compiled by WLA (2001) from a number of individual surveys that were not previously tied together. The plant site topographic surveys cover an area from the coastline to about 1600 m inland and extend approximately 800 m north of DCPP and 1600 m south of the DCPP. Elevations in the onshore survey area range from 0 m (MLLW) to over 400 m.

The nominal sea floor elevations in the offshore area of the DEM are 0 m to -120 m. Onshore elevations range from 0 m to 556 m. Comparisons of published bathymetric charts for the same area were conducted to determine overall precision, accuracy and degree of consistency among various sources used. The largest differences between the PG&E, NOAA Chart series and NOAA Coastal model are along the slope at water depths greater than 120 m.

The ***Regional DEM*** is modified from the NGDC/NOAA Coastal Relief Model for California (NGDC, 2005). The Regional DEM is presented on a 90-m grid in UTM Zone 10 North, NAD 83 coordinates and on a 3-arc-second grid in geographic, NAD 83 coordinates. The publicly available digital Coastal Relief Model is based on analog surveys from the 1930s through the 1970s, post-1970 single beam digital surveys, multibeam surveys collected in 1988 and later and onshore topographic data from the USGS. The Regional DEM grid incorporates the Coastal Relief Model within the study area defined by the geographic coordinates in Section A1.1 above. The nominal sea floor elevation range for this grid is 0 m to deeper than -3,500 m at the base of the Santa Lucia Escarpment. The regional grid also incorporates two minor modifications to the Coastal Relief Model, which are the following: 1) the area covered by the Nearshore DEM has been deleted from the Regional DEM grid and replaced with points from the Nearshore DEM; and 2) the coordinates are converted from geographic, NAD 83 to UTM Zone 10 North, NAD 83, the project coordinate system, and the data re-projected on a 90-m grid. The boundaries between the Nearshore and Regional DEM grids have been checked to ensure that there are no discontinuities related to the processing or use of different data sets. As indicated above, the Regional DEM is presented in both UTM and geographic coordinate systems.

A1.5 REPROCESSED DEMS

More detailed, higher quality DEMs were created for different parts of the study region to aid in interpreting the geology and sea floor morphology that was needed to identify and characterize features that represent potential tsunami sources. The reprocessed bathymetry DEMs were specifically developed for this project by reprocessing raw (unprocessed) bathymetry data obtained from NOAA including: (1) multibeam survey data for the offshore Santa Maria basin and Santa Lucia Bank (Figure A1-2); (2) single beam data for portions of the Santa Lucia escarpment, and (3) the near shore region above the 200 m isobath (Figure-A1-1).

The raw data are the same data used by NGDC to develop the Coastal Relief Model on a 3-arc-second (90 m) grid. In order to identify smaller-scale bathymetric features (areas of unstable slopes and active faulting that could be local sources of tsunamis), we reprocessed the raw survey data to develop databases on 50-m grids. The three reprocessed DEMs are along the coastal strip, in the NOS multibeam survey areas, and along the Santa Lucia escarpment.

The ***Coastal Strip DEM*** covers a nominal 5-km to 25-km-wide strip along the part of the central California coast within the study area (Figure A1-1). It is based on raw bathymetric data from NOS surveys in the area. The data were reprocessed to provide a greater data density than available from the 90-meter grid or 3-arc second grid NGDC/NOAA Coastal Relief Model (NGDC, 2005). Bathymetric data in this coastal strip area reflect the Hosgri-San Simeon fault zone and slumps along a break in slope that occurs in a nominal water depth of 120 m to 150 m. The *Coastal Strip DEM* compliments the D-Series Maps of the LTSP and provides a digital database on a 75-m grid (Figure A1-3).

We created a separate ***Multibeam Bathymetry DEM*** from the raw NOAA data to provide higher resolution images in those areas covered by the 1988 and later multibeam surveys (Figure A1-2). These reprocessed data provide greater detail of the sea floor morphology to help evaluate the geology of the Santa Lucia Bank fault and a proposed landslide in the upper slope region off Point San Luis. This latter feature is herein referred to as "the Pismo feature" in Section 6 of the text. Eleven multibeam surveys were conducted offshore central California from 1987 through 1997. Data from five of these surveys (B00117, B00118, B00157, B00161, and B00162) were integrated to generate the *Multibeam Bathymetry DEM* shown in Figure A1-4). Data density over most of the DEM area outlined in Figure A1-4 is very detailed (<25 m spacing). In regions of sparse data, the DEM was interpolated between available data points.

A more detailed, higher quality DEM than the NGDC Coastal Relief Model was created for a region covering the Santa Lucia escarpment (Figure A1-5). The ***Escarpment DEM*** represents the highest-resolution coverage of publicly available bathymetry data in this region of offshore Central California. The visual renderings of these data are used to assist in interpreting the geology of the Santa Lucia escarpment to identify and characterize features that could represent past and/or potential tsunami sources.

The ***Escarpment DEM*** was created by integrating over 1.3 million data points from all available datasets, including NOS hydrographic survey data, portions of six multibeam

surveys and 25 data sets with individual survey tracklines. However, data coverage is sparse for much of the area except where multibeam data are available. The lack of data density impacts accuracy and therefore the DEM should be used with caution in these areas with limited data coverage. The *Escarpment DEM* data are intended for interpretation and mapping at a scale of 1:100,000 or smaller. Mapping at larger scales (e.g., 1:50,000) is not recommended with this data. The vertical accuracy of this DEM is difficult to evaluate because of the large size (~1.3 million points) of the dataset and the large range of water depth values in the data set. A vertical error of ±1 to± 2 percent of the water depth would be in-line with the NOS and USC&GS estimates for their survey data.

A1.6 OTHER BATHYMETRIC DATA SETS

Additional detailed bathymetry data within the study region for the Monterey Bay and Santa Barbara Channel regions were obtained from the Monterey Bay Aquarium Research Institute (MBARI) (MBARI, 2000 and 2001). The Santa Barbara Channel data were incorporated into the project GIS and were used to provide more detailed geomorphology for comparison to the landslide analogs in this region.

A1-7 REFERENCES

Furgo West, Inc., 2005, Geomatrix Consultants, Inc., and William Letters & Associates, Inc., 2005, Evaluation of Potential tsunami sources in the Diablo Canyon Power Plant region, Final Report, the digital elevation Models: unpublished report submitted to Pacific Gas and Electric Company, November, 46 p.

Monterey Bay Aquarium Research Institute (MBARI), 2000, Monterey Bay multibeam survey: Digital Data Series No. 3.

Monterey Bay Aquarium Research Institute (MBARI), 2000, Santa Barbara multibeam survey: Digital Data Series No. 4.

National Geophysical Data Center (NGDC), 2005, Southern California Coast geophysical data system (GEODAS) for gridded bathymetric data, Coastal relief model, v. 6, ver. 4.1, compact disk.

National Oceanic and Atmospheric Administration (NOAA), 2003, Tidal datums at Port San Luis, Pacific Ocean, California: Published Bench Mark Sheet for 9412110, Available online at http://140.90.121.76/benchmarks/9412110.html.

Pacific Gas and Electric Company (PG&E), 2004, Diablo Canyon Power Plant Design Criteria Memorandum No. T-9, Wind Tornado, and Tsunami, revision 14, p. 119.

Pacific Gas and Electric Company (PG&E), 1989, Response to NRC question 43p, Diablo Canyon Long Term Seismic Program, U.S. Nuclear Regulatory Commission docket nos. 50-275 and 50-323, 10 charts, scale 1:24,000.

William Lettis & Associates (WLA), 2001, Data Report A: Geologic Mapping in the Plant Site Area and ISFSI Study Area, Diablo Canyon ISFI. Prepared for Pacific Gas and Electric Company, 42 p., 23 photographs, and 3 maps, December 18.

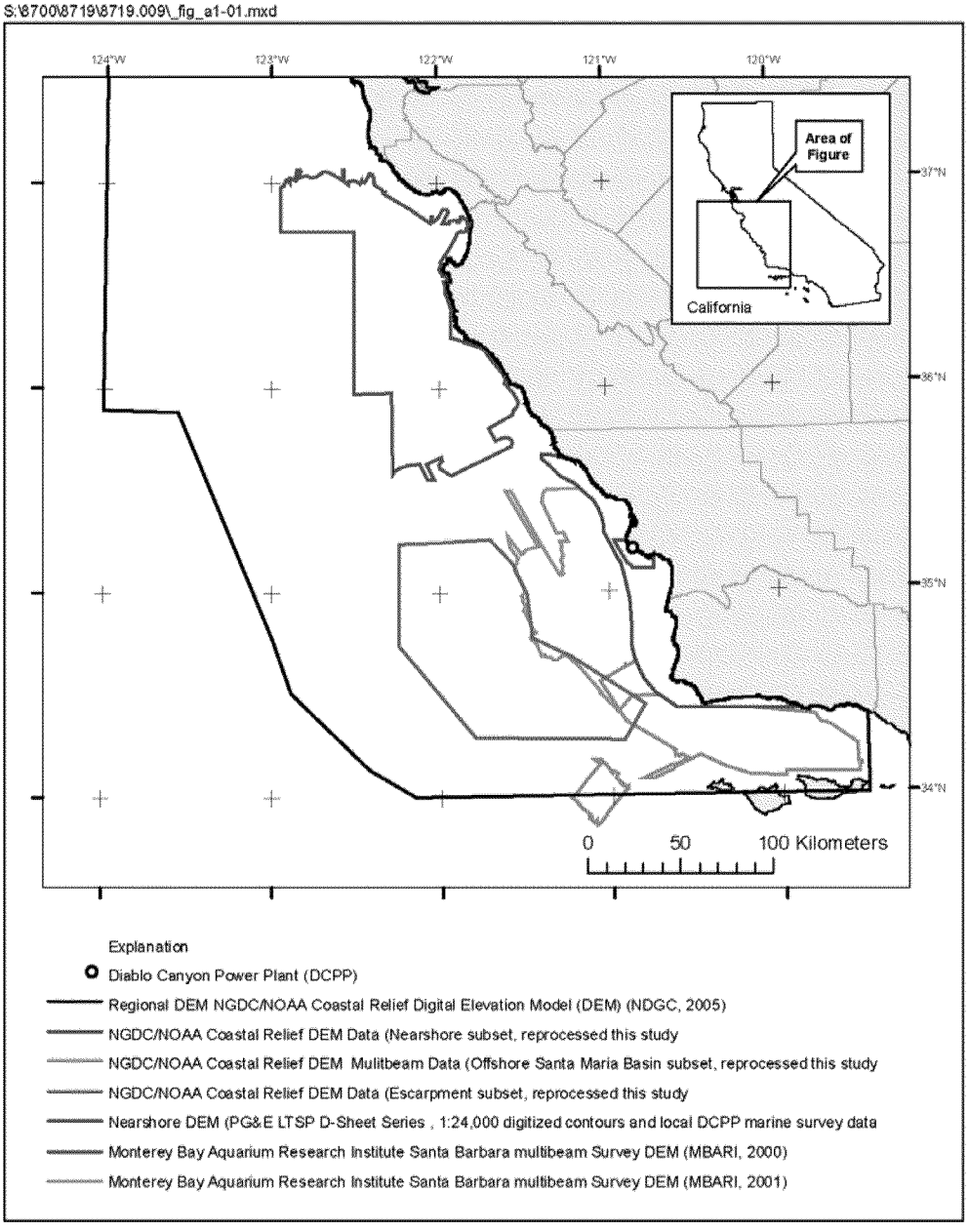

Figure A1-1 Boundaries of the DEM Areas

S:\8700\8719\8719.002\06_0223_rf_fig_A1-02.ai

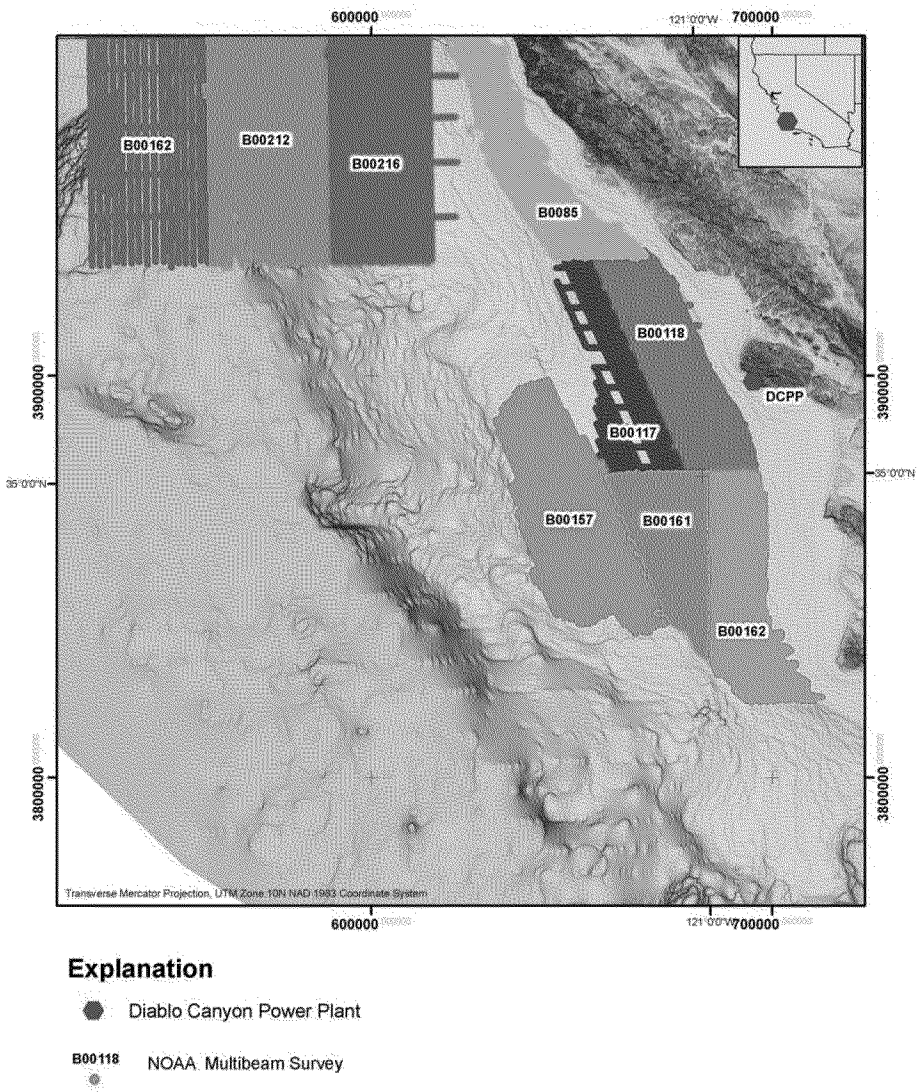

Figure A1-2 NOS/NOAA Multibeam Bathymetry Surveys Offshore Central California

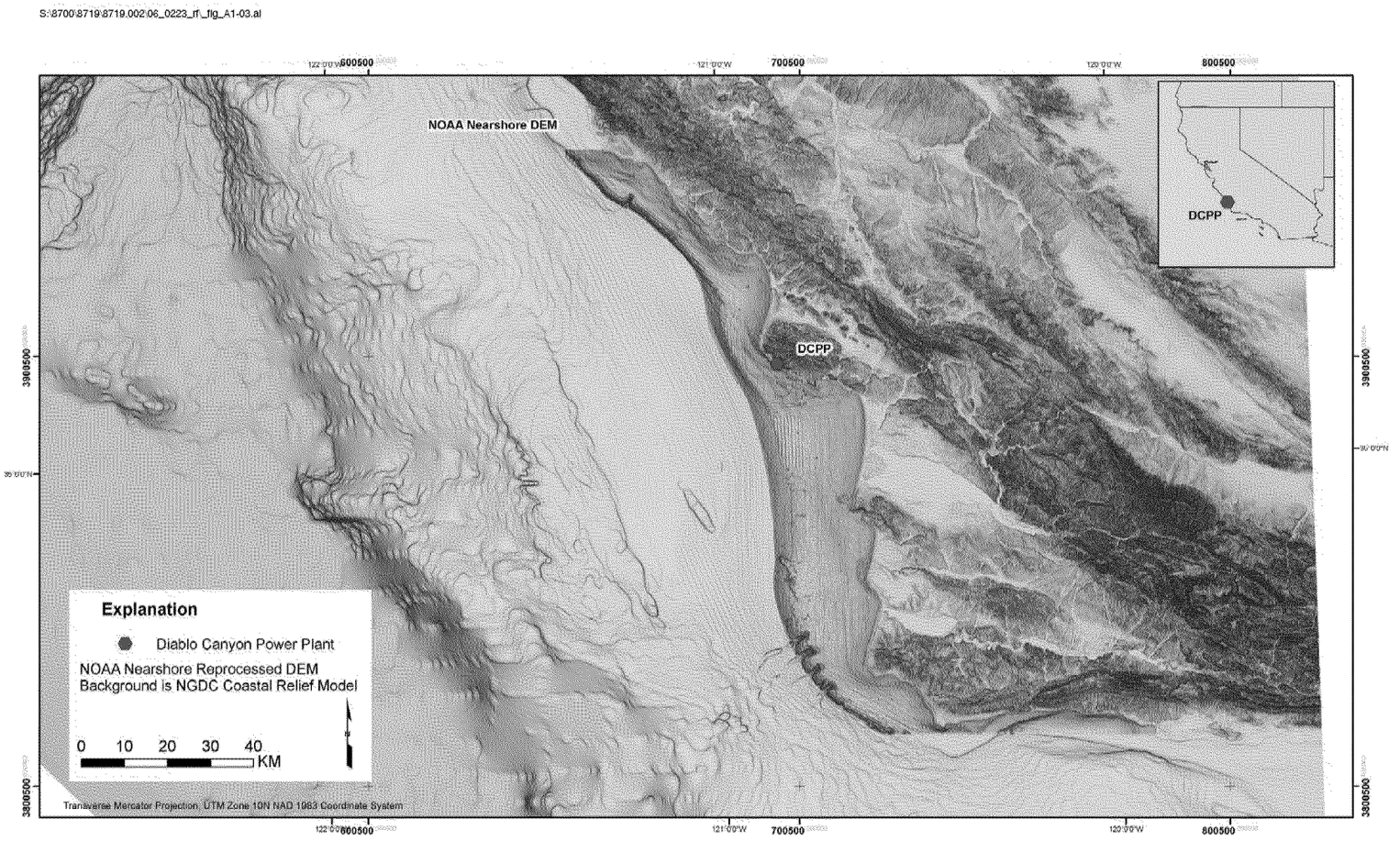

Figure A1-3 Coastal Strip DEM with NGDC/NOAA Coastal Relief DEM

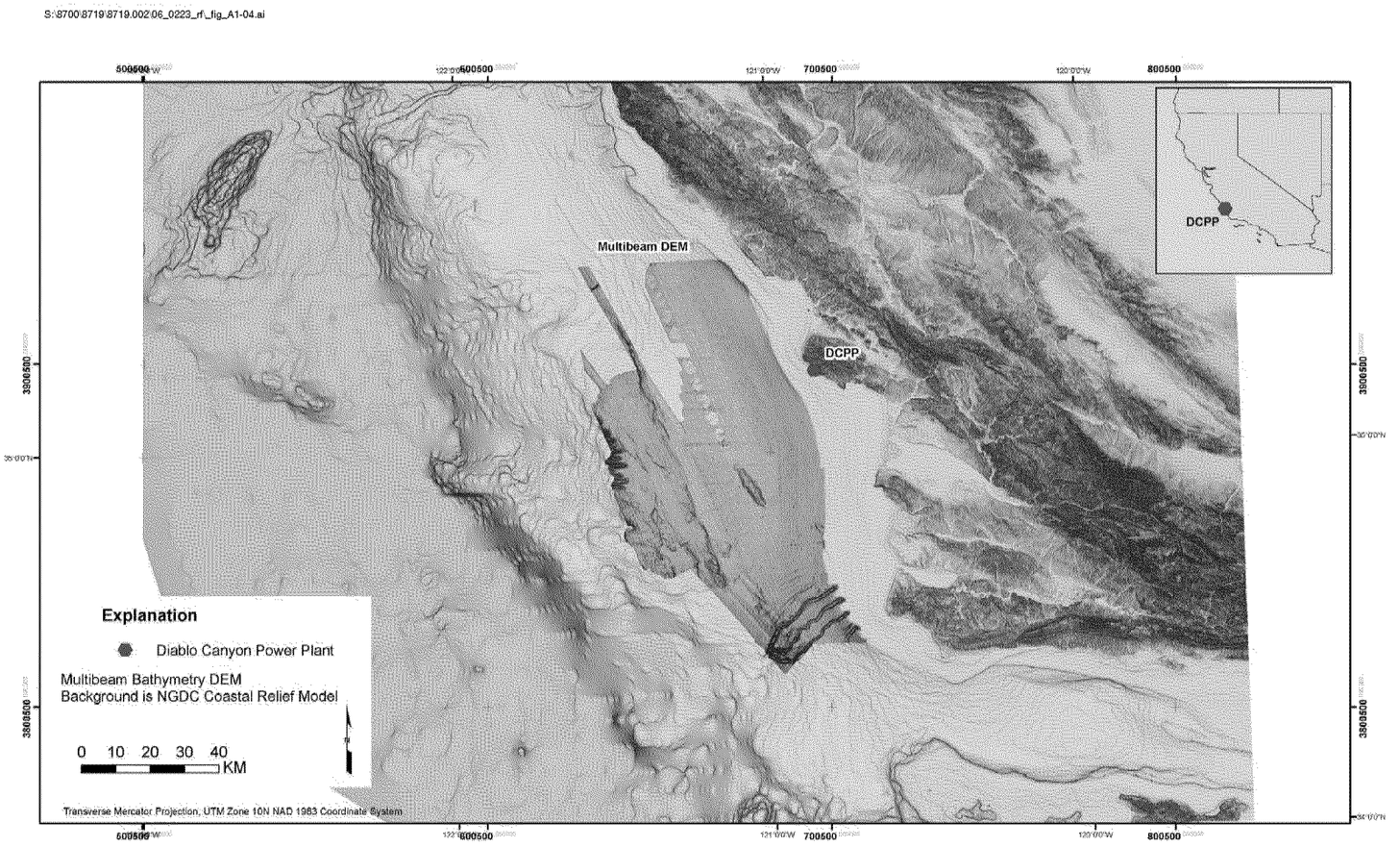

Figure A1-4 Multibeam Bathymetry DEM with NGDC/NOAA Coastal Relief DEM

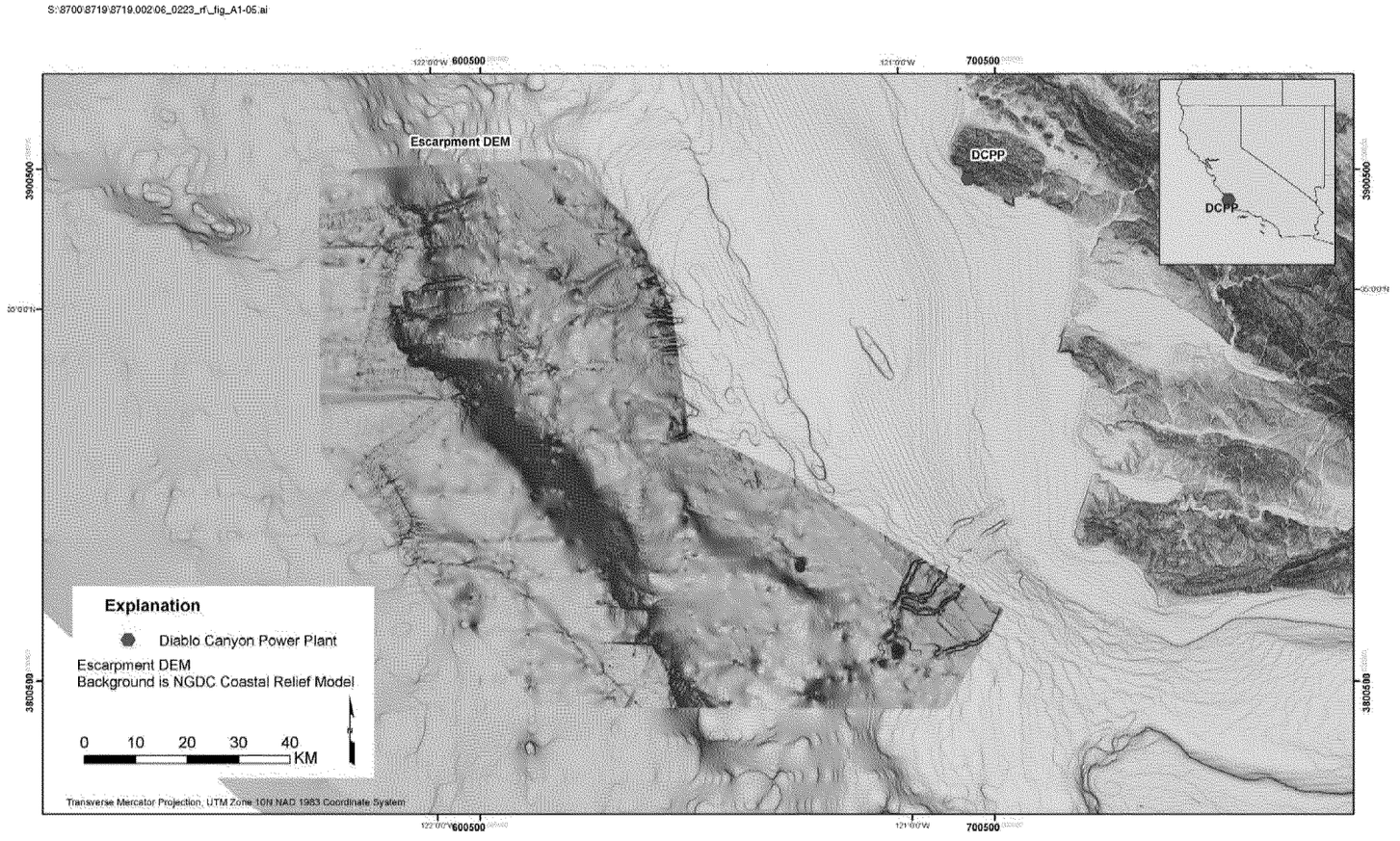

Figure A1-5 Escarpment DEM with NGDC/NOAA Coastal Relief DEM

APPENDIX 2
TSUNAMI MODELING

TABLE OF CONTENTS

FIGURES

Appendix 2
TSUNAMI MODELING

A2.1 METHODOLOGY

We take a Eulerian approach to describe the particle motion of the fluid. Only the velocity changes of the fluid are described at some point and at some instant of time, rather than describing its absolute displacement. We consider a wave that is a propagating disturbance from an equilibrium state. Gravity waves occur when the only restoring force is gravity. When the horizontal scale of motion is much larger than the water depth, then the vertical acceleration of water is much smaller than the gravity acceleration and thus negligible. This means that the whole water mass from the bottom to the surface is assumed to move uniformly in a horizontal direction. This kind of gravity wave is also known as a "long wave." Long-wave approximations are appropriate when the water depth of lakes and oceans (< 5 km) is much smaller than the length of the disturbance (fault lengths ~10-1,000 km).

General Linear Gravity Wave

The following is a derivation of the general case of gravity waves for two dimensions where x is the horizontal direction and z is the vertical direction. We start from the Euler's equation of motion that considers the conservation of momentum on a volume of water. The Newton equations can be simplified as, (Eq 1.)

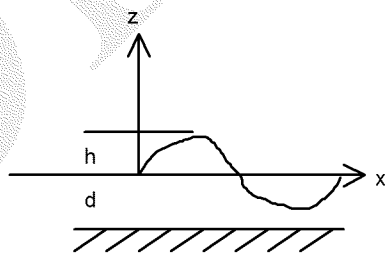

$$\frac{d}{dt}V = g - \frac{1}{\rho}\nabla p$$

where d/dt is the total and $\partial/\partial t$ is the partial derivative with respect to time, g is the gravitational acceleration, $V = (u,w)$ are the depth-averaged velocities in the x and z directions, ρ is the density, and p is the fluid pressure. The figure shows that h is the tsunami wave height and d is the water depth. We next consider the conservation of mass to derive the equation of continuity,

$$\frac{\partial \rho}{\partial t} + \nabla \cdot (\rho V) = 0$$

and for incompressible fluid becomes,

$$\nabla \cdot V = 0 .$$

From the Euler's equation of motion, the horizontal and vertical acceleration components are,

$$\frac{du}{dt} = -\frac{1}{\rho}\frac{\partial p}{\partial x}$$
$$\frac{dw}{dt} = -g - \frac{1}{\rho}\frac{\partial p}{\partial z}$$

The relationship between h and p is related through the hydrostatic pressure equation,

$$p = -\rho g(h - z) + p_0$$

where h is the wave height, z is the water depth, and p_0 is the pressure of one atmosphere at $z = 0$ and $h = 0$. The horizontal and vertical pressure gradients given from the slope of the water surface,

$$\frac{\partial}{\partial x} p = pg\frac{\partial h}{\partial x}$$
$$\frac{d}{dz} p = -\rho g$$

are combined with the Euler's equation to give the horizontal and vertical components,

$$\frac{du}{dt} = -g\frac{\partial h}{\partial x}$$
$$\frac{dw}{dt} = 0$$

For ocean tsunamis, the non-linear advective term is small and can be ignored; therefore, the equation of motion is,

$$\frac{du}{dt} = \frac{\partial u}{\partial t} + u\frac{\partial u}{\partial x} \approx \frac{\partial u}{\partial t}$$
$$\frac{\partial u}{\partial t} = -g\frac{\partial h}{\partial x}$$

We next consider the conservation of mass for a region with a small length *dx*. Since the volume change per unit time must be equal to the flow rate of water going out of this region, we can therefore write

$$\frac{\partial}{\partial t}\{(h+d)dx\} = -\frac{\partial}{\partial x}\{u(h+d)\}dx$$
$$\frac{\partial h}{\partial t} = -\frac{\partial}{\partial x}\{u(h+d)\}$$
$$\frac{\partial h}{\partial t} = -\frac{\partial}{\partial x}(du)$$

which is the simplified equation of continuity when the amplitude of the wave is small compared to the water depth. The so-called small-amplitude, linear, long-wave assumption is valid for most tsunami propagation paths except near coasts.

Nonlinear Gravity Waves and Shallow Water Waves

Without a viscous force to dissipate wave energy, the water motion will continue forever. In order to include the viscous effect, we can add a term for viscous stress to the equation of motion. We only consider a shear stress at the water bottom, and the normal stress is already included and equal to the pressure. The shear stress is experimentally estimated as

$$\tau_x^{\,b} \approx C_f v_x \sqrt{v_x^{\,2} + v_y^{\,2}}$$

and the frictional force is

$$F_x^{\,b} = C_f \frac{v_x \sqrt{v_x^{\,2} + v_y^{\,2}}}{d+h}.$$

Satake (1995) adopted two types of frictional coefficients from engineering hydrodynamics for including bottom friction for tsunamis. These are the De Chezy (*C*) and Mannings's roughness (*n*) coefficients. These have different dimensions; therefore, a nondimensional frictional coefficient C_f is related to these two coefficients by

$$C_f^{\,2} = \frac{g}{C_c^{\,2}}$$

and

$$C_f = \frac{gn^2}{(d+h)^{1/3}}.$$

The Manning's roughness coefficient n is used for a uniform turbulent flow on a rough surface. It indicates that the bottom friction varies with water depth. We use an n of 0.03 $m^{-1/3}$ s, typical for coastal waters. If n is translated to C_f, then n becomes 2.3×10^{-3} for a total depth of 50 m and 1×10^{-2} for a total depth of 0.6 m, which agree well with observational values of tidal flow and rupup of solitary waves (see Satake, 1995).

Since the Earth is rotating, there is a force apparently acting on a body of water. In an inertial reference frame (fixed on the rotating Earth), this force is called the Coriolis force. The derivation of this term is beyond the scope of this report, and we refer the reader to textbooks on analytical mechanics. The vertical component of the Coriolis force is much smaller than gravity (3 cm/s^2 compared to 980 cm/s^2 at 4,000-m depth). In a local Cartesian coordinate system, the horizontal components are given by

$$F_x^{\ cor} = -fv_y$$
$$F_y^{\ cor} = fv_x$$

where f is the Coriolis parameter, and this force always acts to the right-hand side of the motion in the northern hemisphere. The Coriolis force is only significant for long propagation times and distances along lines of latitude near the equator.

We derive the equations for general gravity waves without making the small-amplitude, linear long-wave approximation appropriate when the wave height is much smaller than the water depth (h<<d). If we expand the hyperbolic tangent function using the Taylor series expansion and include the first- and second-order terms, then the corresponding equation of motion becomes

$$\frac{\partial u}{\partial t} = -g\frac{\partial h}{\partial x} + \frac{1}{3}d^2\frac{\partial^3 u}{\partial x^2 \partial t}$$

which is also known as the Boussinesq equation. After relaxing the small-amplitude assumption, the equation of motion and continuity are given as

$$\frac{du}{dt} + u\frac{\partial u}{\partial x} = -g\frac{\partial h}{\partial x}$$
$$\frac{\partial h}{\partial t} = -\frac{\partial}{\partial x}\{u(h+d)\}$$

These equations are for the finite-amplitude shallow water waves. For the linear case, the phase velocity is given by $c = \sqrt{g(d+h)}$. In the nonlinear case the phase velocity is given by the following Taylor series expansion of the hyperbolic tangent function,

$$c = \sqrt{gd\left[1 - \frac{2\pi^2}{3}\left(\frac{d}{\lambda}\right)^2\right]}$$

where λ is the wavelength. Note that in the nonlinear case, there is a phenomenon of amplitude dispersion: the larger the amplitude, the faster the wave speed. As a consequence, peaks of a wave catch up with troughs in front of them, and the forward-facing portion of the wave continues to get steeper. This wave will eventually break.

Including the bottom friction and Coriolis force, the equation of motion for shallow water waves can be written for a two-dimensional case as follows:

$$\frac{\partial U}{\partial t} + U\frac{\partial U}{\partial x} + V\frac{\partial U}{\partial y} = -fV - g\frac{\partial h}{\partial x} - C_f\frac{U\sqrt{U^2+V^2}}{d+h}$$

$$\frac{\partial V}{\partial t} + U\frac{\partial V}{\partial x} + V\frac{\partial V}{\partial y} = -fU - g\frac{\partial h}{\partial y} - C_f\frac{V\sqrt{U^2+V^2}}{d+h}$$

and the equation of continuity is

$$\frac{\partial h}{\partial t} + \frac{\partial}{\partial x}\{U(h+d)\} + \frac{\partial}{\partial y}\{V(h+d)\} = 0$$

where the coordinate system is x = east, y = south, f is the Coriolis parameter, C_f is a non-dimensional frictional coefficient, and U and V are the average velocities in the x and y directions, respectively. The first term on the left-hand side (lhs) is the local acceleration term, the second and third terms on the lhs are the advection terms, the first term on the right-hand side (rhs) is the Coriolis force, the second term on the rhs is the restoring force from gravitation acceleration, and the third term on the rhs is the bottom friction force.

Numerical Computation

The equations of motion and equation of continuity are converted from Cartesian to a spherical coordinate system $(x,y,z) \rightarrow (r,\theta,\varphi)$ with the origin at the Earth's center, but r is constant and equal to the Earth's radius R. Note that θ is the colatitude and measured southward from the North Pole and φ corresponds to longitude measured eastward from the Greenwich meridian. These equations are solved by the finite-difference method

using the staggered leapfrog method (e.g., Satake, 1995). For the advection terms, upwind difference scheme is used (e.g., Press et al., 1992). The land-sea boundary condition in the linear computation is total reflection, and in the nonlinear case there is a moving boundary condition and runup is considered. The time step of computation is determined to satisfy the stability condition (Courant condition) of the linear, and by trial and error for the nonlinear finite-difference computations.

Variable Grid Finite Difference

The variable grid setup consists of a master grid with a coarse grid spacing and a number of nested finer grids with decreasing grid sizes around areas of interest. Our code allows for more than one area with decreased grid size, which we used for our Hawaii scenarios, where the source region (around Hawaii) as well as the target region around DCPP are sampled at smaller intervals. In this model, the deep ocean part is sampled at 300 arc seconds (9 km horizontal resolution). Because of the very long wave length of the tsunami waves in the deep ocean, such a sampling is sufficient for accurate results and reduces the computation time and memory requirements considerably. In the source region, the Hawaiian Islands, we used a grid with 60 arc sec (1.85 km) resolution, and in the DCPP region we used several nested grids stepping down to 0.8 arc sec (~25 m) at the site. The time step for these runs is 0.2 sec. For the local landslide and fault scenarios, we used a master-grid at 4.5 arc seconds (140 m) with three nested finer grids stepping down a factor of three each, for a finest grid spacing around DCPP of approximately 5 m. Currently, our code uses a fixed timestep, which generally is controlled by the finest grid size. In almost all cases, we used a timestep of 0.1 second.

A2.2 BREAKING AND NON-BREAKING WAVES

Full tsunami waveforms were calculated using two-dimensional (2-D) nonlinear Boussinesq equations to examine the effects of earthquake and submarine landslide tsunami sources at Diablo Canyon, along the central California coast. The results of these scenarios only include a first-order approximation of the incompressible breaking wave. The study of more realistic breaking waves dates back to the 1960s, but only within the last decade have full 3D compressible Naviar-Stokes calculations been implemented for examining mega-tsunamis due to the effects of near-Earth asteroid impacts and volcanic collapses (e.g., Mader, 2004). However, the most applicable results have used empirical relationships derived from experimental wave-tanks and provide the best evidence of a reduction of wave runup by breaking waves relative to non-breaking wave numerical calculations.

Generally, breaking waves in experimental wave-tanks generate smaller wave runup and therefore less inundation than predicted from numerical calculations based on non- or weakly-breaking wave equations. These are typically calculated using a first-order approximation of nonlinear 2-D incompressible waves including the Boussinesq or other 2-D forms of the Navier-Stokes equations. In experimental wave-tanks, the reduction in wave runup by breaking waves is one-half when the incident wave and water depth near the shoreline are approximately unity for a ~26° sloping beach. The wave runup is reduced by 1/2 to 1/5 for incident wave heights in the range of 1 to 10 meters typically observed in tsunamis. The reduction in runup by breaking waves is even greater for shallow sloping beaches.

These experiments confirm what is already known in the defense research community as the so-called "Van Dorn effect," (Van Dorn, 1961, 1965, 1968) summarized by Melosh (2003). One important aspect of the Van Dorn effect is that the wave amplitude is limited to approximately 0.4 times the water depth because of breaking wave effects and energy dissipation of high-frequency waves. This indicates that most wave energy from a mega-tsunami is lost during breaking along continental margins. Although the Van Dorn effect applies to asteroid impacts for dimensions < 1 km, it will also apply to volcanic collapses of similar dimensions.

Nonlinear Long Wave Versus Linear Methods

We use a numerical methodology based on so-called "weakly breaking waves" by modifying two assumptions made in the linear forms. The total derivative of the velocity field is

$$\frac{DV}{Dt} = \lim_{\Delta t \to 0} \frac{\Delta V}{\Delta t} = v_y \frac{\partial V}{\partial x} + v_x \frac{\partial V}{\partial y} + \frac{\partial V}{\partial t} = \frac{\partial V}{\partial t} + (v \cdot \nabla)V$$

where V is the instantaneous velocity field $V(x,y,t)$ and v_x and v_y are the components of the velocity field in the x and y directions. This is also known in fluid mechanics as the material, advective, or substantive derivative. Advection in a Eulerian approach is the effect of transport of fluid on an instantaneous velocity field. The advection terms resulting from the expression $(v \cdot \nabla)V$ makes the forms of the Navier-Stokes equations very nonlinear and difficult to solve. The linear theory neglects advection terms and assumes that the total derivative is $\frac{DV}{Dt} = \frac{\partial V}{\partial t}$. This assumption is only valid when the amplitude of the wave h is much smaller than the water depth d ($h << d$) and is therefore

most significant for breaking waves in shallow water. The advective terms take into account the effect of water transport or flow on the velocity field and have a particularly strong diffusion-type effect on shock waves or sharp disturbances in the fluid (e.g., the effect of wind on the propagation of an acoustic sound wave). The other modification to the nonlinear shallow water long wave equations is in the continuity equation, where the instantaneous phase velocity c in the linear code is $c = \sqrt{gd}$ but in the nonlinear equations includes wave height in the water depth $d' = (h + d)$. This allows the crest of waves to travel faster than the troughs and steepen. The equations are of incompressible forms and codes are set up using the Eulerian rather than Lagrangian approach, so the waves cannot topple over and fully break. A fully breaking wave would require a 3-D Navier-Stokes equation in Lagrangian form for a compressible fluid including correct handling of the water-air interface.

Summary of Experiments and Numerical Calculations

The breaking wave problem is complex, and most of the previous work on breaking wave run-up has consisted of experimental studies or numerical simulations. Typically, after a wave breaks, the propagating wave forms a bore. Ho and Meyer (1962) and Shen and Meyer (1963) originally proposed an analytical theory for bore runup using the nonlinear water equations. They found that the bore collapsed at the shoreline and transformed into a thin sheet of water propagating up a slope. Shen and Meyer (1963) theoretically predicted the maximum runup from bore as,

$$R_b = \frac{u_{xy}^{\ 2}}{2g}$$

which is independent of beach slope, where u_{xy} is the horizontal velocity of the bore at the shore and g is gravitational acceleration. Miller (1968) and Yeh (1991) further experimentally investigated bore runup and found that beach angle and bottom friction were important factors. Empirically, Yeh (1991) found that reducing the equation by u_{xy} produced better fits to the experimental observations.

Battjes (1974) used dimensional analysis to analyze the characteristics of periodic wave breaking and runup on plane slopes. They found that one parameter, the surf similarity parameter ζ ,

$$\zeta = \tan\beta \left(\frac{H}{L_0}\right)^{\frac{1}{2}}$$

approximately governed many wave-breaking characteristics. β is the angle of the beach slope, H is the incident wave height, and L_0 is the deep-water wave length of the incident periodic wave. Battjes (1974) presented experimental data and empirical formulas for several wave characteristics including $R/H = \zeta$ (in the range of $0.1 < \zeta < 2.3$), the runup R normalized by the incident wave height H. Kobayashi and Karjadi (1994) extended the surf similarity parameters proposed by Battjes (1974) for solitary wave runup. The wavelength of solitary wave L_0 was defined as,

$$L_0 = \frac{gT^2}{2\pi}$$

where T is the period of the solitary waves. Kobayashi and Karjadi (1994) fitted the breaking wave data of Synolakis (1986) and the numerical data from their own model and developed an empirical relation for maximum runup R normalized by incident wave height H by,

$$\frac{R}{H} = 2.955\zeta^{0.395}.$$

Synolakis (1986) and Zelt (1991) confirmed analytical breaking wave and numerical models for non-breaking waves by comparing their resulting runups from earlier studies. The following expressions were developed by Synolakis (1986) for non-breaking waves,

$$\frac{R}{h_0} = 2.831\sqrt{\cot\beta}\left(\frac{H}{h_0}\right)^{\frac{5}{4}}$$

where R is runup, h_0 is the water depth in the constant depth region, *beta* is the beach slope, and H is the incident wave height. For a breaking wave,

$$\frac{R}{h_0} = \frac{H}{h_0} + 0.918\left(\frac{H}{h_0}\right)^{0.606}.$$

Typically these relationships are shown as dimensionless parameters, normalized runup (R/h_0) versus normalized incident wave height (H/h_0).

Wave basin experiments by Briggs et al. (1995) found that the runup values were somewhat smaller than those obtained from narrower wave tanks used in previous studies. Experimental results typically conclude that the breaking height-to-depth ratio was about 1.2 for solitary wave heights on gentle slopes. The ratio increases for steep slopes and also for decreasing relative incident wave height. The breaking amplitude and breaking depth increases with decreasing slope.

Li (2000) studied the runup of breaking waves numerically and experimentally because no theoretical foundation yet exists. They found that the splash up caused by the breaking jet (the portion of the wave which curls over and topples) impinging on the beach strongly affects the runup process. If maximum runup is of most interest, then the approximation of a propagating bore may be sufficient. Li (2000) developed a numerical scheme that predicts results from wave tank experiments and numerical calculations for 1:2 and 1:20 beach slopes for only solitary waves (Figure A2-1). Experimental and numerical results agree very well for non-breaking waves and reasonably well for breaking solitary waves (compare circles and triangles on the left graph of Figure A2-1 and dark red with light green lines in both graphs of Figure A2-1). Breaking waves may have a more asymptotic behavior for extreme values. The right graph shows that for a shallow sloping beach, the difference in maximum runup between breaking and non-breaking waves is much larger. The breaking wave is about a factor of 1 to 10 lower than a non-breaking solitary wave, and the difference increases with increasing incident wave height.

Kobayashi and Karjadi (1996) developed an empirical relation for runup by a solitary wave as a function of incident wave height H and period (T) using the surf-similarity parameterization of Battjes (1974). This relationship suggests that the period of the incident wave, particularly going from wind swells (5<T<10 sec) to tsunamis (50<T<300 sec), plays a significant role in the eventual runup, which is not easily reproducible in wave-tank experiments. Physically, it is understandable that longer-period breaking waves will cause more runup than short-period waves.

Li and Raichlen (2003) updated the Li (2000) semi-empirical relation for a breaking solitary wave by proposing a solution to the breaking jet problem based on energy conservation. The empirical expression for energy dissipation during wave breaking is based on the bore representation of post-breaking wave conditions proposed by Li (2000). Li and Raichlen (2003) used the energy dissipation model and energy conservation considerations for the prediction of the maximum runup and compared them to experiments. During the process a portion of the energy is reflected from the slope and

a portion of the energy is dissipated. The energy from dissipation, E_D is caused by several mechanisms: friction at the free surface between the air and water, friction at the bottom of the wave tank, and wave breaking. This is expressed as: $E_D = E_{FF} + E_{FB} + E_B$, where E_D is the total dissipated energy, E_{FF} is the energy dissipated by friction at the air-water surface, E_{FB} is the dissipation at the ocean bottom, and E_B is the energy dissipation associated with wave breaking. E_{FF} is assumed small compared to the incident wave energy and is therefore neglected. The energy dissipation is considered solely due to wave breaking ($E_D \approx E_B$). The energy balance for the runup process at an arbitrary location on the slope shoreward of breaking can be expressed as $E_I = E_K + E_P + E_B + E_R$, where E_K and E_P are the kinetic and potential energies, present in the domain during the runup process, and E_I is the total incident energy. Data were collected from tank experiments and empirical equation were fit to these data by,

$$\frac{E_B}{E_I} = C[A\ln(\cot\beta) + B]$$

where,

$$A = -0.470(H/h0) + 0.534$$

$$B = 2.165(H/h0) - 1.154$$

$$C = 0.190(\ln(H/h0)) + 0.969$$

The maximum predicted runup R in metric system based on energy considerations is a function of slope β, and E_B/E_I,

$$\frac{R}{h_0} = \left[1 - \frac{E_B}{E_I}\right]\frac{H}{1.5\alpha h_0}$$

where H is the incident wave height at water depth h_0, and α is the wave shape factor found empirically as 0.18, which gave the best fits to the above equation. This equation is shown in Figure A2-2 for a 2 degree slope for both h_0=20 and 100 m and is similar to the breaking solitary wave equation shown in Figure A3-1. The new relations suggest that the wave heights are reduced by a factor of 1/5 in the breaking case for a wide range of h_0, H, and beach slope.

Comparison of URS Runup Results with Li and Li & Raichlen Results

In Figure A2-2, we compare the runup estimates of Li (2000) and Li and Raichlen (2003) with runup calculations using the URS weakly breaking wave formulation. The URS

runup estimates are lower than those for the non-breaking waves, and are in closer agreement with the breaking wave model predictions of Li and Raichlen (2003). Our expectation is that a weakly breaking wave runup should be lower than those for non-breaking waves but likely higher than those for breaking waves. Our runup estimates, shown as the red line in Figure A2-2, are about 0.6-0.7 times lower than the newer breaking wave relation of Li and Raichlen (2003); however, the wave tank and numerical solutions of Li and Raichlen (2003) are for a one-way solitary plane wave equation. Therefore, to be compared with the estimates of Li and Raichlen (2003), our wave amplitudes should be multiplied by at least a factor of two because our wave propagates as spherically in two dimensions in the numerical calculations; this modification is shown as the blue line in Figure A2-2. The sum of the two wave fronts propagating away from the initial source area is typically equal to a one-way solitary wave. This places our results in between the breaking and non-breaking relationships, as expected. This example illustrates the problem of comparing directly the results from previous breaking and non-breaking wave studies to our numerical calculations.

Implications for Diablo Canyon

Based on the above analyses, we estimate that the URS calculations for weakly breaking wave conditions provide a reasonable runup estimate. The average bathymetry slope just offshore of Diablo Canyon is about 1-2° out to 10-km distance. Therefore the relationships for 1:20 slopes shown on the right-hand side of Figure A2-1 and in Figure A2-2 are more applicable to this study. The wave runup amplification for breaking waves along shallow-sloping beaches is shown in Figure A2-1 to be about 2 to 3 times higher than the incident wave height. For example, for a normalized incident wave height (H/h_0) of 0.1 (in a water depth of h_0=10 m), the incident wave height (H) will be 1 m. The predicted runup amplification ratio (R/H) will be 7 for a purely non-breaking wave and 3 for breaking waves. For another example, given a normalized wave height of 1 (in a water depth of h_0=10 m), the resulting wave runup amplification ratio (R/H) for breaking waves is 2 and about 10 for non-breaking waves. This is not easily seen in Figure A2-1 because it mainly shows the differences between (R/H) for both wave types. The breaking wave curve (R/h_0) is 2.3 times lower than the breaking wave curve at (H/h_0) of 0.1 and becomes even lower with increasing (H/h_0). The curve is 5 times lower at H/h_0 of 1 and reaches 10 times lower for H/h_0 approaching 10. This is probably applicable to all waves including those from mega-tsunamis. According to the Van Dorn effect (e.g., Van Dorn, 1968), mega-tsunamis generated from asteroid or volcanic collapses will break along the wide continental margins along the central California coast and lose most of their energy before reaching the shore.

A2.3 COSEISMIC SURFACE DISPLACEMENTS

We take the traditional "decoupled" approach by first calculating the elastic deformation on the ocean bottom generated by the earthquake, and then use this as an initial condition on the "rigid" ocean bottom. Therefore, the decoupled approach includes no influence of the tsunami in the fluid body on the elastic earth. With the small compressibility of water, it has been shown by others (e.g., Comer (1984), Kajiura (1970)) that both coupled and decoupled approaches give similar solutions and the coupling effect is negligibly small. The ocean or lake bottom deformation due to faulting can be calculated using the elastic theory of dislocation. The displacement in an elastic medium is given by the Representation theorem, and is related to the space and time integration of slip distributed across the fault plane Σ where,

$$U_n(\vec{x},t) = \int \partial\tau \iint [\mu \vec{n}_j u_j(\vec{\xi},\tau) G_{ni,j}(\vec{x},\vec{\xi}\ t-\tau)]\partial\Sigma$$

is the n[th] component of displacement. The term $\mu \vec{n}_i u_j(\vec{\xi},\tau)$ is a product of the rigidity, fault orientation vector, and fault slip at point $\vec{\xi}$ and time τ. $G_{ni,j}(\vec{x},\vec{\xi}\ t-\tau)$ are the Green's functions (GFs) that describe the wave propagation from each point on the fault to the receiver. x is the vector describing the relative location of the source and receiver. The slip function $u_j(\vec{\xi},\tau)$ is predetermined using various scenarios.

The GFs can be computed using two methods, analytical or reflectivity frequency-wavenumber summation method. The analytical method (e.g., Okada (1992)) is fast because it only considers elastic halfspace using equations derived for rectangular faults and point sources. The use of the reflectivity f-k method (e.g., Zeng and Anderson (1995)) is more time-consuming. It uses layer matrices with reflectivity coefficients to compute f-k spectra and then integration method to compute the time-history or static ground displacement at the surface or buried receiver location. This is only a point source method; therefore, there is the problem of spatial aliasing of the continuous displacement field.

A2.4 LANDSLIDE MODEL

Landslide-generated tsunami wave heights are dependent on size (length, width), thickness, slide velocity, and water depth. The dynamical behavior of submarine landslides is not well known, since very few direct observations of submarine landslides exist. We have used simplified sliding models that are broadly consistent with observed

landslide geometries, and whose dynamical models are governed by simple equations derived from first-principles.

Kinematic Model

We used a simple kinematic model to simulate the effect of submarine landslides (Figure A2-3). The model consists of a single block with a trapezoidal profile. The main dimensions are the downslope width (W), the along-strike length (L), and height at the top (H_{top}) and bottom (H_{bottom}). The block is tapered on all four sides. The sliding of the block occurs in two stages, the first on a purely rigid translation at high velocity (usually 10-50 m/sec) and a second runout phase where the tail end of the block stops and the head decelerates linearly and therefore effectively stretches. For the landslide scenarios, this shape is actually extracted from the seafloor and the changes in seafloor bathymetry are taken into account at every timestep. The dimensions and orientation of the landslide that we modeled were given by Geomatrix (2005), and where a range of dimensions was given we chose the largest ones. In general, the amplitude of a tsunami scales roughly linearly with the vertical offset of the seafloor, be it caused by an earthquake or landslide. It is therefore straightforward to estimate the effect of a range of offset values from a single scenario by linear extrapolation.

Landslide Velocity

It is clear that the high velocities yield much larger amplitudes, and more severe inundation. This is further illustrated by a graph showing the dependence of tsunami amplitude on slide velocity at the shoreline at Diablo Canyon (Figure A2-4) and just offshore. There are no direct observations of slide velocities of submarine landslides, and all modeling efforts so far have to rely on theoretical estimates or on the interpretation of tsunami data. Model-based velocities found in the literature span a very wide range, with 50 m/sec for a model of a landslide off Palos Verdes (Locat et al., 2004) to 150 m/sec for landslides off Tenerife (Hurlimann et al, 2000), and values from 10-150 m/sec for several worldwide landslides (Ward and Day, 2001). Velocities based on observed runup heights include 60-80 m/sec for the 1741 Oshima tsunami and 50-100 m/sec for the Nuuanu slide (Satake, 2001). Finally, Ten Brink and Geist (2005) used a value of 40 m/sec to model landslides around Puerto Rico.

We used a simple 1-D sliding block model that contains a basal friction term for calculating the submarine landslide velocities similar to the methodology of Ward and Day (2003). For submarine slides the friction can be considered as a coefficient of effective friction that includes basal friction including other loss mechanisms. Given the

slope profile h(x), we compute the peak v_p and average $\bar{v}$ slide velocities controlled by gravitational sliding down an inclined surface including frictional forces,

$$v(x) \approx \sqrt{2g}\left[h_0 - h(x) - \mu x\right]^{\frac{1}{2}}$$

where v(x) is the slide velocity as a function of distance x, g is gravitational acceleration constant 9.8m/s^2, h(x) is the slope profile, h_0 is the drop height, and μ is the coefficient of "effective" friction. Runout distance is approximately $xc=h_0/\mu$. The location of the breakaway points were modified slightly to find optimal slope profiles for sliding. We lowered the friction until sliding occurred. In some cases the slide velocity was zero for all positive frictional values, and therefore, we implemented an artificial minimum slide velocity of 1 m/s.

A2.5 COMPARISON TO THE MOST CODE

In order to validate our numerical codes, we performed a comparative study with the Method of Splitting Tsunamis (MOST) code (Titov and Gonzalez, 1997), which is in wide use today by tsunami researchers at NOAA and other institutes. For comparison we used the 1960 Chile earthquake (uniform rupture) with observations near Diablo Canyon. This experiment addresses both long-term stability issues (because of the very long path) as well as issues of local grid refinements and non-linear effects, since both use a nested grid approach to include detailed bathymetry around the site of interest. The result is shown in Figure A2-5, where we have plotted the time-series from both methods using identical source models and almost identical (due to different parameterizations) bathymetric models. It is clear that the two methods give very similar results, in particular at the beginning of the record, with some deviation further back in the record at higher frequencies.

A2.6 INSTRUMENTAL MEASUREMENTS OF TSUNAMIS

Instruments of various types have been used to measure tidal changes. Typically the tide changes over a 12-hour period, so most recording systems have mechanisms to desample the continuous observations or filters to reduce shorter period noise, such as wind swells. Tsunamis have periods of about 5 to 30 minutes, so both high sampling at shorter period and an appropriately damped response are very important for tsunami and seiche observations.

The U.S. National Ocean Service (NOS) has operated tide gauges along the Pacific coasts, including islands and lakes, since 1850. Tidal instruments are sometimes installed in harbors, ports and at the end of long piers in deep water (> 10 meters) to minimize the amplification effects of wave shoaling and complexities of wave breaking. The first generation NOS system is the stilling-well gauge. Satake et al. (1988) and Satake and Kanamori (1991) have extensively examined the response of stilling-well instruments, the most traditional and popular mechanical system used in the Pacific, including Japan and U.S. A wire to a recorder transmits vertical motion of a float in the well. The nominal gain is 330 cm/ft, the motions are recorded on an analog strip chart, and the response is flat for very long periods (tides). The water enters an opening that acts as a low-pass filter, reducing shorter period noise. Satake et al. (1988) found that the response of these types of systems is very poor if the tsunami period is shorter than the response time of the instrument. The new generation NOS systems in use today use acoustic waves to measure the water level in a tube and sample every second with a 1 cm accuracy; averaging the samples into 3- and 6-min intervals reduces the data volume and time resolution.

Satake and Kanamori (1991) showed that tide gauge instruments underestimate tsunami amplitudes only for small earthquakes and tsunamis, and that the tide gauge may slightly overestimate tsunami amplitudes for large earthquakes and tsunamis. Whether there is amplification or deamplification depends on the period of the incoming wave, which is proportional to the size of the earthquake. The tsunami waveforms from the 1968 Tokachi-oki and 1983 Japan Sea tsunamis were corrected for instrument response and shown to require a 33% upward correction for a 10 min period wave, but for a 30-min period no correction was needed. For reference, the tsunami that struck Banda Ache, Sumatra, in the 2004 Indian Ocean tsunami had a period of 30 min, and in Thailand and Sri Lanka the period was about 5 to 15 min. The periods of waves that were recorded at Avila Beach or Port San Luis by distant historical tsunamis were in the 5 to 15 min range, and therefore may be underestimated by about 0-33%. We account for the instrument by low-passing the simulated records to better fit the amplitude response of the instruments. The damped response and undersampling effects were not corrected and may explain some of the misfit in phase to the simulations. Finally, large damaging waves will be recorded without distortion up until the system is destroyed or damaged and becomes inoperable.

A2.7 REFERENCES

Battjes, J.A., 1974, Surf similarity: Proceedings of the 14th Conference on Coastal Engineering, ASCE, v. 1, p. 466-480.

Briggs, M.J., Synolakis, C.E., and Hughes, S.T., 1995. Large scale 3-dimensional laboratory measurements of tsunami inundation, in Tsunami Progress in Prediction, Disaster Prevention and Warning: Kluwer Academic Publishers, p. 129-149.

Comer, R.P., 1984, The tsunami mode of a flat earth and its excitation by earthquake sources: Geophysical Journal of the Royal Astronomical Society, v. 77, p. 1-27.

Geomatrix Consultants, Inc., 2005, Evaluation of Potential Tsunami Sources in the Diablo Canyon Power Plant Region, Final Report – Local Sources of Tsunamis in the DCPP Region, Report to Pacific Gas and Electric Company, December.

Ho, D.V., and Meyer, R.E., 1962, Climb of a bore on a beach: Journal of Fluid Mechanics, v. 14, p. 305-318.

Hurlimann, M., Garcia-Piera, J.O. and Ledesma, A., 2000, Cases and mobility of large volcanic landslides: Application to Tenerife, Canary Islands: Journal of Volcanic and Geothermal Research, v. 103, p. 121-134.

Kajiura, K., 1970, Tsunami source, energy, and the directivity of wave radiation: Bulletin of the Earthquake Research Institute, University of Tokyo, v. 48, p. 835-869.

Kobayashi, N., and Karjadi, E.A., 1994, Surf-similarity for breaking solitary wave runup: Journal of Waterway, Port, Coastal, and Ocean Engineering, v. 120, p. 645-650.

Kobayashi, N. and Karjadi, E.A. (1996), "Obliquely Incident Irregular Waves in Surf and Swash Zones," Journal of Geophysical Research, 101(C3), 6527-6542.

Li, Y., 2000, Tsunamis: Non-breaking and Breaking Solitary Wave Run-up: Ph.D. Thesis, Mechanical Engineering, Report # KH-R-60, Caltech.

Li, Y., and Raichlen, F., 2003, Energy balance for breaking solitary wave runup: Journal of Waterway, Port, Coastal and Ocean Engineering, v. 129, no. 2, DOI: 10.1061/(ASCE)077-950X(2003) v. 129:2, no. 47, p. 47-59.

Locat, J., Lee, H.J., Locat, P. and Imran, J., 2004, Numerical analysis of the mobility of the palos Verdes debris avalanche, California, and its implication for the generation of tsunamis: Marine Geology, v. 203, p. 269-280.

Mader, C.L., 2004, Numerical Modeling of Water Waves: 2nd Edition, CRC Press, Boca Raton, Florida.

Melosh, H.J., 2003, Impact-generated tsunamis: An over-rated hazard (Abs.): Lunar and Planetary Science XXXIV.

Miller, R., 1968, Experimental determination of run-up of undular and fully developed bores: Journal of Computational Physics, v. 115, p. 200-212.

Okada, Y., 1992, Internal deformation due to a shear and tensile faults in a half-space: Bulletin of the Seismological Society of America, v. 82, p. 1018-1040.

Press, W.H., Teukolsky, S.A., Vetterling, W.T., and Flannery, B.P., 1992, Numerical Recipes in FORTRAN: The Art of Scientific Computing: Cambridge University Press.

Satake, K., 1995, Linear and nonlinear computations of the 1992 Nicaragua earthquake tsunami: PAGEOH, v. 144, p. 455-470.

Satake, K., Okada, M., and Abe, K., 1988, Tide gauge response to tsunamis: Measurements at 40 tide gauge stations in Japan: Journal of Marine Research, v. 46, p. 557-571.

Satake, K., and Kanamori, H., 1991, Use of tsunami waveforms for earthquake source study: Natural Hazards, v. 4, p. 193-208.

Satake, K., 2001, Volume Estimate and Tsunami Modeling of Underwater Landslide from Submarine Survey Data: American Geophysical Union, Fall Meeting, 2001.

Shen, M.C., and Meyer, R.E., 1963, Climb of a bore on a beach, part-3: run-up: Journal of Fluid Mechanics, v. 16, p. 113-125.

Synolakis, C.E., 1986, The run-up of long waves: Ph.D. Thesis, Caltech.

Ten Brink, U., and Geist, E., 2005, Size distribution of submarine landslides and implications for tsunami probability in Puerto Rico: EOS, American Geophysical Union, Fall Meeting, 2005.

Titov, V.V., and Gonzalez, F.I., 1997, Implementation and testing of the Method of Splitting Tsunami (MOST) model: NOAA Technical Memorandum ERL PMEL-112, 11 p.

Van Dorn, W.G., 1961, Some characteristics of surface waves in the sea produced by nuclear explosions: Journal of Geophysical Research, v. 66, no. 11, p. 3845-3862.

Van Dorn, W.G., 1965, Tsunamis Advances in Hydroscience, vol. 2: Academic Press, New York.

Van Dorn, W.G., 1968, Tsunamis, in Contemporary Physics. A Review of Physics and Associated Technologies: Taylor & Francis, Ltd., London, v. 9 no. 2. p. 145-164.

Ward, S., and Day, S., 2001, Cumbre Vieja Volcano – Potential collapse and tsunami at La Palma, Canary Islands: Geophysical Research Letters, v. 28, p. 3397-3400.

Ward, S.N., and Day, S., 2003, Ritter Island volcano – lateral collapse and the tsunami of 1888: Geophysical Research International, v. 154, p. 891-902.

Yeh, H.H., 1991, Tsunami bore runup: Natural Hazards, v. 4, p. 209-220.

Zelt, J.A., 1991, Overland flow from solitary waves: Journal of Waterway, Port, Coastal, and Ocean Engineering: ASCE, v. 117, p. 247-263.

Zeng, Y., and J.G. Anderson, 1995, A method for direct computation of the differential seismogram with respect to the velocity change in a layered elastic solid: Bulletin of the Seismological Society of America, p. 85,300-307.

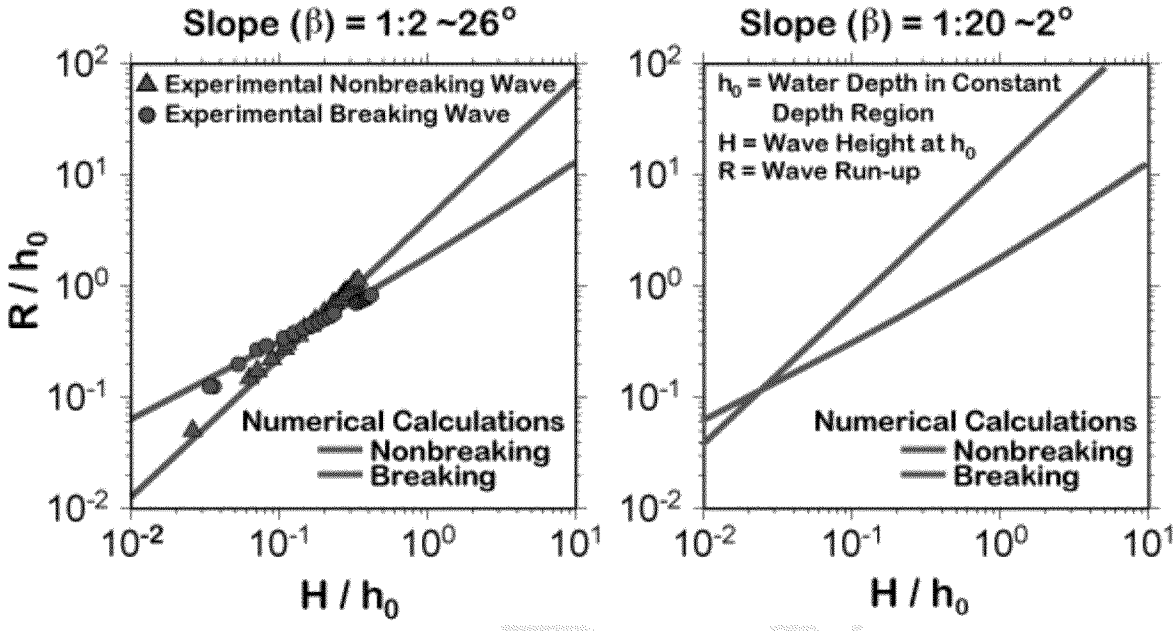

Note: Comparisons by Synolakis (1986), Zelt (1991), and Li (2000) between breaking and non-breaking solitary waves from wave tank experiments and numerical calculations for two beach slopes, gentle (1:20) and steep (1:2) slopes (rise/run). Experimental and numerical results agree very well for non-breaking waves and reasonably for breaking solitary waves (see circles and triangle on the left graph). Breaking waves may have a more asymptotic behavior for extreme values. The right graph shows that for a shallow sloping beach, the difference in maximum run-up between breaking and non-breaking waves is much larger. The breaking wave is about a factor of 1 to 10 lower than for a non-breaking solitary wave and the difference increases with increasing incident wave height.

Figure A2-1 Comparison between breaking and non-breaking waves from wave tank experiments and numerical calculations

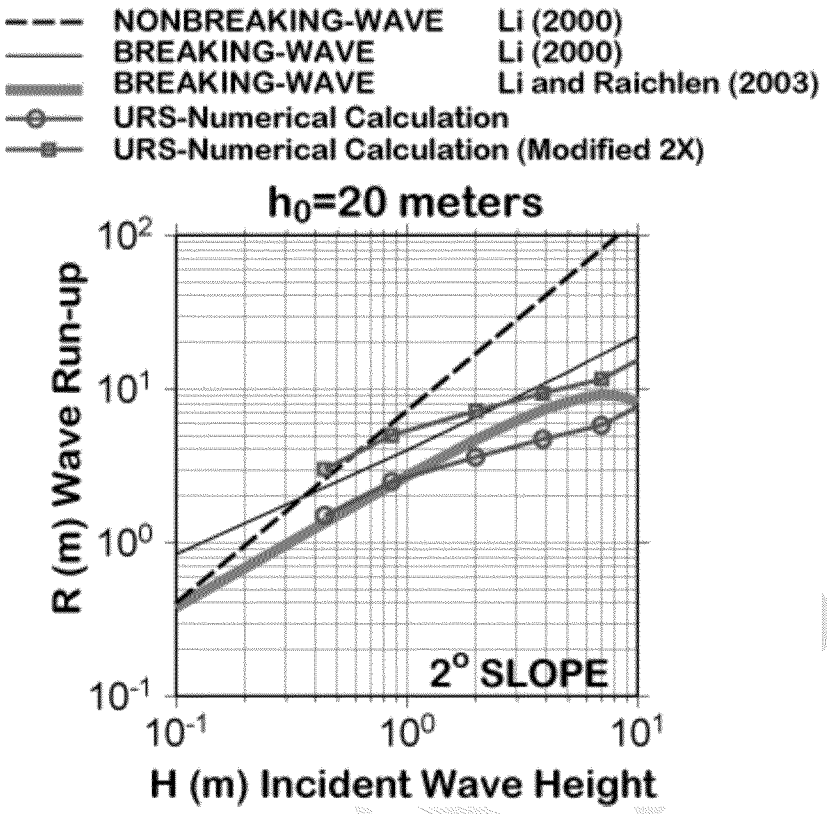

Note: A numerical nonlinear wave simulation based on a weakly breaking wave for a circularly propagating wave is used in this study rather than the one-way solitary wave conditions of a wave tank environment. This is compared to the new relations of Li and Raichlen (2003) and the older relation of Li (2000), which are based on empirical data from wave tank experiments including energy considerations in the latter relation. To be properly compared with the Li and Raichlen (2003) estimates, the URS results (red-line) were multiplied by a factor of 2 to give appropriate results shown by the blue-line.

Figure A2-2 Predicted wave runup R as a function of incident wave height at water depth h_0 of 20 m for a 2-degree sloping beach

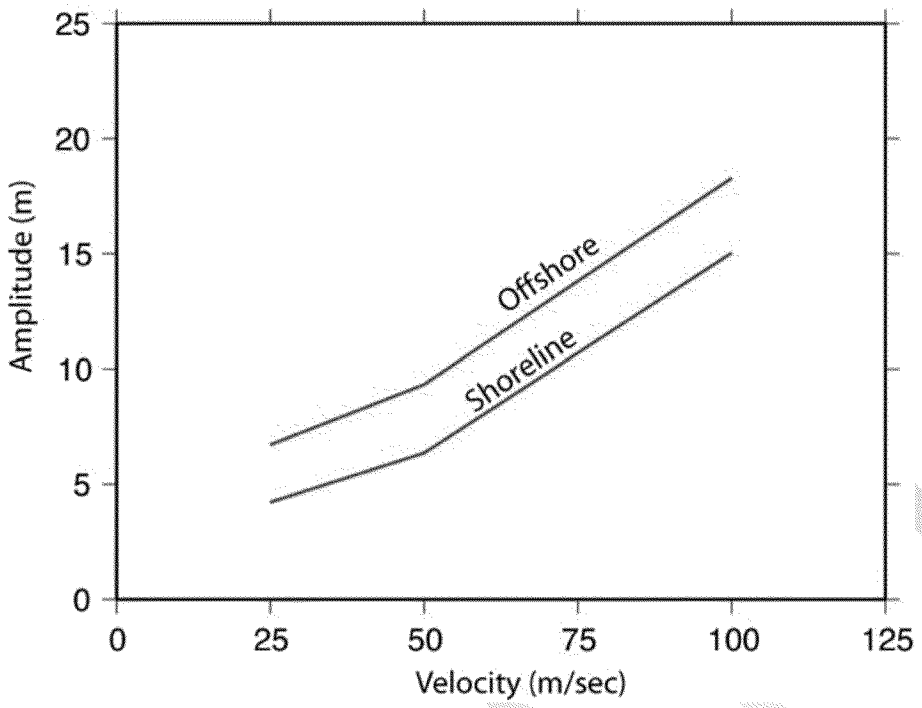

Figure A2-3 Runup height as a function of slide velocity for a submarine landslide

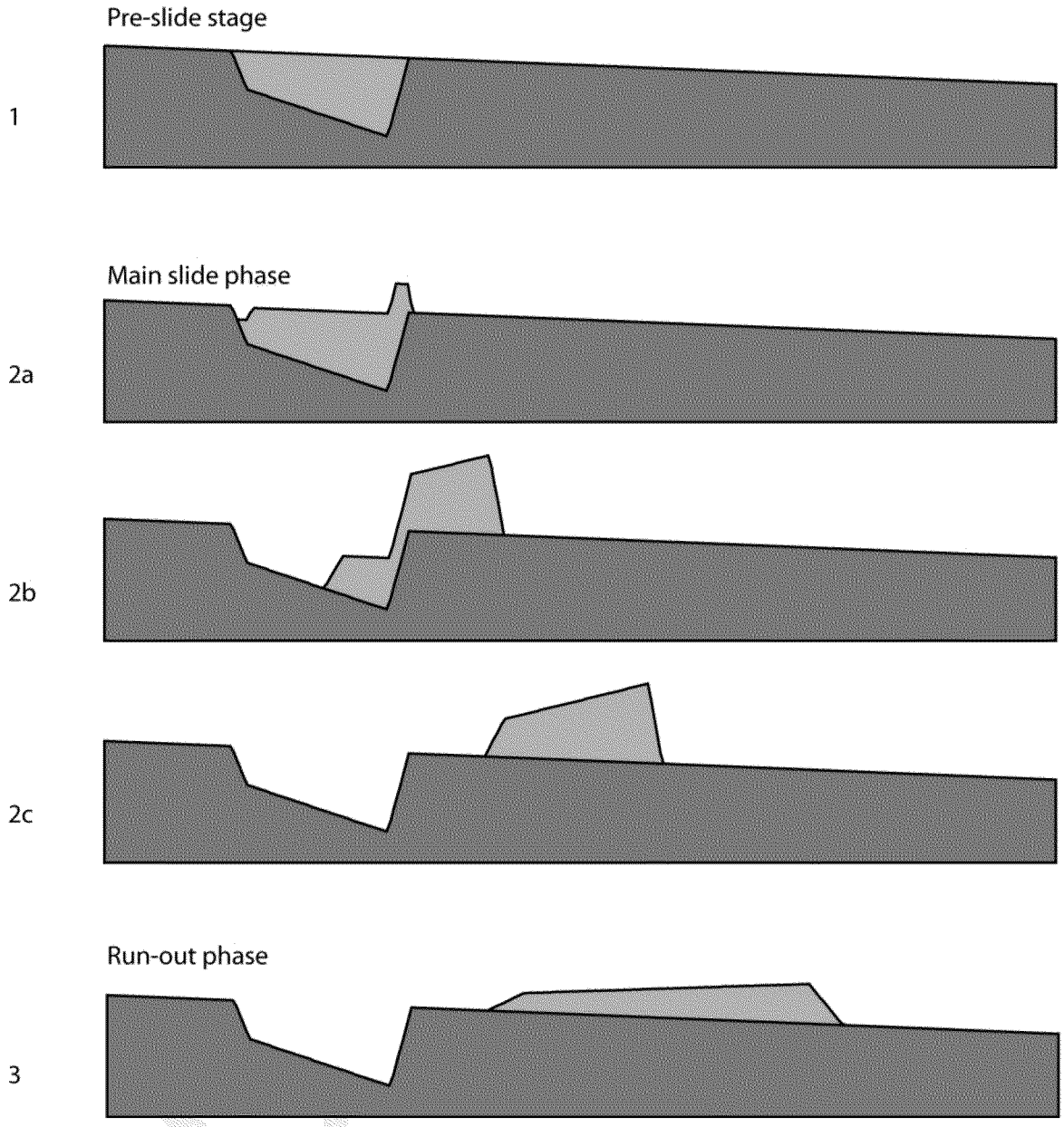

Figure A2-4 Cartoon showing the kinematic landslide model that was used in this study

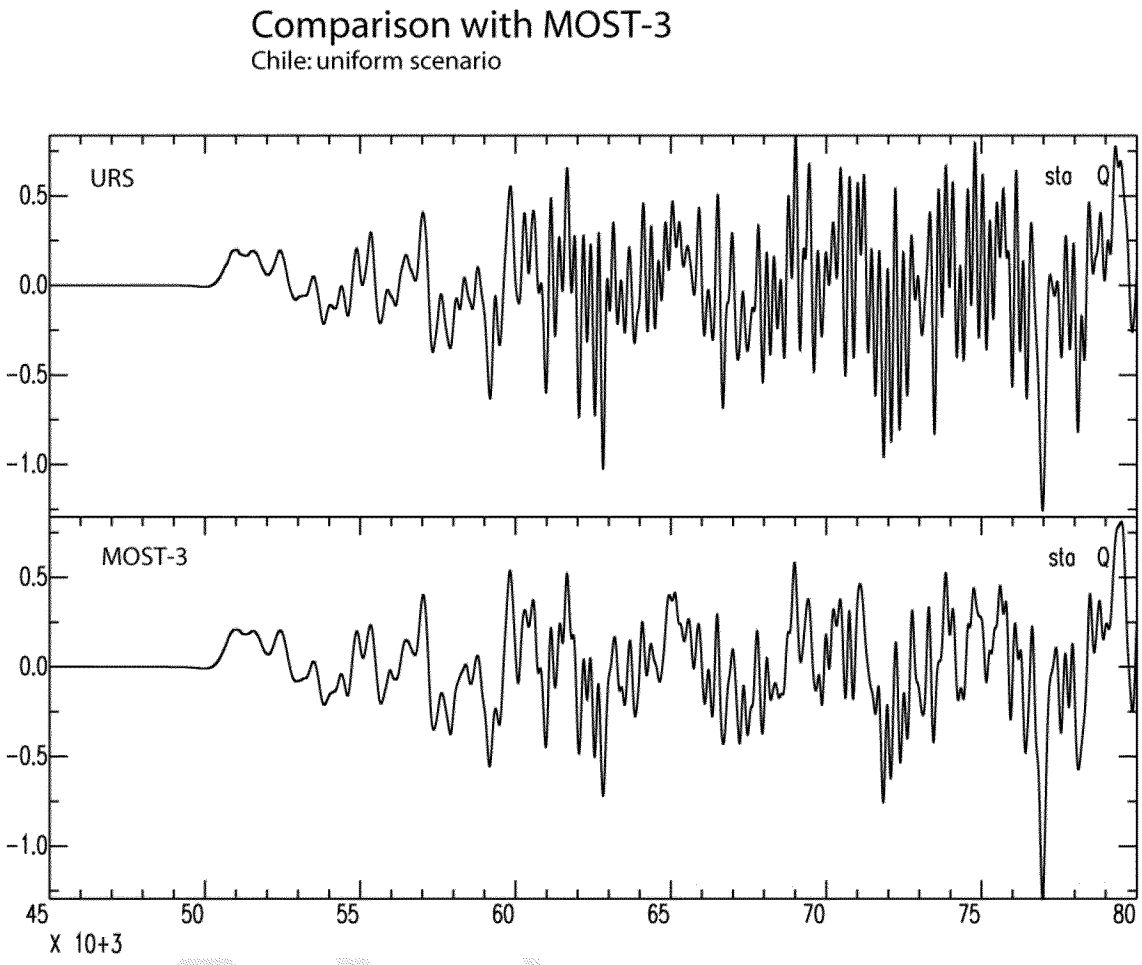

Figure A2-5 Comparison of simulated tsunami waveforms for the 1960 Chile earthquake using the URS (top) and MOST (bottom) codes.

APPENDIX 3
DISCUSSION OF APPLICABILITY TO CURRENT DCPP DESIGN AND LICENSING BASES

Appendix 3 - Discussion of Applicability to Current DCPP Design and Licensing Bases

Executive Summary

In April 2010, the Pacific Gas & Electric Geosciences department submitted a study titled, Methodology for Probabilistic Tsunami Hazard Analysis: Trial Application for the Diablo Canyon Power Plant Site (PTHA) to the Pacific Earthquake Engineering Research Center (PEER). The PTHA employs new, probabilistic methods aimed at developing a consistent approach for addressing different natural hazards under a risk-informed framework.

In September 2010, PEER will conduct a workshop on tsunami hazard analysis. This workshop is the first in a series that are intended to provide the scientific bases for developing a new tsunami hazard analysis standard for nuclear power plants.

This paper summarizes and compares the results of the PTHA to the results of the current Diablo Canyon Power Plant design and licensing basis tsunami hazard analyses which consist of both probabilistic risk assessment (PRA) and deterministic methods.

Comparison of the PTHA and the current PRA show that the probabilities of exceeding the critical flood levels are similar. The results of the PTHA shows that the assumed flooding levels in the current deterministic tsunami hazard analysis are not credible based upon low frequency of occurrence.

Background

Diablo Canyon Power Plant (DCPP) design and licensing bases contain evaluations of the impact of near-shore and distant tsunamis on safety relate structures, systems and components. These analyses are described in the DCPP Updated Final Safety Analysis Report (UFSAR), Section 2.4 and in PG&E Letter DCL-94-133, Response to NRC Generic Letter 88-20, Supplement 4, Individual Plant Examination of External Events for Severe Accident Vulnerabilities (IPEEE).

The UFSAR analyses use historical data and deterministic analytical approaches to determine the "Maximum Probable Tsunami Flooding" elevations. These analyses also determine the lowest level of tsunami drawdown. The results of the maximum runup and drawdown are compared to the structural capacity and physical characteristics of the intake structure and the auxiliary saltwater pumps (ASP) it houses.

The IPEEE analysis used probabilistic methods to determine the relative risk associated with beyond-design basis scenarios. In the case of intake flooding, the IPEEE considers the partial or complete loss of ASPs due to failure of the ASP compartment watertight doors and / or due to the doors being left open. The IPEEE analysis also considers the

risk associated with total loss of the ASP flow due to tsunami wave heights that exceed the elevation of the ASP compartment snorkels.

These two current design and licensing basis analyses are compared to the proposed PTHA described below.

Probabilistic Tsunami Hazard Analysis (PTHA)

Traditional tsunami hazard analyses for nuclear power plants have been based on deterministic methods. This approach arithmetically combines the maximum tsunami wave, storm surge and tide heights with a maximum storm wave height to determine a combined wave height. The individual contributors to the combined wave height are determined either from historical records, analytical methods or expert judgment.

The PTHA is a trial study being submitted for various agencies' consideration. The goal of this analysis is to improve the accuracy of tsunami hazard analysis by:

- Incorporating additional near and distant tsunami-generating faults
- Considering the impact of underwater landslide generated tsunamis
- Including the aleatory (randomness) affects on tsunami wave height
- Employing a probabilistic method (instead of arithmetic) to combine the tsunami waves, storms waves, and tides.

The PTHA considers Diablo Canyon-specific tsunami sources, tide and storm data, and topographic and bathymetric data. This PTHA does not consider the affect that the intake structure has on wave runup elevation. The tsunami hazard uses numerical simulation methods to compute the tsunami wave heights for a given earthquake or landslide scenario.

At this time, the PTHA is considered a methodology study and is not intended to be used in design decisions or margin evaluations. As such, the PTHA has been performed outside of the DCPP 10CFR50 Appendix B Quality Assurance Program. However, as an overall accuracy check, the simulation method has been validated by modeling historical tsunamis from earthquakes and comparing the wave heights predicted by the simulations with the wave heights recorded at tide gauge stations.

The result of the PTHA is a presentation of probabilistically combined wave heights at annual rates of being exceeded, shown in Figure 1, below.

Probable Maximum Tsunami Flooding (UFSAR)

The limiting case for the UFSAR tsunami runup was developed using historical tide, storm surge and storm wave data combined with an analytically determined, near shore tsunami wave height. Because the intake structure's geometry impacts the combined wave runup in a complex way, the maximum credible wave runup was determined using a scale model of the intake bay, breakwater and intake structure. This model was placed in a large tank with a wave generator to determine wave runup elevation on the scale model. The maximum runup value was obtained by simulating a combined, long period

wave consisting of tsunami, storm surge and tide of 17' MLLW with a superimposed storm wave height of 26.8' MLLW. This equates to a combined wave height of 43.8' MLLW. The resulting maximum runup was 34.6' MLLW. The limiting elevation (bottom of ASP snorkel) is 48' MLLW.

Tsunami drawdown was determined analytically in the UFSAR analyses. The bounding case resulted in -9.0' MLLW. The limiting elevation (based on ASP required suction head) is -17.4' MLLW (Reference 4).

Individual Plant Examination of External Events (IPEEE)

This goal of this analysis was to determine the core damage frequency (CDF) associated with flooding at the intake structure due to the simultaneous occurrence of a tsunami, high tide, storm waves and a degraded breakwater. The annual frequency of exceeding certain flooding levels was combined with the conditional core damage probability (CCDP) of loss of some or all of the ASPs.

This analysis established two critical flood elevations as follows:

> 20' MLLW is the elevation at which seawater may flood the top deck of the intake structure, allowing seawater to reach the ASP compartments. The frequency of exceeding 20' MLLW is combined with the likelihood that the ASP compartment doors are open or fail to remain watertight and the likelihood of core damage with the loss of 1, 2, 3 or 4 ASPs.
>
> 48' MLLW is the elevation at which seawater may flood the ASP compartment snorkels, resulting in a loss of all 4 ASPs. The frequency of exceeding 48' MLLW is combined with the likelihood of core damage when losing all 4 ASPs.

To determine the annual frequency of exceeding these critical flood elevations, the IPEEE conservatively assumed that the maximum tide, storm surge, and storm waves occur simultaneously. These contributions to wave height were combined arithmetically and compared to the critical flood elevations. The difference between the critical flood elevation and this arithmetic combination was taken as the tsunami wave height required to exceed the critical flood elevation.

Using tsunami frequency and magnitude data (Reference 5), the frequency of exceeding the critical flooding elevations was determined to be:

> Annual Frequency of Exceeding 20' MLLW = 8.4 E-4 per year
> Annual Frequency of Exceeding 48' MLLW = 5.0 E-7 per year

This analysis did not consider the effect the intake structure has on the runup water level, nor did the analysis consider tsunami drawdown.

Conclusions and Limitations

<u>Runup</u>

The UFSAR maximum credible wave height of 34.6' MLLW was developed by a simulated **43.8' MLLW** wave height, based on scale model testing. The PTHA predicts combined wave heights higher than 43.8' MLLW; however, the PTHA predicts the annual rate of exceeding this combined wave height is 8.0 E-7, as shown in Figure A3-1 below. Based upon this, higher waves (less frequent) are not considered credible.

The IPEEE analysis determined the frequency of exceeding two critical flood elevations: **20' and 48' MLLW**. The IPEEE annual frequency of exceeding the 20' MLLW flood elevation bounds (is greater than) the annual frequency predicted by the PTHA. The IPEEE annual frequency of exceeding the 48' MLLW flood elevation is similar to and within the accuracy of the annual frequency predicted by the PTHA as shown in Figure A3-1 and Table A3-1, below.

Drawdown

The PTHA report provides hazard curves for the drawdown due to tsunami and tides (not storms). The numerical simulations were not checked against historical tsunamis for drawdown. In particular, the aleatory variability of the drawdown has not been estimated. Therefore, the PTHA used upper and lower bounding values for the aleatory variability. Further, the site location used to represent the intake structure in the simulation has a mean water depth of 10.5' MLLW. As such, the PTHA does not make predictions below a drawdown level of -10.5' MLLW. Consequently, the PTHA is not suitable for direct comparison to the current DCPP design and licensing bases for drawdown.

Wave Velocity

The PTHA report also provides hazard curves for the wave velocities. Because the PTHA does not model the intake structure geometry, dynamic loading on the intake structure can not be predicted using the PTHA wave velocity. Consequently, the PTHA is not suitable for direct comparison to the current DCPP design and licensing bases for intake structure dynamic loading.

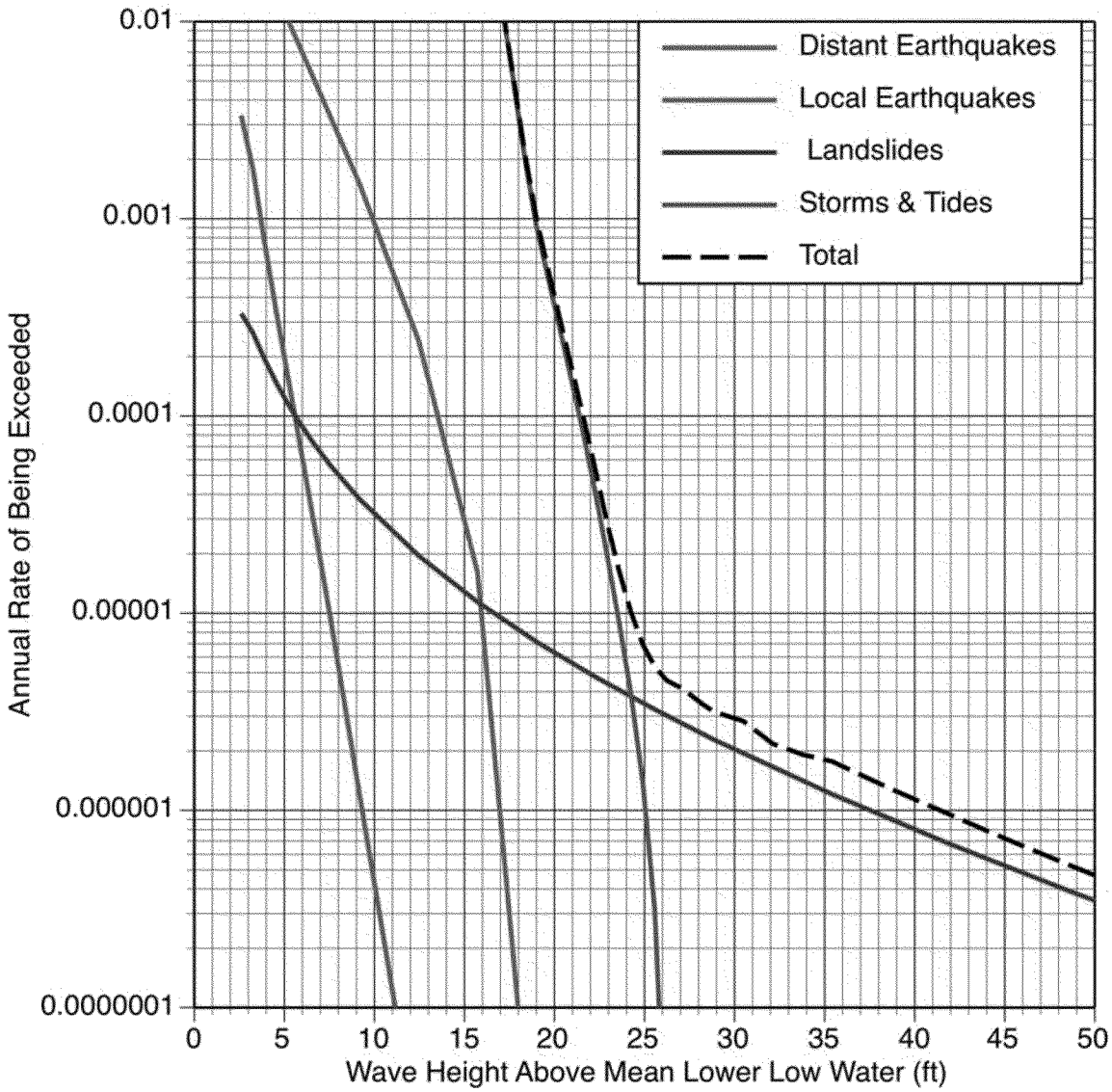

Figure A3-1. Mean hazard from storms, tides and tsunamis for the DCPP intake structure.

	Annual Probability of Exceeding 20' MLLW	Annual Probability of Exceeding 48' MLLW
IPEEE	8.4 E-4	5.0 E-7
PTHA	3.5 E-4	5.5 E-7

Table A3-1. Comparison of IPEEE and PTHA Annual Probabilities of Exceeding Critical Flooding Elevations

References

1. Cluff, L. S. et al, Methodology for Probabilistic Tsunami Hazard Analysis: Trial Application for the Diablo Canyon Power Plant Site, Submitted to PEER Workshop for Tsunami Hazard Analysis for Engineering Design Parameters, Berkeley CA, September 2010.
2. Diablo Canyon Power Plant Updated Final Safety Analysis Report, Revision 19, Section 2.4
3. PG&E Letter DCL-94-133, Response to NRC Generic Letter 88-20, Supplement 4, Individual Plant Examination of External Events for Severe Accident Vulnerabilities
4. Design Criteria Memoranda S-17B, Auxiliary Saltwater System, Revision 18C
5. Houston, J. R., and A. W. Garcia, "Type 16 Flood Insurance Study: Tsunami Predictions for the West Coast of the Continental United States," Hydraulics Laboratory, U.S. Army Engineer Waterways Experiment Station, December 1978.